UNIVERSITÄT DUISBURG ESSEN

PHYSIK

Time-dependent electronic transport and relaxation in nanoscale conductors

Der Fakultät für Physik
der Universität Duisburg-Essen
vorgelegte

Dissertation

zum Erwerb des Grades
„Doktor der Naturwissenschaften“

von

Markus Paul Heckschen, M.Sc.

aus Marl

1. Gutachten: Prof. Dr. Björn Sothmann
2. Gutachten: Prof. Dr. Bärbel Rethfeld

Tag der Disputation: 13. Juni 2024

DOI: 10.17185/duepublico/82104
URN: urn:nbn:de:hbz:465-20240619-150444-3

Zusammenfassung

Auf der Nanoskala können Ladungsträger vielfältige zeitabhängige Transporteffekte zeigen. Diese Transporteffekte sind das Ergebnis von Nichtgleichgewichtssituationen. Die Art des Nichtgleichgewichts sowie das spezifische System beeinflussen den Transport der Ladungsträger. In dieser Arbeit untersuchen wir einerseits die Dynamik der Paaramplitude in einem Supraleiter-Quantenpunkt-Hybrid und andererseits den Transport sowie die Relaxation photoangeregter Elektronen in einer Fe/Au-Heterostruktur, welche als konkrete Beispiele für zeitabhängigen Transport im Nanobereich dienen.

Die Paaramplitudendynamik wird in einem Ein-Niveau-Quantenpunkt untersucht, welcher stark an zwei Supraleiter sowie schwach an einen Normalleiter gekoppelt ist. Aufgrund der Kopplung mit den Supraleitern werden im Quantenpunkt supraleitende Korrelationen induziert, die durch eine Paaramplitude charakterisiert sind. Zur Beschreibung der Paaramplitudendynamik verwenden wir eine Diagrammatik, bei der alle nicht wechselwirkenden Freiheitsgrade der Reservoire ausintegriert werden. Die diagrammatische Methode führt zu einer Mastergleichung, welche die zeitliche Entwicklung des Quantenpunkts durch seine reduzierten Dichtematrix beschreibt.

Wir untersuchen zwei verschiedene Nichtgleichgewichtsszenarien. Im ersten Szenario wird das System einem Quench unterzogen, der eine vielfältige Paaramplitudendynamik auslöst. Die Dynamik besteht aus einer Oszillation, bedingt durch resonant tunnelnde Cooper-Paare, und einem exponentiellen Zerfall, welcher durch dissipative Tunnelereignisse zwischen dem Quantenpunkt und dem Normalleiter entsteht. Im zweiten Szenario wird das System von außen angetrieben, um die Relaxation zu überwinden. Wir analysieren die Paaramplitude im adiabatischen und schnellen Limes. Für beide Szenarien können wir Oszillationen mit einer großen Amplitude anregen.

Um die Ausbreitung und Relaxation photoangeregter Ladungsträger in einer Fe/Au-Heterostruktur zu untersuchen, haben wir die Trajektorien von Elektronen simuliert. Mit einer Monte-Carlo-Simulation werden die Anzahl der Streuereignisse, die Energie und die Propagationszeit bestimmt. Unser Modell ist durch kürzlich durchgeführte Experimente motiviert. In den Experimenten werden die Elektronen mit einem Laser in der Eisenschicht angeregt. Die Elektronen bewegen sich durch die Grenzschicht und erreichen schließlich die Goldoberfläche, an der sie mit einem weiteren Laser gemessen werden. Durch die Pump-Probe-Methode erhält man Zugang zur ultraschnellen Zeitentwicklung der Elektronenverteilung. Die Ergebnisse aus unserer Simulation stimmen qualitativ mit denen aus dem Experiment überein. Mithilfe der Simulation interpretieren wir die Dickenabhängigkeit der Elektronverteilung. Indem wir die Anzahl der Streuereignisse gemäß der Simulation mit der experimentell bestimmten Elektronenenergie verknüpfen, identifizieren wir das Transportregime der Elektronen, das entweder ballistisch oder superdiffus ist.

Darüber hinaus berechnen wir die Dynamik der Elektronenverteilung in derselben Probe mit Hilfe der Boltzmann-Gleichung in Kombination mit diffusem Transport. Durch den diffusiven Transport ändert sich die Dickenabhängigkeit der Elektronenverteilung signifikant. Daher sind schichtdickenabhängige Messungen in der Lage, zwischen den verschiedenen Transportregimen im Experiment zu unterscheiden. Durch die Simulation und die diffusive Berechnung erhalten wir ein vollständiges Bild der Transporteffekte im ballistischen, superdiffusiven und diffusiven Regime.

Summary

At the nanoscale, multifaceted time-dependent transport effects of charge carriers can occur. In general, these transport effects are the result of nonequilibrium conditions which tend towards the equilibrium state. The nature of the nonequilibrium conditions as well as the underlying system affect the transport of the charge carriers. In this thesis, we study the pair-amplitude dynamics in a superconductor-quantum dot hybrid and the propagation and relaxation of photoexcited electrons in a Fe/Au heterostructure as specific examples of nanoscale time-dependent transport.

The pair-amplitude dynamics is studied in a single-level quantum dot which is coupled strongly to two superconducting leads. In addition, the dot is tunnel coupled to a normal conductor. The coupling to the superconductors induces superconducting correlations in form of a pair amplitude on the quantum dot. We describe the pair-amplitude dynamics with a real-time diagrammatics approach where all noninteracting degrees of freedom of the leads are integrated out. The diagrammatic method yields a master equation that describes the time evolution of the quantum dot in terms of its reduced density matrix.

We consider two different nonequilibrium scenarios. First, a quench which starts rich pair-amplitude dynamics consisting of an oscillation arising from resonantly tunneling Cooper pairs and an exponential decay due to dissipative tunneling events between the dot and the normal conducting lead. Second, the system is externally driven to overcome the relaxation. We discuss the response of the pair amplitude in the adiabatic and in the the fast-driving limit. For both scenarios, we can excite oscillations of the pair amplitude with a large amplitude.

To study the propagation and relaxation of photoexcited charge carriers in a Fe/Au heterostructure, we compute numerically the trajectories of electrons propagating from the Fe/Au interface to the Au surface. More precisely, the final energy and propagation time is determined within the framework of a Monte-Carlo simulation. Our work is motivated by recent experiments on a Fe/Au heterostructure. Here, the electrons are excited with a back-pump laser in the Fe layer, injected into the Au layer and finally measured by a probe laser on the Au surface. Due to the pump-probe method access to the ultrafast time evolution of the hot electron distribution is gained. Our results match with the experimental results on a qualitative level. With the detailed information about the relaxation and propagation dynamics in the simulation, it is then further possible to interpret the thickness dependence of the electron distribution. With our simulation, we are able to identify the transport regime of the electrons which is either ballistic or superdiffusive.

In addition, we calculate the dynamics of the electron distribution in the same sample using the Boltzmann equation combined with diffusive transport. Due to the diffusive regime, the thickness dependence of the electron distribution changes significantly. Hence, thickness-dependent measurements are able to distinguish between the different transport regimes in the experiment. With both the simulation and the diffusive calculation, we get a full picture of the transport effects in the ballistic, superdiffusive and diffusive regime.

Contents

1. Introduction

The discovery of electricity changed human life centuries ago. A key technology for society are artificial light sources. The first kind of such light sources is the light bulb. The current flow of charged particles through a wire heats it up due to Joule heating. The hot wire starts glowing according to Planck's radiation law and emits photons in the visible spectrum. Today, the light bulb disappears due to its small energy efficiency. It is substituted by the more efficient light emitting diode (LED). Nevertheless, there are still applications using Joule heating like the kitchen stove.

Hans Christian Ørsted discovered in 1820 that an electric current generates a magnetic field [1]. A simple application for this phenomenon is a wire that is arranged in a coil. The coil serves as a powerful electromagnet whose field strength can be tuned by the strength of the charge current [2]. Faraday discovered that the opposite process by which a time-dependent magnetic flux induces an electric voltage is possible as well [3]. This leads to the development of electric generators and electric motors. The latter are a key technology for several large scale applications in industry and small scale in robotics. Electric motors play a crucial role in initiating a shift in the transportation sector away from fossil fuels toward sustainable, eco-friendly alternatives to face today's biggest global challenge: climate change.

The transfer of electric energy to magnetic energy and vice versa can be analyzed in LC circuits. In such circuits, a coil is combined with a capacitor. The energy inside the circuit is either stored electrostatically in the capacitor or in the magnetic field of the current-carrying coil. The periodic transfer of energy between capacitor and coil results in an alternating current flowing through the LC circuit. Due to the continuous acceleration of charged particles, electro-magnetic waves are emitted from the device. This principle is the basis for today's telecommunication devices. Beginning with the telegraph, the development leads towards every-day applications like the radio, television and mobile internet [2].

Turning back to the transport of charged particles in circuits, the demand for manipulating the current flow in circuits arise. Transport in semiconductors is dramatically different from that in metallic conductors. Manipulating the transport properties of semiconductors by doping leads to the development of diodes and transistors. Diodes block transport in one direction while allowing the charge current to flow in the opposite direction. Transistors are three-terminal devices which allow a current flow between two terminals (emitter and collector) if a certain voltage is applied at the third terminal (base). These characteristics make it possible to build logic circuits and gates. Therefore, the transistor is the most important component for microelectronic devices like computers.

It seems to be impossible to substitute the computer and other microelectronic devices from today's society. Computers support tasks of different kinds e.g. administrative tasks, media design, controlling of machines, calculations/simulations and many more. Thereby, the demand for the computation power and time rises continuously in

each of its task fields. Besides designing supercomputers which demands for a lot of physical space, there are different approaches to increase the power of computers. One possibility is the downscaling of the components to achieve more calculation power on the same area. The computer's central processing unit is an example of such a development. The number of transistors on a single processing unit is rising exponentially. In other computer components, new technologies are developed to increase power and capacity. The hard drive disc is a current example where a new technology is in development. So far, the digital data is stored in discrete areas of the hard drive [4]. Since the capacity growth of hard drive discs is slowing down it is currently discussed to store the data in magnetic domain walls which further downscale the required space and speeds up the data processing [5].

Another demand on electronic devices is the energy efficiency. Facing the current challenges regarding the sustainable usage of resources and the environment, it is necessary to search for alternative materials and concepts to design electronic components. Understanding the underlying transport properties of the energy-carrying particles is of key importance for the right choice of material and design.

A charged particle can be transported either ballistically, superdiffusively or diffusively. Ballistic transport is characterized by propagation at a constant velocity without scattering. Such a transport behavior seems to be odd in a metallic conductor since the electrons interact with each other and the crystal lattice due to Coulomb interactions. The interactions happen on a certain timescale and if a shorter time is considered, the electron has not yet interact and propagates therefore ballistically. However, such a point of view is only meaningful when the process of interest, e.g. the transport through a material section, happens also on timescale which is much smaller than the interaction timescale. A prominent example of ballistic transport in a mesoscopic system is the quantum Hall effect [6]. If a strong magnetic field is applied on a two-dimensional electron gas, this leads to the formation of unidirectional chiral edge channels [7]. As a result, backscattering processes are prohibited and the Hall resistance becomes a quantized property.

The diffusive transport regime is characterized by multiple collisions of the particle with other particles and phonons in the material. A basic example of a diffusive charge transport is a DC current through a metallic conductor. The DC current is generated by an applied bias voltage to the conductor. Thus, there is an electric field inside the conductor which accelerates the electrons which gain kinetic energy. The charge carriers collide multiple times with other electrons, phonons and impurities in the conductor and exchange energy. Since energy is exchanged with the crystal lattice, it heats up. This so called Joule heating is the basic principle of a light bulb, see above. Another type of diffusive transport is heat transfer. If a metallic plate has a hot left side and a cold right side the temperature will equalize over time due the diffusive transport of phonons.

Regarding the energy efficiency, it is of course favorable to design electronic devices where only ballistic transport occurs. In a diffusive transport regime, a share of the energy is transferred, e.g., to the crystal lattice and, hence, is no longer usable for the device. In addition, the devices might need a cooling system which decreases the energy efficiency further. A deeper understanding of the different transport regimes is required here.

An intriguing question is how a transition from the ballistic to diffusive regime can

be defined and identified. On a microscopic level, ballistic transport is the motion of a particle without any collisions. Diffusive transport, in contrast, is governed by multiple collisions. The transport of a single particle under diffusive conditions can be described by a random walk. If a bias is applied to the system, the full ensemble of particles would shift according to the nonequilibrium driving force. However, a particle trajectory with only a few collisions would be classified as neither ballistic nor diffusive. In literature, this intermediate transport regime is called superdiffusive. However, there is no exact definition of the transition points to the ballistic and diffusive regime on the microscopic level. In addition, it is challenging to identify the different regimes in an experiment since there it is not possible to select single electrons from the ensemble.

Charge transport arises from nonequilibrium conditions in the system. Besides applying a voltage or temperature bias to the conductor there are also other possibilities to bring a system out of equilibrium. Inducing a nonequilibrium particle density distribution is another option to induce transport processes. Pumping a metal with a laser is an excellent way to introduce a nonequilibrium distribution of hot electrons in the system. In so called pump-probe experiments, a pump laser is followed subsequentially by a laser pulse which probes the hot electrons. The photoemitted electrons can be detected afterwards. The time delay between the pump and probe pulse can be arranged in the setup giving access the time evolution of the density distribution. The time resolution is determined by the accuracy of the delay stage in the experimental setup as well as the pulse width of the pump and probe laser pulses. In the last decades, laser setups generating fs laser pulses have been developed. At these ultrashort timescales, it is possible to investigate the relaxation of hot electrons into equilibrium.

If the pump and probe pulses are spatially separated, access to the transport properties is gained. An interesting sample in which transport and relaxation dynamics can be analyzed by pump-probe experiments are heterostructures, e.g., an iron-gold (Fe/Au) layered material where a single-crystalline gold layer is grown on an iron single crystal by molecular beam epitaxy. If the system is pumped on the iron side of the sample the pump pulse is absorbed almost completely by the electronic system in the iron layer [8]. When there is a perfectly single-crystalline interface most of the electrons are transmitted into the gold layer. Thus, in this heterostructure an electron distribution is rapidly injected into a homogeneous gold layer giving a nonequilibrium distribution of charge carriers whose transport mechanisms can be studied by probing the system from the gold side. Additionally, the Fe/Au interface is only transparent to electrons with an energy in a certain range [9]. This gives the opportunity to inject the electrons within a certain energy window and study relaxation and transport dynamics accordingly. The analysis of the electron dynamics in the Fe/Au model system provides new insights to the transport regimes.

Turning back to the development of computers, one needs also to discuss a new generation of computers which is currently in development - the quantum computers. The key advantage of quantum computers over classical computers would be the usage of quantum states which can be explained by considering the following example. A classical computer can represent any number between 0 and 255 using eight bits. In contrast, a quantum computer would be able to represent the same numbers simultaneously using eight quantum bits. With a few hundred entangled quantum bits more numbers than there are atoms in the universe can be represented [10]. Hence, the calculation power of quantum computers is in general higher compared to classical

computers depending on the specific field of application.

The main idea of a quantum bit is to use the superposition of quantum states. Thus, different from the classic bit not only the state 0 and 1 are possible but also any superposition of them. The design of a quantum bit is a challenging endeavor since a detailed knowledge about the underlying quantum effects is necessary. Superconductors hosts many interesting quantum phenomena that are promising for the construction of quantum bits on a macroscopic system size. One example is the formation of Cooper pairs. The Cooper pairs interact with normal conductors and insulators via Andreev reflections and the Josephson effect which we will explain in more detail later on. During an Andreev reflection a Cooper pair is either formed or split. In the latter case the superconductor act as a source for spin-entangled electrons which can be spatially separated via a crossed Andreev reflection [11]. Due to the Josephson effect interesting phenomena occur at the interface between two superconductors. Such a setup is also called Josephson junction. Here, the Josephson current can be controlled by the superconducting phases.

Further interesting transport effects occur by the combination of superconductivity with a sort of interaction, e.g. Coulomb interaction. In quantum dots, strong Coulomb interactions can occur. In addition, quantum dots can be coupled to superconductors forming a Josephson junction. Due to the coupling, superconducting correlations are induced on the quantum dot. This allows, on the one hand, to study transport effects and, on the other hand, bring additional degrees of freedom like the level position of the dot into play. The superconducting correlations on the dot can be studied by the pair amplitude which is related to the collective motion of the Cooper pairs in the superconducting condensate.

In this thesis, we will study both the nonequilibrium transport and relaxation dynamics of hot electrons in a Fe/Au heterostructure and the pair-amplitude dynamics in strongly-coupled superconductor-quantum dot hybrids. The thesis is structured as follows. In Chapter 2, we will introduce the components of our two models. For the superconductor-quantum dot hybrid, we will start with an introduction of superconductivity and basic transport phenomena in quantum dots. Afterwards, the transport phenomena present in hybrid structures are discussed. Experiments studying transport and relaxation in Fe/Au and other similar heterostructures are introduced. Subsequentially, theoretical approaches to model the transport and relaxation dynamics are reviewed. A special focus relies on the Boltzmann transport equation. We give a detailed introduction into an analytic calculation of the relaxation of hot electrons via electron-electron scattering published in Ref. [12]. Chapter 2 is closed by a brief introduction of possible transport regimes of electrons in metals.

In Chapter 3, the superconductor-quantum dot hybrid used to study the pair-amplitude dynamics is introduced. We begin with an explanation of the basic system Hamiltonian in the effective representation of the superconductor-quantum dot hybridization. Hereby, we use the infinite-gap limit which is a convenient description of subgap physics in strongly-coupled devices. The transport dynamics of the devices is calculated by a master equation. The derivation of the master equation with a real-time diagrammatic approach is shown in detail for our specific system. For a physically more intuitive picture, the master equation is transformed into the pseudospin representation. The relation between the pseudospin components and the Josephson and Andreev current is explained. The currents give experimental access to

the pair-amplitude dynamics in such systems.

The results are presented subsequentially. We investigate two types of pair-amplitude dynamics in the system. The first type is the relaxation of the pair amplitude from a quenched state into the nonequilibrium stationary state. Here, we first calculate the time evolution as a function of the initial quench from the master equation and, afterwards, analyze the resulting dynamics in the framework of the pseudospin. The second type of pair-amplitude dynamics is the periodic driving of the system by an external variation of the parameters. The two limits which are driving the system adiabatically and fast are considered. In the adiabatic limit, the evolution of the pair-amplitude is approximated by the stationary master equation. In the fast driving limit, the master equation is decomposed into its Fourier components with respect to the driving force. For both driving schemes, we find pronounced oscillations of the pair amplitude. In the limit of adiabatic driving, we are able to link the pair-amplitude oscillation directly to the Higgs mode in bulk superconductors. In the fast driving limit, we find that the quantum dot is able to follow the fast external driving up to high frequencies. In the end of the chapter, the results are summarized and a conclusion is drawn.

In Chapter 4, we discuss the transport dynamics in the Fe/Au model system. In the beginning, we set up a trajectory-based Monte-Carlo simulation that follows the path of single electrons through a sample. We extract the energy and time-dependent intensity spectra which are compared qualitatively to the experimental results. Subsequentially, the effective electron velocity and its insights into the transport regimes of the electrons is discussed. Afterwards, we introduce the electron passage velocity and discuss the corresponding results. We explain the apparently higher effective velocity of scattered electrons in thicker Au sample by analyzing the shift of the injection angle with increasing sample thickness. Beyond ballistic and superdiffusive transport, we introduce a diffusive transport model based on the Boltzmann equation to show the similarities and differences of the energy- and time-dependent intensity spectra and the effective velocity. Finally, we discuss the transition between the diffusive and superdiffusive transport regime.

We close this thesis with a conclusion and short outlook on future data analysis with the methods presented here.

2. Nonequilibrium transport dynamics at the nanoscale

Here, we introduce the systems and their properties which we analyze in Chapter 3 and 4. We focus on the transport features of the corresponding systems. In this thesis, we study on the one hand the pair-amplitude dynamics of superconductor-quantum dot hybrids. Therefore, we begin with an introduction of superconductivity in this chapter. Fundamental for the description of superconductivity is the microscopic theory by Bardeen, Cooper and Schrieffer (BCS) which was awarded by a Nobel prize. We introduce the phenomenological description by the Ginzburg and Landau too since it allows us to interpret collective excitations of the superconducting condensate in terms of the Higgs and Nambu-Goldstone mode. Quantum dots which are coupled to superconductors exhibit interesting transport phenomena. In order to understand the origin of the transport phenomena, we introduce the basic transport properties of single-level quantum dots. Consecutively, we discuss special transport features of superconductor-quantum dot hybrids.

On the other hand, our second research focus is the spatio-temporal electron propagation dynamics in an iron-gold (Fe/Au) heterostructure. In Chapter 2.4 we introduce the development of Fe/Au heterostructures as a model system to study spintronic principles. Afterwards, we discuss pump-probe experiments with Fe/Au samples which lead to a discussion of the occurring transport features in metals. We introduce theoretical models to predict and describe the electron dynamics. A special focus relies on the Boltzmann equation and its solution by Kabanov [12]. We close this chapter with a brief discussion of the different transport regimes.

2.1. Superconductivity

Superconductivity is a fascinating material property that has been discovered more than a hundred years ago. After a successful attempt to liquify Helium, Kammerlingh-Onnes studied the electrical conductance of materials near zero temperature in 1911 [13]. It turns out that the electric resistance of some materials vanishes below a critical temperature. Moreover, the materials become perfect diamagnets which are able to shield a magnetic field from penetrating inside up to a critical field strength. The shielding is called Meisner effect. Due to the new properties, superconducting is a new phase. Albeit that old, superconductivity is still an intriguing topic for scientists today [14].

Superconductors are already tested in every day applications, e.g. as conductors for the power grid, see the pilot project [15]. Here, high-temperature superconductors cooled with liquified nitrogen substitute a much larger conventional copper conductor. The superconductor has the advantage that it transports the electricity lossless and with a higher current density. For the operation, it is important that the critical current

density is not exceeded since the superconductor will be destroyed otherwise. Besides the reduced required space for the conductor, the project tests if the higher transport efficiency leads to a higher total efficiency by taking the additional energy demand due to cooling into account. Another application of superconductivity are superconducting coils which are powerful electromagnets that have been developed many decades ago [16] and generate magnetic fields up to 45.5 T [17]. Powerful magnets are the foundation for magnetic resonance imaging in medicine, nuclear magnetic resonance in pharmacy and particle acceleration e.g. in CERN. In this type of accelerators, the superconducting magnets are used for multiple applications. On one hand, powerful magnets are used for accelerating the particle and, on the other hand, the magnetic fields are used for steering and focusing the beam.

The potential use of superconductors in quantum computers are discussed in numerous papers [18–22]. The key advantage of superconducting quantum bits is the lossless transport which provides a reduction in the loss of information. On the other side, superconducting phenomena like the Josephson effect provides the possibility to build nonlinear inductors. Such a circuit element leads to quantum-mechanical energy levels which can be isolated to get two computational basis states $|0\rangle$ and $|1\rangle$. The transition energy of these energy levels is in the microwave range. Therefore, it is possible to control the quantum bit externally [18].

Forty years after the discovery of superconductivity, the first phenomenological theory was proposed by Ginzburg and Landau in 1950 [23]. The Landau theory of the 2^{nd} order phase transition finds an approximate form of the free energy near the phase transition at T_c. In the absence of electromagnetic fields and gradients, the free energy is given by

$$f_\text{S} - f_\text{N} = \alpha|\psi|^2 + \frac{1}{2}\beta|\psi|^4. \tag{2.1}$$

This is a series expansion of the free energy in powers of the order parameter $|\psi|^2$ which gives the local density of superconducting electrons. The order parameter is zero on the high-temperature side of the phase transition and different from zero on the low-temperature side. If the order parameter is zero, there are no superconducting effects on the free energy. For a superconducting condensate with a nonzero number of superconducting electrons the minimum of the free energy occurs at finite ψ. Therefore, the parameter α needs to be smaller than zero and β needs to be positive. Only then, the formation of a superconducting condensate is stable. To describe superconductivity, Ginzburg and Landau use a phenomenological ansatz. They introduce the order parameter as a complex number $\Delta e^{i\varphi}$, where Δ is the absolute value of the order parameter and φ the superconducting phase. The Ginzburg-Landau theory describes superconductor properties close to their critical temperature well since it is an approximation close to the phase transition.

Even though the Ginzburg-Landau theory explains many experiments, it is a phenomenological approach that lacks of an underlying microscopic description until the BCS theory by Bardeen, Cooper and Schrieffer was established in 1957 [24]. The BCS theory is a microscopic theory that is still the foundation of today's understanding of superconductivity. This theory provides results that agree excellently with results from experiments and was honored in 1972 with the Nobel prize. The theory is very powerful in describing superconducting phenomena like the temperature dependence of the gap, ultrasonic attenuation and nuclear relaxation.

The basis of the BCS theory is the effective attraction between two electrons mediated by electron-phonon coupling. Fröhlich proposed in 1950 the importance of the electron-phonon coupling for superconductivity [25]. Intuitively, one expects the electrons to repel each other due to the Coulomb force. To understand the attraction with a simple model, we consider an electron propagating through a crystal lattice. Due to the Coulomb force, the electron attracts the positively charged ions of the crystal lattice leading to a local higher density of the positively charged ions. This positively charged localization of the crystal lattice attracts a second electron. In total, there is a net attraction between the two electron mediated by the crystal lattice. Cooper showed that the Fermi sea is unstable with respect to pair formation in presence of arbitrarily weak attractive interactions. The electrons condense into Cooper pairs where the electrons have opposite momenta and form a spin-singlet state in a second-order phase transition. The size of the Cooper pair is given by the coherence length of the superconducting material $\xi = \hbar v_\mathrm{F}/\Delta$ where $\hbar$ is the reduced Planck constant, v_F the Fermi velocity and Δ the absolute value of the order parameter. The size of a Cooper pair in aluminum at $T = 0$ is $1.6\,\mu$m [26].

To describe superconductivity, the coupling between electrons and phonons needs to be taken into account. In the BCS theory, the influence of phonons is integrated out which results in an effective electron-electron coupling, the Cooper pairing. The kinetic energy of the electrons as well as the pairing potential which forms the Cooper pairs are used to describe a superconductor. The pairing Hamiltonian is given by

$$H = \sum_{\mathbf{k}\sigma} \xi_\mathbf{k} c^\dagger_{\mathbf{k}\sigma} c_{\mathbf{k}\sigma} + \sum_{\mathbf{kl}} V_\mathbf{kl} c^\dagger_{\mathbf{k}\uparrow} c^\dagger_{-\mathbf{k}\downarrow} c_{-\mathbf{l}\downarrow} c_{\mathbf{l}\uparrow}. \tag{2.2}$$

Here, $\xi_\mathbf{k}$ denotes the particle energy above the Fermi energy, $c^\dagger$ and c are the creation and annihilation operators. $V_\mathbf{kl}$ gives the scattering of electrons from state $\mathbf{l}$ to $\mathbf{k}$. For simplification, a mean-field approximation is made by a canonical transformation which we summarize below according to Ref. [23]. For that, we use that the operators $c_{-\mathbf{l}\downarrow} c_{\mathbf{l}\uparrow}$ have a nonzero expectation value $b_\mathbf{k}$. Thus, the product of the operators can be written as

$$c_{-\mathbf{l}\downarrow} c_{\mathbf{l}\uparrow} = b_\mathbf{k} + (c_{-\mathbf{l}\downarrow} c_{\mathbf{l}\uparrow} - b_\mathbf{k}), \tag{2.3}$$

where the bracket gives fluctuations from the mean value. Inserting this into the pairing Hamiltonian and neglecting second order fluctuations gives the mean-field Hamiltonian

$$H = \sum_{\mathbf{k}\sigma} \xi_\mathbf{k} c^\dagger_{\mathbf{k}\sigma} c_{\mathbf{k}\sigma} + \sum_{\mathbf{kl}} V_\mathbf{kl} \left(c^\dagger_{\mathbf{k}\uparrow} c^\dagger_{-\mathbf{k}\downarrow} b_\mathbf{l} + b^\dagger_\mathbf{k} c_{-\mathbf{l}\downarrow} c_{\mathbf{l}\uparrow} - b^\dagger_\mathbf{k} b_\mathbf{l} \right). \tag{2.4}$$

Hereby, the $b_\mathbf{k}$ are determined in a self-consistent calculation, such that

$$b_\mathbf{k} = \langle c_{-\mathbf{k}\downarrow} c_{\mathbf{k}\uparrow} \rangle . \tag{2.5}$$

The energy gap is defined as

$$\Delta_\mathbf{k} = -\sum_\mathbf{l} V_\mathbf{kl} b_\mathbf{l}, \tag{2.6}$$

which gives the nondiagonal Hamiltonian in the mean-field approximation

$$H_\mathrm{mf} = \sum_{\mathbf{k}\sigma} \xi_\mathbf{k} c^\dagger_{\mathbf{k}\sigma} c_{\mathbf{k}\sigma} - \sum_\mathbf{k} \left(\Delta_\mathbf{k} c^\dagger_{\mathbf{k}\uparrow} c^\dagger_{-\mathbf{k}\downarrow} + \Delta^\dagger_\mathbf{k} c_{-\mathbf{k}\downarrow} c_{\mathbf{k}\uparrow} - \Delta_\mathbf{k} b^\dagger_\mathbf{k} \right). \tag{2.7}$$

As shown independently by Bogoliubov [27] and by Valatin [28], this Hamiltonian can be diagonalized by a linear transformation given by

$$c_{\mathbf{k}\uparrow} = u_{\mathbf{k}}^{\dagger}\gamma_{\mathbf{k}\uparrow} + v_{\mathbf{k}}\gamma_{\mathbf{k}\downarrow}^{\dagger}, \tag{2.8}$$

$$c_{-\mathbf{k}\downarrow}^{\dagger} = -v_{\mathbf{k}}^{\dagger}\gamma_{\mathbf{k}\uparrow} + u_{\mathbf{k}}\gamma_{\mathbf{k}\downarrow}^{\dagger}. \tag{2.9}$$

Here, $\gamma_{\mathbf{k}}$ are defined as new Fermi operators for the linear transformation. The numerical coefficients $u_{\mathbf{k}}$ and $v_{\mathbf{k}}$ fulfill the normalization condition $|u_{\mathbf{k}}|^2+|v_{\mathbf{k}}|^2 = 1$. The Fermi operator $\gamma_{\mathbf{k}\uparrow}$ aims to the decrease the system momentum by $\mathbf{k}$ and reduce the system spin S_z by $\hbar/2$ by creating and annihilating the corresponding electrons. The operator $\gamma_{\mathbf{k}\downarrow}$ aims for the opposite, thus increasing the system momentum by $\mathbf{k}$ and the spin S_z by $\hbar/2$. By inserting the new operators into the nondiagonal mean-field Hamiltonian and choosing the coefficients $u_{\mathbf{k}}$ and $v_{\mathbf{k}}$ such that the nondiagonal elements vanish, we finally obtain the diagonal mean-field Hamiltonian which is given by

$$H_{\mathrm{mf}} = \sum_{\mathbf{k}} \left(\xi_{\mathbf{k}} - E_{\mathbf{k}} + \Delta_{\mathbf{k}} b_{\mathbf{k}}^{\dagger}\right) + \sum_{\mathbf{k}} E_{\mathbf{k}} \left(\gamma_{\mathbf{k}\uparrow}^{\dagger}\gamma_{\mathbf{k}\uparrow} + \gamma_{\mathbf{k}\downarrow}^{\dagger}\gamma_{\mathbf{k}\downarrow}\right). \tag{2.10}$$

The first sum denotes the condensation energy of Cooper pairs. If the condensation energy is less than zero, Cooper pair formation is favored. $\xi_{\mathbf{k}}$ is the particle energy above the Fermi energy. The eigenstates of a superconductor, see second sum, described by $\gamma_{\mathbf{k}}$ are so called Bogoliubons which are quasiparticle excitations. The excitation energy of quasiparticles is given by

$$E_{\mathbf{k}} = \left(\xi_{\mathbf{k}}^2 + |\Delta_{\mathbf{k}}|^2\right)^{1/2}. \tag{2.11}$$

Hence, $2\,|\Delta_{\mathbf{k}}|$ is an energy gap centered at the Fermi energy. The gap gives the required energy to excite quasiparticles in the superconductor. The quasiparticles are a superposition of the electron and hole wave function in the superconductor. The superposition becomes strongest for $\epsilon = \Delta$ and vanishes for $\epsilon \gg \Delta$. The quasiparticles are either of an electron-like or hole-like nature depending on the dominating wave function. Since there are no free single-particle states inside the gap, the only way for electrons to enter the gap is by forming a Cooper pair at the Fermi energy.

The Cooper pairs are described by a macroscopic wave function $\Delta e^{i\varphi}$. This description is analogue to the earlier introduced Ginzburg-Landau theory. The order parameter is a dynamic quantity which can exhibit collective oscillations such as the Nambu-Goldstone mode and the Higgs mode. The free energy of the Ginzburg-Landau theory, see Eq. (2.1), is the best way to understand these oscillations. Plotting the free energy as a function of the order parameter in a complex space gives a Sombrero potential, see Figure 2.1. The Nambu-Goldstone mode is a gapless excitation of the superconducting phase φ in the minimum of the sombrero potential while the Higgs mode is a gapped excitation which oscillates around the minimum of the free energy. In bulk superconductors, the Nambu-Goldstone mode is shifted to the plasma frequency due to the Anderson-Higgs mechanism [29–31]. Pekker and Varma give an intuitive picture in their review [32] which takes into account the sombrero potential, see Fig. 2.1. Since the phase mode is energy invariant, there exists a zero energy or massless mode of fluctuations of the density current in the long wavelength limit. As pointed out by Anderson [29], such density fluctuations occur in superconductors at the plasmon

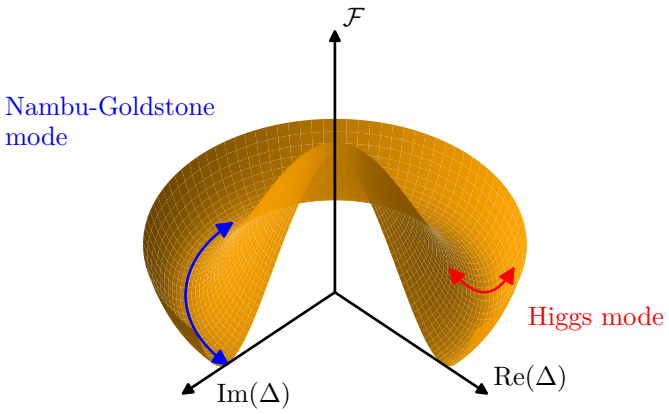

Figure 2.1.: Sombrero potential: Free energy as a function of the order parameter in a complex parameter space. The blue arrow indicates the gapless Nambu-Goldstone mode and the red arrow shows the gapped excitation of the Higgs mode.

energy due to the large interaction range of the Coulomb force. Hence, the Higgs mode is the only remaining collective, low-energy excitation in bulk superconductors. Since the Higgs mode coincides with the energy of the superconducting gap, the frequency of the Higgs mode is

$$\hbar\omega_{\mathrm{H}} = 2\Delta, \tag{2.12}$$

for zero crystal momentum. Since this energy marks the lower boundary of the quasiparticle excitations, the decay into single-quasiparticle excitations is suppressed. For a nonzero momentum, the Higgs mode can decay into quasiparticle excitation [33].

The experimental detection of the Higgs mode is a challenging endeavor. The Higgs mode is charge neutral and couples only quadratically to external electromagnetic fields. Therefore, large field strengths are required to excite the Higgs mode. In addition, the excitation energy in typical BCS superconductors lies in the THz range. Suitable laser sources and the corresponding detectors have been developed only recently after a long time of development in other fields of terahertz physics [34]. The Higgs mode excitation energy is the same as for quasiparticles. Thus, the Higgs mode is masked by quasiparticles if the excitation of the latter is not suppressed. The first indirect detection of the Higgs mode has been reported in superconductors that host charge density waves [35, 36]. Here, the Higgs mode becomes Raman active due to electron-phonon coupling. In a Raman spectrum, the coupling appears as an additional peak close to the energy of the superconducting gap.

With powerful THz lasers, it is possible to detect the Higgs mode directly with pump-probe experiments [37]. The experimentally observed oscillation of the electromagnetic probe signal is explained theoretically in terms of Anderson pseudospin dynamics in the x-y plane in a BCS model [38] and by gauge-invariant kinetic equation of superconductivity [39]. The Higgs mode has also been probed by its third-order nonlinear optical response which provides a clear distinction between the Higgs mode and quasiparticle excitations [40, 41]. Recently, the Higgs mode has also been detected in strongly-interacting fermionic superfluids [42]. Further theoretical studies focus on the Higgs mode in unconventional d-wave superconductors [43, 44], and on the cou-

pling of the Higgs and Leggett modes in two-gap superconductors [45]. The Leggett phase mode corresponds to fluctuations of the interband phase difference. Recently, the Higgs mode has been used to amplify incident light pulses [46]. For current reviews on the Higgs mode in superconductors see Refs. [32, 33].

2.2. Quantum dots

Quantum dots are zero-dimensional objects that interact with their environment. Different types of quantum dots are realizable. For example, nanoparticles which can be synthesized with an arbitrary size, acts as quantum dots. The discovery and the synthesis of quantum dots was awarded with a Nobel prize in 2023. Another type of quantum dots are solid state quantum dots. These quantum dots are small islands of a different material than the surrounding environment. Quantum dots have many interesting electronic, optoelectronic and other phenomena due their zero-dimensional nature. The confinement leads to a limited number of electrons that are able to occupy the quantum dot. Therefore, the quantum dot has discrete energy states and a discrete density of states. The level position of quantum dots is determined by its size. This can be understood by imaging that an electron wave needs to fit into the quantum dot. The smaller the quantum dot the less space has the electron wave and the higher is the energy the electron absorbs and emits. Consequently, quantum dots can be used as a light source that emits photons of any wavelength. [47–51]. This characteristic has already been used to produce every-day applications like QLED TVs [52]. Other applications based on quantum dots as light source are quantum dot lasers [53]. Quantum dot lasers have several advantages over bulk semiconductor lasers. At first, the wavelength is almost arbitrarily tuneable by the spatial extent of the used quantum dots. The size quantization leads to an increase in the density of states near the band edges. Consequently, the lasing threshold current density is decreased from 1050 A/nm in bulk lasers to 45 A/nm in quantum dot lasers. In addition, the zero-dimensional nature of quantum dots leads to a strong overlap of the electron and hole wave function and, thus, to a high recombination rate. Finally, the emitted wavelength of quantum dots are stable up to room temperature if the quantum dot is suitably small that the first energy level above the ground state is not thermally reachable [54].

The opposite physical process where the quantum dot absorbs photons to create an electron-hole pair is exploited to produce solar cells based on quantum dots [55]. Key advantage for quantum dot solar cells is again the size-tuneable wavelength. Exploiting this property, it is possible to design a solar cells which is able to absorb the full spectrum of sunlight without using a bunch of different materials. See Ref. [47] for a review on quantum dot solar cells.

Besides these multiphoton applications quantum dots can also act as single-photon emitters [56–60], which are key for quantum information technologies [61]. Moreover, quantum dots play an important role in the development of quantum computing [62–64]. Various devices constructed with quantum dots like single-electron emitters which provide single electrons on demand [65] and spintronic devices [63, 66] provide the foundation to study quantum effects which can be exploited to possibly construct a quantum computer.

Before we focus on transport effects of quantum dots, we consider the properties of an isolated quantum dot. Due the small extent of the quantum dot, it has discrete

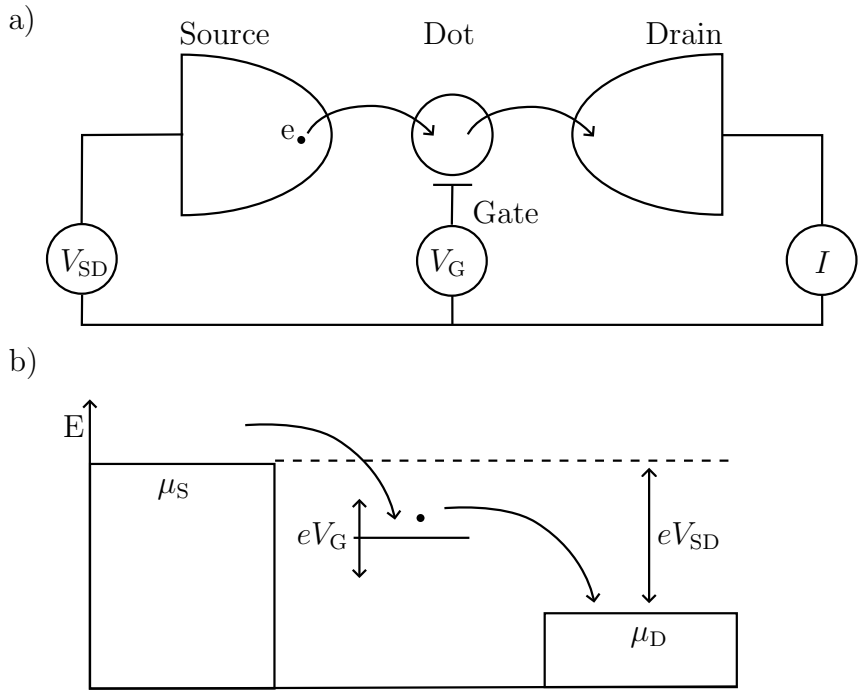

Figure 2.2.: a) Schematic sketch of a quantum dot coupled to a source and drain electrode. A voltage bias V_{SD} is applied on the electrodes. The current I flows through the dot. The level position of the quantum dot can be tuned with the gate voltage V_G. b) Energy diagram of the quantum dot coupled to source and drain electrode with a voltage bias of V_{SD}.

energy levels. Each energy level can be occupied by two electrons due to the Pauli exclusion principle. An electron that occupies the energy level of a previously empty quantum dot needs to have an energy ϵ that matches to the energy level of the quantum dot. In strongly-interacting quantum dots the second electron needs an energy

$$E = \epsilon + U, \tag{2.13}$$

to occupy the same energy level. The extra amount of energy U is required to overcome the on-site Coulomb repulsion.

In the following, we want to focus on the transport features of quantum dots which are relevant for the model we discuss in Chapter 3.1. For a general insight into the basic transport phenomena of a quantum dot, we consider a system in which a single-level quantum dot is coupled to a source and a drain electrode. The energy levels of the quantum dot can be tuned with a gate voltage. The system is sketched in Fig. 2.2 panel a). The voltage V_{SD} between the source and drain electrode yields a difference in the electrochemical potentials. There are three configurations of the level position of the dot. If the energy level of the quantum dot is energetically between the Fermi energy of source and drain electrode, see Fig. 2.2 panel b), an electron can tunnel from the source electrode onto the quantum dot. From here the electron can proceed tunneling to the drain electrode. In this case, a net current I can be measured between the source and drain electrode. If the dot level is tuned above the electrochemical potential of the source electrode μ_S it is not possible for the electron to tunnel onto the dot. In this case, the current flow between source and drain is blocked. Another configuration is when the energy level of the dot is tuned below the electrochemical

potential of the drain electrode μ_{D}. Here, an electron can tunnel either from the source or the drain electrode onto the quantum dot. It is also possible that a second electron tunnel onto the quantum dot if it has enough energy to overcome the Coulomb force. Due to the Pauli exclusion principle the single-level quantum dot is with two electrons fully occupied and further current flow is blocked in this configuration.

When we consider the system in a low temperature regime there exist also another type of tunneling which is called cotunneling. Hereby, the energy level of the quantum dot is tuned below the electrochemical potentials of both source and drain electrode. As a starting point, we assume the dot to be single occupied. In a cotunneling process an electron from the electrodes tunnels onto the quantum dot and simultaneously the dot electron uses this energy to tunnel into one of the electrodes. Before recognizing that cotunneling is of another type of tunneling it was viewed as a limitation in the resolution of sequential tunneling which we have discussed above [67]. In addition, it also possible to find a transition from an empty to a doubly occupied quantum dot by a cotunneling event where two electrons tunnel coherently onto the dot. The opposite process is also possible when energy is introduced into the system such that the electrons can tunnel coherently from the dot to the electrodes.

2.3. Transport phenomena in hybrid structures

In this section, we discuss transport phenomena in more complex systems where normal conductors and superconductors are connected to a quantum dot. To go step-by-step, we start with simple junctions to introduce two important transport phenomena, the Andreev reflection and the Josephson current. For the Andreev reflection, we consider a normal conductor coupled to a superconductor with an order parameter Δ. We assume a transparent interface in between the conductors, see Fig. 2.3. Panel a) shows the incident of an electron with energy $E_{\mathrm{F}} + \epsilon$ at the normal conductor-superconductor interface. Here, ϵ denotes the energy of the electron above the Fermi energy E_{F}. The energy of the electron is inside the gap of the superconductor $2\,\Delta$. Since there are no free single-particle states available in the superconducting gap the electron forms a Cooper pair with another electron from the normal conductor. Due to charge and particle conservation the second electron leaves a hole in the normal conductor. The hole has an opposite momentum compared to the incident electron. The resulting process is an incident electron which is Andreev reflected as a hole by forming a Cooper pair in the superconductor.

The opposite process is marked in panel b) of Fig. 2.3. Here, the incident hole is Andreev reflected as an electron by destroying a Cooper pair in the superconductor. When the incident particle energy lies outside the superconducting gap, an additional transport process comes into play. The electron can be either reflected or transmitted at the interface to the superconductor. At first, we assume a barrier free junction between normal conductor and superconductor. The process is best understood by considering the dispersion relation of the free electrons in the normal conductor and the dispersion relation of the quasiparticles in the superconductor which is [23]

$$\epsilon(k) = \sqrt{\left[\frac{\hbar^2}{2m}\left(k^2 - k_{\mathrm{F}}^2\right)\right]^2 + \Delta^2}. \tag{2.14}$$

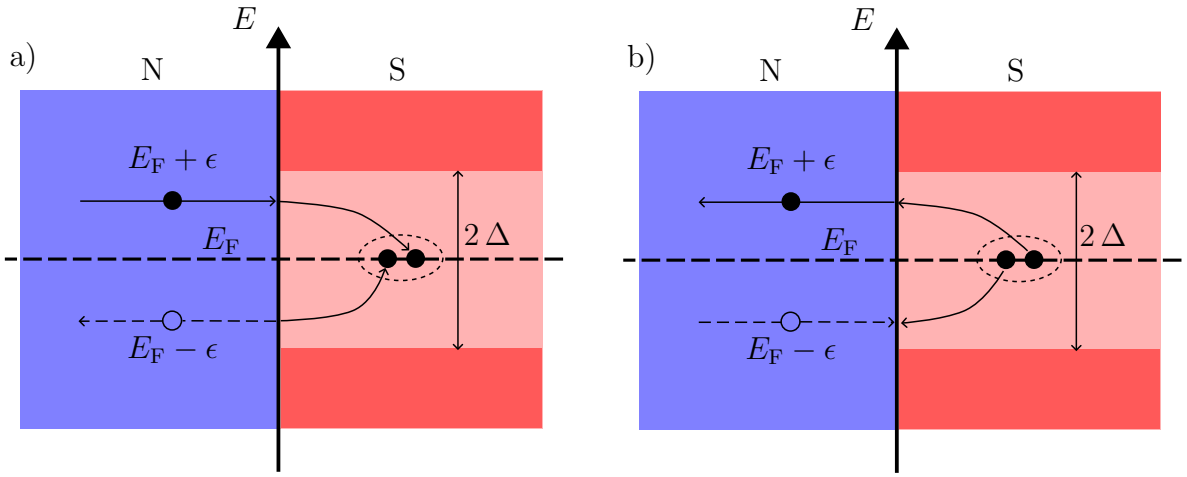

Figure 2.3.: Normal conductor-superconductor junction with a perfectly transparent interface. The extend in horizontal direction indicates the energy E of the particles. The dashed line shows the Fermi energy E_F. Here, Andreev processes below the gap of the superconductor 2Δ are considered. In a) an electron with energy ϵ above E_F is Andreev reflected as a hole with energy ϵ below E_F at the interface to the superconductor. In the superconductor the electrons form a Cooper pair. Panel b) shows the opposite process where an incident hole is Andreev reflected as an electron under destroying a Cooper pair.

The Fermi wave vector k_F denotes the wave vector where the transition from electron-like to hole-like quasiparticles occur.

The dispersion relations are given in Fig. 2.4. Here, blue line sections indicate electrons (electron-like quasiparticles) and red line sections holes (hole-like quasiparticles). The blue arrow in panel a) denotes an incident electron in the normal conductor. The electron can either be reflected as a hole or transmitted into the superconductor where it becomes an electron-like quasiparticle. In both cases, the direction of momentum cannot change since we assume a perfectly transparent interface. For a reflection, the electron needs to change the direction of the group velocity. Therefore, it can only be Andreev reflected as a hole (red arrow in panel a)) as already explained for the case when the electron energy is inside the gap. For a transmission both the direction of momentum and group velocity need to remain unchanged. Therefore the electron can only be transmitted as an electron-like quasiparticle into the superconductor, see blue arrow in panel b). When we introduce a finite barrier at the interface, more processes are possible. The barrier introduces the possibility of changing the direction of the momentum of the particle. In the example, sketched in Fig. 2.4, this allows the electron to be reflected as an electron as well as to be transmitted into a hole-like quasiparticle state.

The second transport phenomena has been proposed by Josephson in 1962 [68]. A good model system to visualize the Josephson effect is the superconductor - normal conductor - superconductor (SNS) junction, see Fig. 2.5. According to Josephson, a particle current I between the superconductors has three contributions

$$I = I_{qp}(V) + I_{AR}(V)\cos(\varphi) + I_{Jos}\sin(\varphi). \tag{2.15}$$

The first contribution to Eq. (2.15) is a dissipative current due to quasiparticles with an energy higher than the gap. These quasiparticles do not interact with the su-

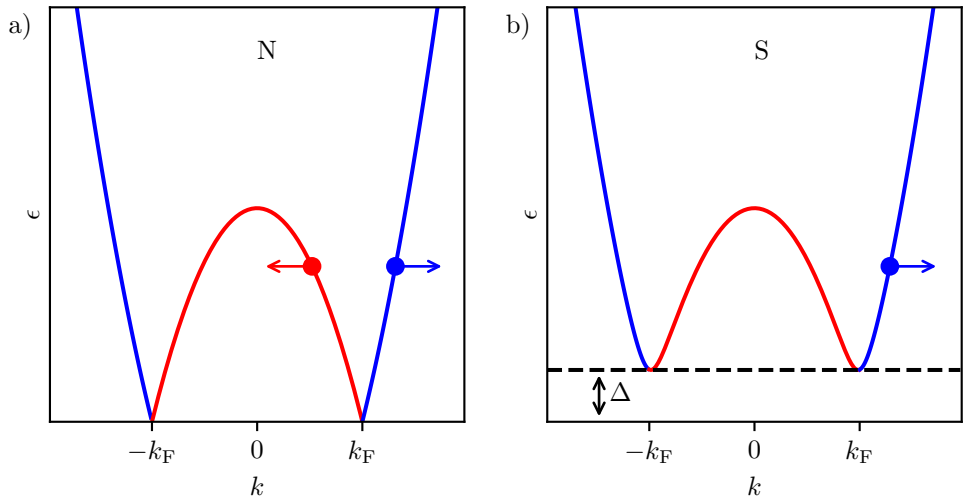

Figure 2.4.: Dispersion relation of a normal conductor (N) in panel a) and a superconductor (S) in b). The blue sections of the dispersion relation represents electrons in a) and electron-like quasiparticles in b). The red sections represents holes in a) and hole-like quasiparticles in b). The blue arrow in a) marks the incident electron which is either Andreev reflected as a hole (red arrow in a)) or transmitted into an electron-like quasiparticle state (blue arrow in b)). The dashed line marks the superconducting gap Δ in panel b).

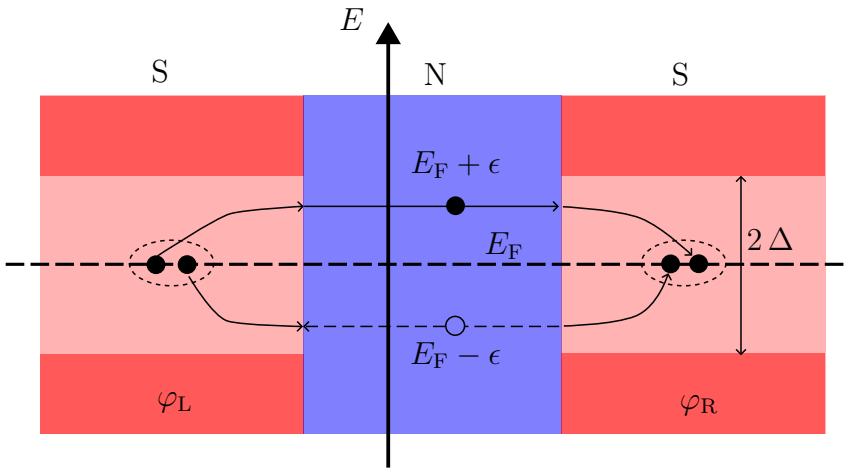

Figure 2.5.: Schematic sketch of a superconductor - normal conductor - superconductor (SNS) junction. Both superconductors have the same gap energy 2Δ. The phase difference between the superconductors is $\varphi = \varphi_L - \varphi_R$. The principle of the subgap Josephson current is illustrated: a Cooper pair from the left superconductor is transported through the normal conductor to the right superconductor via Andreev reflections.

perconducting condensate. Therefore, the quasiparticle current is independent of the superconducting phases. The second contribution $I_{\mathrm{AR}}(V)\cos(\varphi)$ is a quasiparticle current interacting with the superconducting condensate via Andreev reflections. Due to this interaction, the contribution depends on the cosine of the phase between the superconductors $\varphi = \varphi_{\mathrm{L}} - \varphi_{\mathrm{R}}$. Both the first and the second contribution require an applied voltage bias. The voltage bias between the superconductors results in a time-dependent phase difference

$$\dot{\varphi} = \frac{2e}{\hbar} V. \tag{2.16}$$

Consequently, the contributions of I_{AR} and I_{Jos} oscillate with frequency $\frac{2e}{\hbar}V$. High GHz frequencies are already obtained if the applied voltage is in the microvolt range. As a result, both contributions are averaged out and the time-averaged current I is not a function of the phase difference. The third predicted contribution is only driven by the phase difference between the superconductors. The origin of this current is a supercurrent of Cooper pairs which are sensitive to phase differences. All of Josephson's proposed transposed phenomena have been verified in experiments [69].

Figure 2.5 illustrates the supercurrent that is the origin of the Josephson current I_{Jos}. Here, Cooper pairs are transported from the left superconductor to the right superconductor via a normal conducting layer in between. When a hole is Andreev reflected at the left superconductor, a Cooper pair is split and an electron propagates towards the left superconductor in the normal conductor. At the interface to the right superconductor, the electron is Andreev reflected and forms a Cooper pair here. The probability for both Andreev reflections can be controlled via the superconducting phases but the strength of the supercurrent is only determined by the phase difference of the superconducting phases.

Similar transport phenomena as proposed by Josephson for SNS junctions occur in hybrid systems where the normal conductor is substituted by a single-level quantum dot [70, 71]. The coupling strength Γ between superconductors and quantum dot determines the possible tunnel processes and the transport properties of the device. In the following, we discuss the weak, intermediate and strong coupling regime. We consider a single-level quantum dot coupled to two identical superconductors with a superconducting gap of $2\,\Delta$. The tunnel processes in the different coupling regimes are illustrated in Fig. 2.6. The energy level of the quantum dot is aligned with the Fermi energy of the superconductors. In the case of weak coupling, see panel a), only tunneling processes of single particles are allowed. Since there are no single-particle states in the superconducting gap, particle transport is not possible for zero or small voltage bias. Only if the voltage bias between the superconductors exceed $2\,\Delta/\mathrm{e}$ occupied quasiparticle states in the source superconductor are aligned with the free quasiparticle states in the drain superconductor. In a first-order tunneling process, a quasiparticle can tunnel onto the quantum dot and afterwards in another first-order tunneling process into the drain superconductor.

In an intermediate coupling regime, see panel b), cotunneling of particles plays an important role. Besides the single-quasiparticle tunneling introduced above, it possible that a Josephson current flows through the quantum dot depending on the phase difference and the level position of the quantum dot. To give one example of a tunneling process, we consider a doubly occupied quantum dot and a Cooper pair in the left

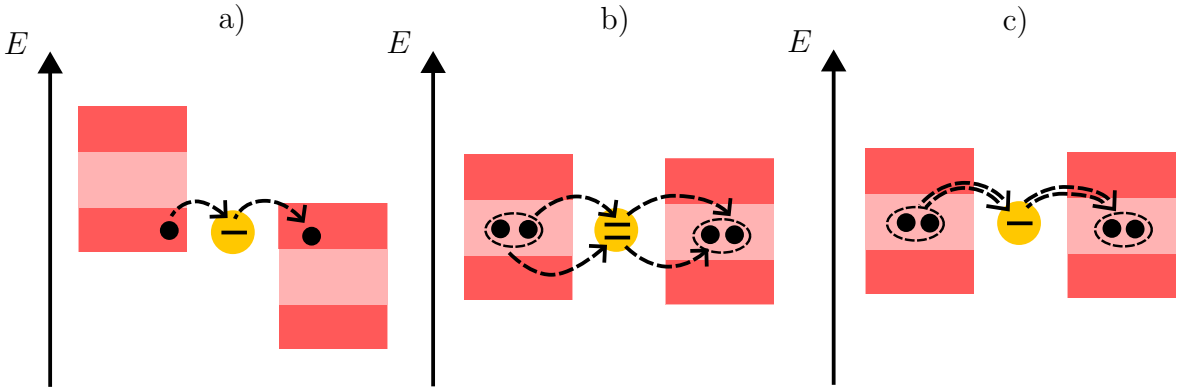

Figure 2.6.: Illustration of the dominant tunneling processes in the a) weak coupling, b) intermediate coupling and c) strong coupling regime. a) In the weak coupling regime, there is only first-order sequential tunneling possible. Thus, there is no tunneling possible when the energy level of the quantum dot is aligned with the Fermi energy of both superconductors. Only if a voltage is applied that aligns the filled quasiparticle states with the empty quasiparticle states of the superconductors over the quantum dot sequential tunneling of single particles is possible as illustrated. b) In the intermediate coupling regime, a supercurrent of Cooper pairs across the quantum dot is possible due to second-order cotunneling. Hereby, a Cooper pair tunnels first onto the quantum dot via an intermediate virtual state (not shown). Afterwards, the two electrons form a Cooper pair in the other superconductor via another virtual tunnel state. c) In the strong coupling limit, Cooper pairs can tunnel resonantly through the quantum dot allowing for arbitrary high orders of tunnel processes.

superconductor. One electron from quantum dot tunnels into the right superconductor and one electron from the left superconductor tunnels into the quantum dot. Since neither the electron from the quantum dot can enter the energy gap nor the remaining electron in left superconductor can stay in the gap, a virtual tunnel state is created where both of these electrons are shifted to quasiparticle states. To reach the final state of this cotunneling event the electron from the left superconductor tunnels onto the quantum dot and one electron tunnels coherently into the right superconductor where it forms with the first electron a Cooper pair. This is only one possibility for cotunneling of Cooper pairs. For more examples and details, see Ref. [71].

By increasing the coupling strength further, we reach the strong coupling regime. Here, the coupling strength is much larger than the Coulomb blockade. Therefore, it is equally probable that the quantum dot is empty, single or double occupied. Consequently, resonant tunneling of particles even Cooper pairs is possible, see panel c). Cooper pairs can tunnel from the source superconductor directly to the quantum dot. From there the Cooper pair can continue to the drain superconductor. The resulting supercurrent has the same properties as proposed by Josephson so the phase difference between the superconductors can be used as a driving force for the current.

In this thesis, we additionally couple a normal conducting lead to the quantum dot. The normal conductor introduces a dissipative type of dynamics into the system. Electrons in the normal conductor interact with the superconducting condensate via Andreev reflections. Due to this interaction, an Andreev current flows between the superconductors and the normal conductor through the quantum dot. Furthermore,

the normal conductor gives the opportunity to control the occupation of the quantum dot. By tuning the chemical potential of the normal conductor far below the energy level of the quantum dot, it is empty with a probability close to one. Increasing the chemical potential far above the dot's energy level will lead to a doubly occupied dot. Using this, it is possible to prepare the quantum dot in the desired initial state which is needed to study the specific transport effect.

Such three-terminal devices has been used to study the proximity effect induced on quantum dots [72–74]. The proximity effect gives the quantum dot characteristics that are related to superconductivity such as an Andreev bound state spectrum [75–77]. Recently, the proximity-induced pair amplitude has been studied in weakly superconductor quantum dot hybrids [78]. Here, the dot's pair amplitude exhibit an oscillatory dynamics which is analogue to the Higgs mode known from bulk superconductors. The transient dynamics has also been extensively studied in systems with noninteracting or weakly correlated systems [79, 80]. In these works, the pair-amplitude dynamics has been interpreted in the framework of Rabi oscillations within the two-level system consisting of empty and doubly occupied quantum dot. Besides studying the pair-amplitude dynamics such three-terminal devices provide also a playground for other transport phenomena. Similar setups act as Cooper pair splitters which are a source of spin-entangled electrons [11]. The nonlocality of Cooper-pair splitting is a promising quantum effect which might be used for quantum computing. In this thesis, we focus on a three-terminal system consisting of two superconductors and a normal conductor coupled to a strongly interacting quantum dot. The exact system and its modeling is introduced in Chapter 3.

2.4. Transport and relaxation of hot electrons in Fe/Au heterostructures

In the late 80s, researchers studied the magnetic properties of layered materials. Special interest has been given to the stacking of ferromagnetic and antiferromagnetic films after theoretical studies proposed a broad spectrum of magnetic phases [81]. Promising candidates for high quality samples are Fe, Au and Cr due to negligible lattice mismatch of these materials. In addition, the continuous development of molecular beam epitaxy opens the door to produce single crystalline multilayer samples with these materials [82–84]. In 1986, Grünberg et al. published their experiment on Fe-Cr-Fe multilayer sample which shows the existence of antiferromagnetic interlayer exchange coupling [85]. Due to this coupling the spin orientation in the Fe layers are antiparallel to each other. Further studies on this system reveal the giant magnetoresistance [86] which was awarded by a Nobel prize in 2007 [87]. Due to the giant magnetoresistance, the electric resistance in system with antiferromagnetic coupling is stronger than in systems with ferromagnetic coupling. Grünberg et al. explain this phenomena in terms of spin-flip scattering of the conduction electrons.

The giant magnetoresistance is only one aspect in the research field of spintronics. Other phenomena that have been studied extensively in Fe/Au heterostructures and other layered systems are electron channeling [88] where minority and majority electrons have different reflection and transmission probabilities at the interface according to their spin. Additionally, the generation of ultrafast spin current pulses due to the

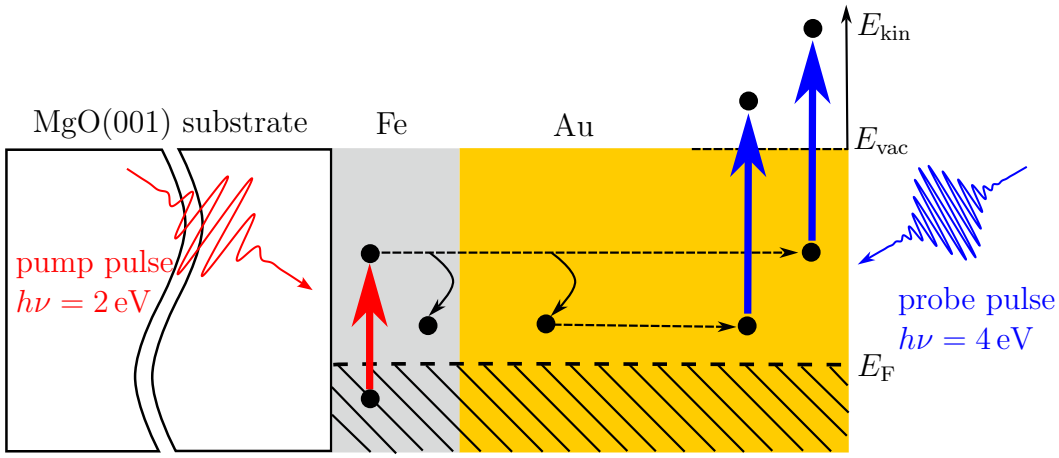

Figure 2.7.: Schematic sketch of the time-resolved two-photon photoelectron emission spectroscopy on Au/Fe/MgO(001). The pump pulse with a photon energy of $h\nu = 2\,\mathrm{eV}$ excites electrons in Fe at the back of the sample. The electrons scatter during propagation through Au and are photoemitted at the Au surface by $2h\nu = 4\,\mathrm{eV}$ photons from the probe laser. The electron energy is determined by a spectrometer (not shown). The black dots represent the excited electrons and the arrows possible relaxation and transport processes. *Adapted from Ref. [9] under Creative Common Attribution 4.0 International license.*

thermal and nonthermal spin-dependent Seebeck effect has been studied [89]. The spin-dependent Seebeck effect explains the generation of spin currents due to a temperature gradient over a bulk ferromagnet [90] or an interface to a normal metal [91]. Another spintronic phenomenon which has been studied in layered materials is the ultrafast demagnetization due to spin-dependent electron-electron scattering after an excitation by a laser pulse [92, 93]. Spin currents have been also investigated theoretically. Here, the Fe/Au heterostructure is often considered as model system [94–96].

Experimental access to such ultrafast phenomena is gained by time-resolved pump-probe experiments. Pump-probe experiments are established to study e.g. the electronic heating [97], electron-phonon relaxation [98] or the electron lifetimes [99]. The first pump-probe experiments in gold have studied the nonequilibrium electron-heating dynamics in gold [100]. Recently, theoretical approaches tackle the effect of the iron layer on spin transport [101, 102]. In the last decade, the transport dynamics in Fe/Au structures [8, 9, 89, 103–106] as well as in other material systems [93, 107] have been extensively studied.

Next, we present the experimental results that are modeled in Chapter 4. We begin with an introduction of the sample that has been analyzed by time-resolved pump-probe measurements. Afterwards, we discuss the results of these measurements, see Refs. [8, 105, 106]. Finally, we discuss the experimental results of our publication [9] which shows thickness-dependent transport features.

The sample consists of an MgO(001) substrate on which a layer of Fe and a layer of Au is grown epitaxially, see Fig. 2.7 for illustration. For the sample, two major measurements have been used. First, a front-pump front-probe measurement where the sample is pumped and probed on the Au side is used to study the local relaxation dynamics. The second measurement type is the back-pump front-probe measurement where the Fe side is pumped and the Au side is probed. Since the MgO(001) substrate

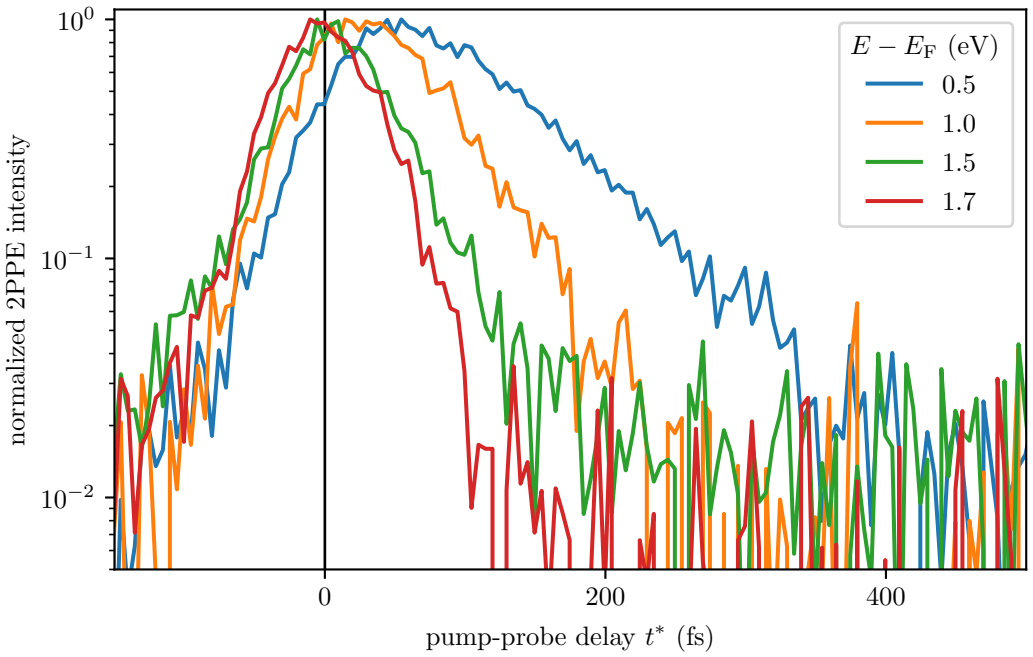

Figure 2.8.: Normalized 2PPE intensity as a function of time for the depicted energies. The data is taken in a back-pump front-probe scenario at a sample with a 7 nm Fe layer and 25 nm Au layer. Time zero denotes the time when the maximum intensity of the 2.2 eV signal is detected. *Thanks to Florian Kühne for providing and explaining the data.*

is transparent to the pump laser pulse, the pump pulse excites the electron in the Fe layer from below the Fermi edge to an energy above the Fermi edge. The delayed probe pulse excites the electrons further such that they are emitted out of the sample. With a time-of-flight measurement the kinetic energy and therefore the electron energy before the probe pulse is determined. Due to the spatial separation of the pump and probe laser pulse the electron distribution contains information about the relaxation and the propagation [108]. For the same reason, it is not possible to determine the exact passage time of the electrons since time zero is determined by the overlap of the pump and probe pulses. Therefore, all times are taken relative to the arrival time of the highest-energy electrons at $E - E_F = 2.2\,\text{eV}$. The 2PPE signal decays as a function of delay time (t^*), see Fig. 2.8. The 2PPE signal increases in intensity in the beginning and decays exponentially after reaching the maximum intensity. The higher the energy, the faster the maximum is reached and the faster the signal decays. The lower the electron energy the later the maximum of the 2PPE signal occurs. This is due to transport effects and on the other hand due to the faster relaxation of the high energy electrons.

In our collaborative publication [9], the 2PPE signal as a function of energy and time has been analyzed, see Fig. 2.9. Two features appear in the signal. At 1.7 eV there is a spectral signature occurring at $t^* = 0$. The physical origin of this feature is an interface state that allows for injection of the excited electrons from the Fe side into Au at this energy. The high energy feature decays as function of time due to scattering with electrons from below the Fermi edge. The feature is stronger with thin Au thicknesses since it becomes more likely that the electrons scatter with increasing

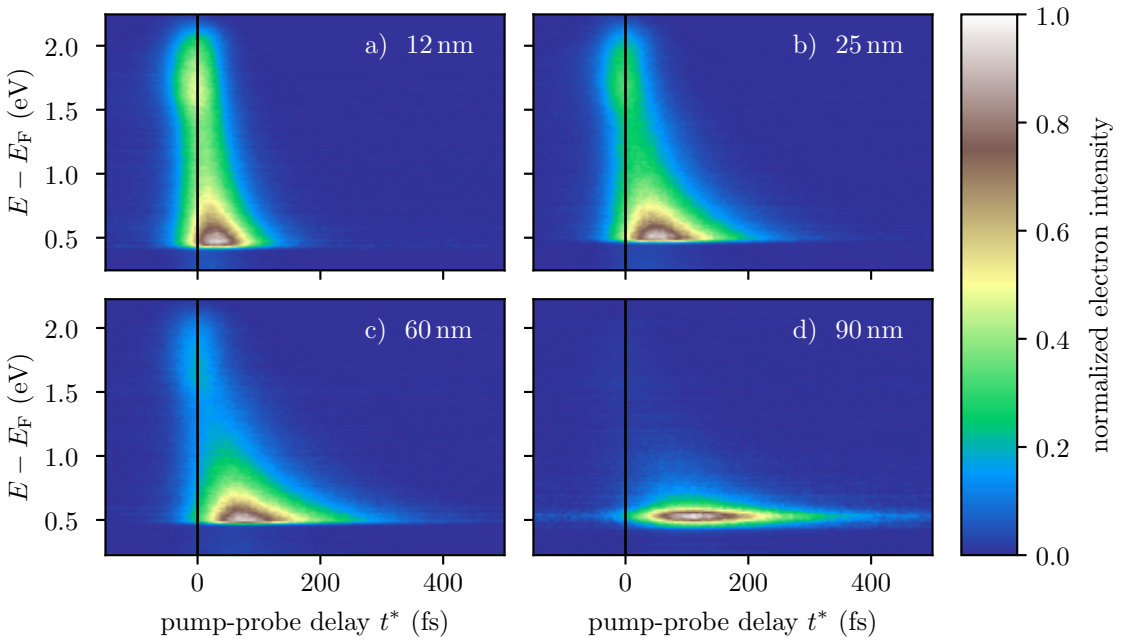

Figure 2.9.: Time-dependent 2PPE intensity as a function of energy with respect to E_F for different Au layer thicknesses, as indicated. The Fe layer thickness is kept constant at 7 nm. The data has been taken in the backside-pumping geometry. *Adapted from Ref. [9] under Creative Common Attribution 4.0 International license. Thanks to Florian Kühne for providing and explaining the data.*

Au thickness. Hence, the number of electrons that reach the Au surface with their original injection energy decreases and consequently also the 2PPE signal.

The second spectral signature is at $E - E_F = 0.6\,\text{eV}$. This feature occurs systematically at a later time t^* the larger d_{Au} is. Electrons contributing to this feature have scattered at least one time because they are not injected at this energy. Therefore, the intensity rather increases with increasing Au thickness because scattering events become more likely. At very large thicknesses, the feature decreases again in intensity because the electrons exchange too much energy to be measured in the configuration. The observed increasing delay in the low energy feature is a result of the scattering. Since the electrons scatter after a distance which is on average the mean free path, the electrons need to take a path which is longer than the Au thickness. Thus, the electrons which are measured at the low energy feature need on average a longer time to cross the sample.

A plot of the time delay as a function of Au thickness reveals that the time delay t^* increases sublinearly with the gold layer thickness (d_{Au}) in the investigated range from 5 to 105 nm, see Fig. 2.10. As a consequence, the effective velocity v_{eff} which is the ratio of d_{Au} and t^* increases approximately linearly with d_{Au}. This behavior can be understood by a simple model. Assuming an isotropic injection and scattering in Au [9] which is a reasonable assumption as transport in Au is dominated by *sp* states in the relevant energy range, the electrons have an equal probability to propagate along the mean free path in all directions. Assuming that the electrons propagate always with Fermi velocity $v_F = \lambda/\tau$, the mean free path λ can be connected to the electron lifetime τ. Since the electrons are injected at 1.7 eV, they must undergo at least one

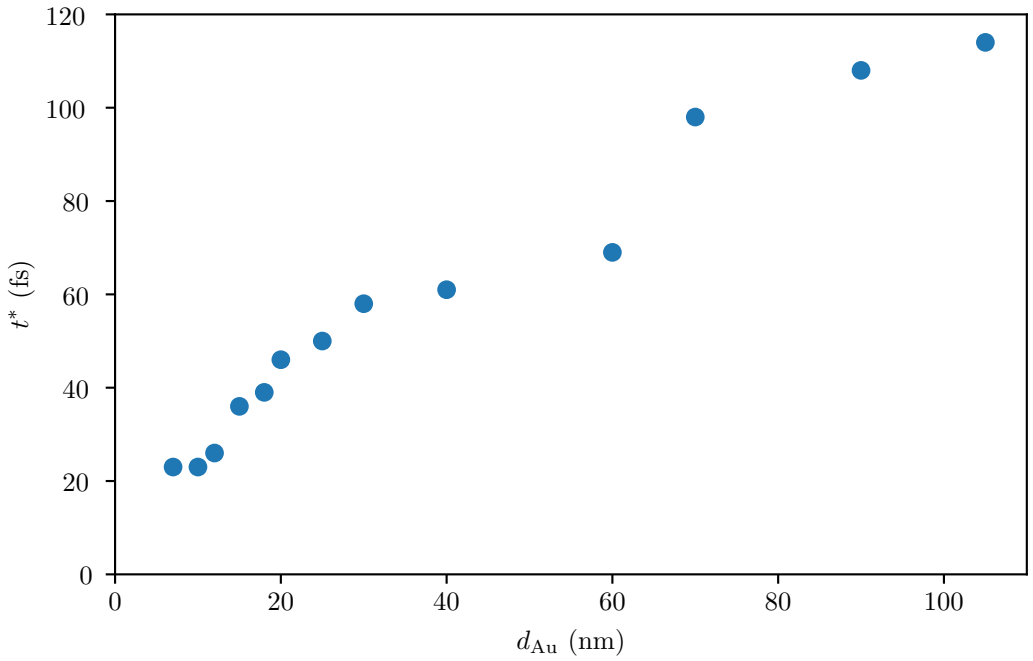

Figure 2.10.: Time delay t^* between maximum at 0.6 eV and 2.2 eV as a function of gold layer thickness d_{Au}. *Thanks to Florian Kühne for providing and explaining the data.*

inelastic scattering event which requires on average the time τ. Hence, electrons need to propagate over a distance λ, to reach an energy of 0.6 eV. The distance can be connected to the gold layer thickness by

$$d_{\mathrm{Au}} = \lambda \cos\theta_{\mathrm{min}}, \tag{2.17}$$

with θ_{min} as the minimum angle to ensure one inelastic collision. The polar angle θ is defined as the angle between the surface normal and the propagation direction. With the definition of the effective velocity, the electron lifetime can be connected to the mean free path by

$$v_{\mathrm{eff}} = \frac{d_{\mathrm{Au}}}{t^*} = \frac{d_{\mathrm{Au}}}{t_1 - t_0} = v_{\mathrm{F}} \frac{d_{\mathrm{Au}}}{\lambda - d_{\mathrm{Au}}}, \tag{2.18}$$

where we assume that time t_0 is set by ballistic electrons propagating with $\theta = 0$ through the sample. The time t_1 is the time electrons with 0.6 eV need to reach the sample surface. A series expansion for small gold layer thicknesses, $d_{\mathrm{Au}} \ll \lambda$, gives the observed linear dependence of v_{eff},

$$v_{\mathrm{eff}} \approx v_{\mathrm{F}} \frac{d_{\mathrm{Au}}}{\lambda} = \frac{d_{\mathrm{Au}}}{\tau}. \tag{2.19}$$

A linear fit of v_{eff} of the experimental data from Ref. [9] yields an electron lifetime which is in good agreement with literature data for inelastic hot electron lifetimes obtained with time-resolved two-photon photoelectron emission spectroscopy [99].

It is unlikely that the electrons experience only a single scattering event for all $\theta(d_{\mathrm{Au}})$. Therefore, an extended theoretical modeling is needed at this point to conclude on the

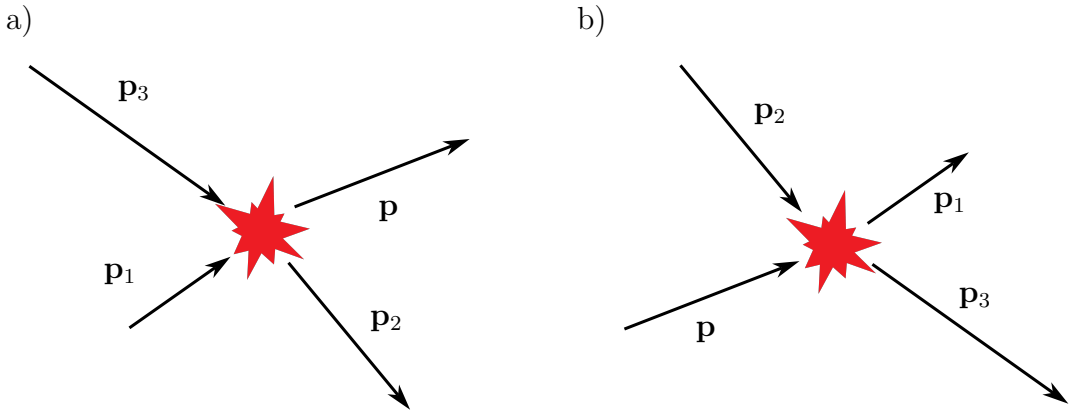

Figure 2.11.: Illustration of a two-particle interaction where momentum is transferred. Two cases are considered. a) shows the process where momentum $\mathbf{p}$ is gained. In b), momentum $\mathbf{p}$ is lost via a collision with a second particle.

transport processes responsible for the features in the experimental data. In the next part, we introduce theoretical concepts to model transport and relaxation processes. Our own theoretical models and results are discussed in Chapter 4.

2.5. Theoretical modeling of relaxation and transport dynamics

Besides the experimental insights into the relaxation and transport dynamics, multiple theoretical descriptions of the underlying physics have been established. In this part of the thesis, we will introduce the Boltzmann equation which serves as a model to calculate the relaxation dynamics of many-body distributions. We focus on the local energy relaxation at first. We show also analytic approaches to solve the energy relaxation. We close this section with a discussion about the transport regimes and their characteristics.

2.5.1. Boltzmann Equation

A well established approximation for the irreversible relaxation of a nonequilibrium distribution into equilibrium is the Boltzmann equation [109]. Boltzmann assumed that the many-body distribution function of N particles can be written as N times the single-particle distribution function if correlations between the particles are neglected. To avoid the problem that a noninteracting gas cannot reach an equilibrium, Boltzmann introduced a collision term

$$\frac{\partial f}{\partial t} = \Gamma_{\text{gain}} - \Gamma_{\text{loss}}. \tag{2.20}$$

The processes behind the gain and loss rates Γ_{gain} and Γ_{loss} are illustrated in Fig 2.11 a) and b), respectively. To gain particles with momentum $\mathbf{p}$, two particles with momentum $\mathbf{p}_3$ and $\mathbf{p}_1$ collide, exchange momentum and have the momenta $\mathbf{p}$ and $\mathbf{p}_2$ afterwards. If the scattering process is turned around, particles with momentum $\mathbf{p}$ and $\mathbf{p}_2$ scatter and have the momenta $\mathbf{p}_1$ and $\mathbf{p}_3$ after the collision. Hence, the distribution

looses particles with momentum $\mathbf{p}$, cf. Fig. 2.11 b). If higher order scattering processes are neglected, the Boltzmann collision term is given by

$$\frac{\partial f}{\partial t} = \int d^3p_1 \int d^3p_2 \int d^3p_3 W(\mathbf{p}, \mathbf{p}_2; \mathbf{p}_1, \mathbf{p}_3) \\ [f(\mathbf{r}, \mathbf{p}_1, t) f(\mathbf{r}, \mathbf{p}_3, t) - f(\mathbf{r}, \mathbf{p}, t) f(\mathbf{r}, \mathbf{p}_2, t)]. \tag{2.21}$$

Here, the transition probability $W(\mathbf{p}, \mathbf{p}_2; \mathbf{p}_1, \mathbf{p}_3)$ is given by

$$W(\mathbf{p}, \mathbf{p}_2; \mathbf{p}_1, \mathbf{p}_3) = \frac{|\mathbf{p} - \mathbf{p}_2|}{m} \sigma(\mathbf{p}, \mathbf{p}_2; \mathbf{p}_1, \mathbf{p}_3) \delta(\mathbf{p} + \mathbf{p}_2 - \mathbf{p}_1 - \mathbf{p}_3) \\ \delta(E_{\text{kin}} + E_{\text{kin},2} - E_{\text{kin},1} - E_{\text{kin},3}), \tag{2.22}$$

with scattering cross section $\sigma(\mathbf{p}, \mathbf{p}_2; \mathbf{p}_1, \mathbf{p}_3)$ and particle mass m. The delta functions ensure momentum and energy conservation, respectively. When the Boltzmann equation is used to describe the relaxation of electrons, the Pauli exclusion principle needs to be taken into account. Hence, the electrons can only scatter into free states. Thus, the collision term is given by

$$\frac{\partial f}{\partial t} = \int d^3p_1 \int d^3p_2 \int d^3p_3 W(\mathbf{p}, \mathbf{p}_2; \mathbf{p}_1, \mathbf{p}_3) \mathcal{F}, \tag{2.23}$$

with

$$\begin{aligned} \mathcal{F} =& f(\mathbf{r}, \mathbf{p}_1, t) f(\mathbf{r}, \mathbf{p}_3, t)(1 - f(\mathbf{r}, \mathbf{p}, t))(1 - f(\mathbf{r}, \mathbf{p}_2, t)) \\ & - f(\mathbf{r}, \mathbf{p}, t) f(\mathbf{r}, \mathbf{p}_2, t)(1 - f(\mathbf{r}, \mathbf{p}_1, t))(1 - f(\mathbf{r}, \mathbf{p}_3, t)). \end{aligned} \tag{2.24}$$

Here, the Fermi function f describes the occupied states and $1 - f$ gives the free states the electrons can scatter in. The first term corresponds to the scattering process in panel a) of Fig. 2.11. The second term is the mathematical expression for the process in panel b), accordingly.

The population dynamics of bosons and fermions have been described with the Boltzmann equation [110, 111]. The Boltzmann equation is also used to describe the evolution of hot electrons after the electronic system has been excited by an initial ultrashort laser pulse [112, 113]. In these papers, the authors perform a (particle-in-cell) simulation to tackle also the material specific density of states that has a strong influence on the transmission probability W. Besides the mentioned numeric approaches, there is also an analytic approach [12] which is explained in detail in the next part.

2.5.2. Analytic solution of the Boltzmann collision term

Before following the argumentation of Ref. [12], we simplify the Boltzmann equation (2.23) by assuming isotropic scattering. In addition, we reduce the number of independent integrals by using the momentum conservation explicitly

$$\Delta\mathbf{p} = \mathbf{p}_1 - \mathbf{p} = \mathbf{p}_2 - \mathbf{p}_3. \tag{2.25}$$

Assuming isotropic scattering, the distributions f_i are only a function of the absolute value of the momentum p. Hence, the angles can be integrated out [110, 111]. Using the proportionality between the momentum p and the wave vector k, it is possible to

substitute the integrals over momentum space by an integration over energy [112]. The resulting Boltzmann equation describes the redistribution of the energy in the electron system due to electron-electron scattering

$$\dot{f}_\xi = \int d\xi' \int d\epsilon \int d\epsilon' K(\xi,\xi',\epsilon,\epsilon')\delta(\xi+\epsilon-\xi'-\epsilon') \\ [f_{\xi'}f_{\epsilon'}(1-f_\xi)(1-f_\epsilon) - f_\xi f_\epsilon(1-f_{\xi'})(1-f_{\epsilon'})]. \tag{2.26}$$

In Ref. [12], the kernel $K(\xi,\xi',\epsilon,\epsilon')$ is a function of the density of states and the electron-electron scattering matrix element. The energies are given with respect to the Fermi energy. Following the argumentation in Ref. [12], only the relaxation of nonequilibrium electron-hole pairs with energies much smaller than the equilibrium Fermi energy E_F is considered. In this case, the kernel $K(\xi,\xi',\epsilon,\epsilon')$ has only small variations on the scale of the Fermi energy and one can approximate the kernel by a constant K. Assuming that the laser excites only a small number of electrons from the Fermi sea, one can linearize Eq. 2.26 by introducing a small nonequilibrium correction $\phi(\xi,t) \ll 1$ to the equilibrium distribution $n_\xi = (\exp[\xi/k_\mathrm{B}T]+1)^{-1}$

$$f_\xi = n_\xi + \phi(\xi,t). \tag{2.27}$$

If only terms up to linear order in ϕ are considered, one obtains

$$\dot{\phi}(\xi,t) = K(k_\mathrm{B}T)^2 \int d\xi' \int d\epsilon \int d\epsilon' \delta(\xi+\epsilon-\xi'-\epsilon') \\ [-\phi(\xi,t)(n_\epsilon n_{-\xi'} n_{-\epsilon'} + n_{\xi'} n_{\epsilon'} n_{-\epsilon}) + \phi(\xi',t)(n_{\epsilon'} n_{-\xi} n_{-\epsilon} + n_\xi n_\epsilon n_{-\epsilon'}) \\ - \phi(\epsilon,t)(n_{\xi'} n_{\epsilon'} n_{-\xi} + n_\xi n_{-\xi'} n_{-\epsilon'}) + \phi(\epsilon',t)(n_{\xi'} n_{-\xi'} n_{-\epsilon} + n_\xi n_\epsilon n_{-\xi'})]. \tag{2.28}$$

We would like to remark that the corresponding equation in Ref. [12] omits terms in the bracket. The energies are given in units of $k_\mathrm{B}T$ and the identity $n_{-x} = 1 - n_x$ is used. Terms which are independent from ϕ yield exactly zero after the integration. The other four terms can be simplified by integrating them separately. For the first term which depends on $\phi(\xi,t)$ all integrals can be solved analytically. For the other three terms, there are always two integrals that can be solved analytically and one remaining integral. The remaining integral is always an integration over the energy on which ϕ depends, respectively. The remaining sum can be simplified by a transformation of variables which finally gives

$$\dot{\phi}(\xi,t) = -\frac{1}{\tau(\xi)}\phi(\xi,t) + \frac{K(k_\mathrm{B}T)^2}{\cosh(\xi/2)} \\ \int_{-\infty}^{\infty} d\xi' \phi(\xi',t)\cosh(\xi'/2)\left[\frac{\xi-\xi'}{\sinh((\xi-\xi')/2)} - \frac{\xi+\xi'}{2\sinh((\xi+\xi')/2)}\right], \tag{2.29}$$

for arbitrary initial perturbations $\phi(\xi,0)$. The first term on the right side of Eq. (2.29) describes the relaxation of the hot electron into equilibrium with an energy-dependent relaxation time

$$\tau(\xi) = \frac{\tau_0}{1+\frac{\xi^2}{\pi^2}}, \tag{2.30}$$

with $\tau_0 = 2/(\pi^2 K(k_\mathrm{B}T)^2)$. The energy-dependent lifetime is in agreement with the lifetime of electron-hole excitations from Fermi-liquid theory. The second term describes

the energy redistribution due to electron-electron scattering. At all times t, the energy and the number of particles is conserved. Assuming that the initial perturbation is antisymmetric in energy, the equation can be simplified further. If the system is, e.g., excited by a laser, electrons are excited symmetrically from below the Fermi energy to an excited state by forming electron-hole pairs. In this case, the Boltzmann equation can be simplified using the identity $\chi(\xi,t) = \phi(\xi,t)\cosh(\xi/2)$

$$\frac{\dot{\chi}(\xi,t)}{K(k_\mathrm{B}T)^2} = -\frac{\pi^2+\xi^2}{2}\chi(\xi,t) + \frac{3}{2}\int_{-\infty}^{\infty} d\xi'\chi(\xi',t)\frac{\xi-\xi'}{\sinh((\xi-\xi')/2)}. \tag{2.31}$$

Both Eq. (2.29) and Eq. (2.31) can be solved numerically with a given initial perturbation. So far, the solution to the collision term provides only a description of the relaxation process but not of the transport processes. In Chapter 4, we discuss the energy relaxation as a function of time for different initial distribution functions first. Afterwards, we introduce a diffusive transport extension to apply the Boltzmann equation to the Fe/Au heterostructure discussed above assuming that there is only diffusive transport possible in the sample.

2.5.3. Transport regimes in metallic structures

The simulations in Ref. [113] are based on the Boltzmann transport equation and, therefore, already include the transport of particles in their algorithms. In addition, they use material-specific scattering probabilities by taking the density of states of the corresponding materials into account. The particle-in-cell approach has been applied to find classic equation of motions for so-called superparticles that represents the full hot-carrier distribution in a statistical fashion. The Fe/Au heterostructure serves in Ref. [113] as a model system. This method is capable to describe the local relaxation process as a function of time and, hence, this model agrees with the discussed energy redistribution in Fig. 2.9. The transport regime changes from ballistic to diffusive with increasing time the hot electrons spend in the sample. The transition does not change rapidly which indicates that there is an intermediate transport regime which is called superdiffusive.

For a better understanding, we introduce the transport regimes microscopically. For diffusion, we consider a stochastic process like the Brownian motion [109]. During a Brownian motion apparently random forces act on the observed particles. Averaging over time, the total force is zero. However, there is a nonzero mean square displacement in one dimension given by

$$\left\langle x^2(t)\right\rangle = 2Dt, \tag{2.32}$$

with diffusion constant D. This equation is used to define the diffusion coefficient which is the exponent of t. A diffusion coefficient of one is a clear sign of diffusive transport. On contrast, ballistic transport is the undisturbed uniform motion of a particle. Thus, the particle does not scatter with any other (quasi)particles. Such a transport would be indicated by a diffusion coefficient of two.

Scattering occurs on average after propagating the mean free path λ which is connected to the electron lifetime τ by the Fermi velocity of electrons. If the observed transport is on a scale much smaller than the mean free path it is unlikely that the electrons have already scattered. Hence, the solution of Ref. [113] that the ballistic

transport regime is visible for short times is reasonable. On the other side, if the observation occurs over longer time such that the electrons propagate over distances which are much larger than the mean free path multiple scattering events dominate the trajectory of the electrons. Therefore, the transport is also on the diffusive side in line with the model of Ref. [113].

The transition via the superdiffusive transport regime occurs when the path length of the electrons is in the magnitude of the mean free path. Then, the electrons cross the sample with a limited number of scattering events. Thus, the transport is neither ballistic nor diffusive. The only sign of the transition is an anomalous generalized diffusion coefficient between one and two. It is important to note that the timescale of the observation has a strong influence on the transport regime as stated by Ref. [113]. So far, the discussion of the transport regime has been applied to the whole ensemble of electrons. It is possible that all transport regimes coexist in one ensemble of electrons e.g. at different energies. Additional research is required at this point.

Apart from the Boltzmann transport equation, there are also other models that investigate the transport regimes of excited electrons in similar systems [93, 114]. Here, the flux of an electron density based on the trajectory of the particles is derived. Subsequentially, higher generations of electrons to include the electron cascade into the density are considered. The result is in line with Ref. [113] regarding the transition from ballistic to diffusive transport over time. However, the information on the energy is not considered as well.

Finally, we introduce a scheme to derive an equation of motion for a particle in a diffusive transport regime, cf. Ref. [109]. Diffusive transport can occur in several different systems. The underlying mechanism is the flow of (quasi)particles from a region with a high concentration to a region with a low concentration. In solids, Fick's law defines the diffusion current as

$$J = -D\frac{\partial \rho}{\partial x}, \tag{2.33}$$

with diffusion coefficient D and particle density ρ. This law is valid for systems with a constant flow of particles. If we consider a closed system, the diffusion current will decrease as a function of time due to equilibrating particle concentration. The time-dependent diffusion can be described by Fick's second law

$$\frac{\partial \rho}{\partial t} = D\frac{\partial^2 \rho}{\partial x^2}, \tag{2.34}$$

which is deduced from the first law under consideration of the continuity equation for the particle density. To solve the diffusion equation, there are multiple numeric [115, 116] and analytic [117, 118] approaches. Mathematically, the diffusion equation is equivalent to the heat equation that describes the heat flow in a system from the hot to the cold side reaching an equilibrium state. A known one-dimensional solution of the heat equation is the fundamental solution which is given by

$$\rho(x,t) = \frac{1}{\sqrt{4\pi D t}} \int_{-\infty}^{\infty} dx_0 \exp\left[-\frac{(x-x_0)^2}{4Dt}\right] \rho_0(x_0), \tag{2.35}$$

with initial distribution ρ_0 at time $t = 0$. The fundamental solution folds the initial distribution with a time-dependent Gaussian distribution. The standard deviation of

the Gaussian distribution increases with $\sqrt{t}$. Thus, the distribution spatially broadens over time. The equation of motion and the fundamental solution is used to expand the solution of the collision term of Ref. [12] by diffusive transport, see Chapter 4.7.

3. Pair-amplitude dynamics in strongly-coupled superconductor-quantum dot hybrids

In this chapter, we investigate the pair-amplitude dynamics of strongly-coupled superconductor-quantum dot hybrids. In the first part of this chapter, we present the Hamiltonian used to model the system. Due to the strong coupling between the superconductors and the quantum dot, we use the hybridized system of both as basis for the mathematical description of the transport with real-time diagrammatics. The transport is described by a master equation which we write in a pseudospin basis that visualizes the effects of the superconducting correlations induced on the quantum dot by the superconductors. The pseudospin gives in intuitive picture to understand the dynamics of the pair amplitude. The Andreev and Josephson current which are a function of the pseudospin components as we discuss in Chapter 3.4 are measurable quantities that can be used to analyze the pair-amplitude dynamics experimentally. In the results, we show first the response of the pair amplitude after quenching the system into a nonequilibrium state. Finally, we discuss the resulting dynamics if the system is periodically driven by an external force. Here, we discuss the limit of adiabatic and fast driving. The model and results have previously been published in Ref. [119].

3.1. Model

We consider a three-terminal setup consisting of a quantum dot which is symmetrically coupled to two conventional BCS superconductors. The strong coupling induces superconducting correlations on the quantum dot via the proximity effect. In addition, the quantum dot is weakly coupled to a normal conductor. With the weak coupling, only single-electron tunneling is allowed. The normal conductor serves as a dissipative channel in the system. Similar systems have been discussed in Ref. [72, 74, 120]. The system is sketched in Fig. 3.1. The total Hamiltonian

$$H = \sum_{\eta} H_{\eta} + H_{\mathrm{dot}} + H_{\mathrm{tun}}, \tag{3.1}$$

describes the setup. The first term describes the three leads $\eta \in [\mathrm{SL}, \mathrm{SR}, \mathrm{N}]$ coupled to the quantum dot. In a mean-field approximation the BCS Hamiltonian is given by

$$H_{\eta} = \sum_{\mathbf{k}\sigma} \epsilon_{\eta\mathbf{k}} a^{\dagger}_{\eta\mathbf{k}\sigma} a_{\eta\mathbf{k}\sigma} + \sum_{\mathbf{k}} \left(\Delta_{\eta} e^{i\varphi_{\eta}} a_{\eta\mathbf{k}\uparrow} a_{\eta-\mathbf{k}\downarrow} + \mathrm{H.c.} \right). \tag{3.2}$$

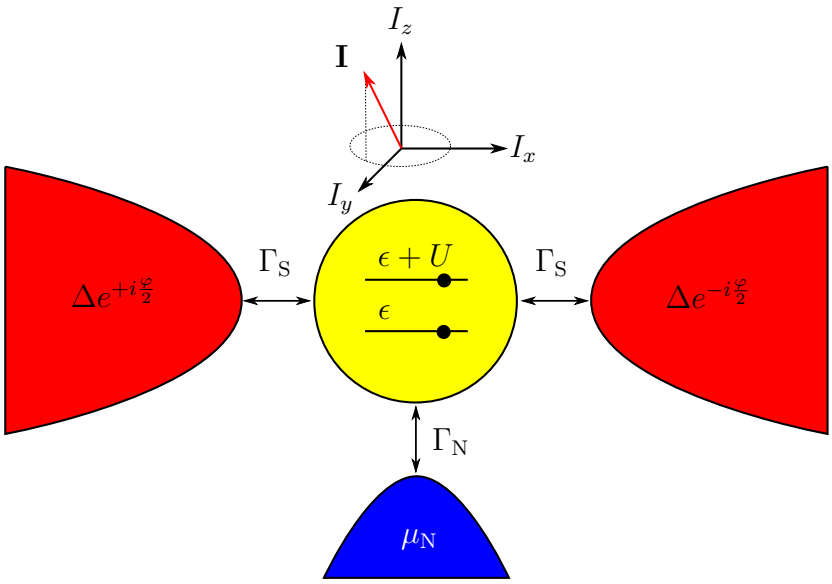

Figure 3.1.: Schematic sketch of the three-terminal system. A single-level quantum dot is strongly coupled to two grounded superconductors with superconducting phases $\pm\varphi/2$ by tunnel coupling strengths $\Gamma_{SL} = \Gamma_{SR} = \Gamma_S$. Furthermore, the quantum dot is weakly coupled to a normal conductor with electrochemical potential μ_N. The proximity effect induces superconducting correlations on the quantum dot which are characterized by the pseudospin $\mathbf{I}$. *Reprinted with permission from Ref. [119]. Copyright 2024 by the American Physical Society.*

The first term of Eq. (3.2) is the kinetic energy of the electrons in the lead η with spin σ and momentum $\mathbf{k}$. The second term is only nonzero for the superconducting leads since it describes the superconducting pairing. The absolute value of the order parameter Δ is assumed to be equal for both superconductors and zero for the normal conductor. The phases of the order parameters are symmetrically chosen $\varphi_{SL} = -\varphi_{SR} = \varphi/2$ without loss of generality. The critical temperature for both superconductors is assumed to be equal and both superconductors are grounded $\mu_S = 0$. The chemical potential μ_N of the normal conductor can be used to control the occupation of the quantum dot.

The single-level, spin-degenerate quantum dot with level position ϵ is described by the dot Hamiltonian

$$H_{\text{dot}} = \sum_{\sigma} \epsilon c_{\sigma}^{\dagger} c_{\sigma} + U c_{\uparrow}^{\dagger} c_{\uparrow} c_{\downarrow}^{\dagger} c_{\downarrow}, \tag{3.3}$$

where the second term denotes the on-site Coulomb repulsion U. The level position can be tuned by a gate voltage. The tunneling between the dot and the reservoirs is described by the Hamiltonian

$$H_{\text{tun}} = \sum_{\eta \mathbf{k} \sigma} t_{\eta} a_{\eta \mathbf{k} \sigma}^{\dagger} c_{\sigma} + \text{H.c.}, \tag{3.4}$$

with tunnel-matrix element t_η which we assume to be spin and momentum independent. The tunnel-matrix element is connected to the coupling strength via

$$\Gamma_{\eta} = 2\pi |t_{\eta}|^2 \rho_{\eta}^{N}, \tag{3.5}$$

with the density of states in the normal state ρ^{N}. Due to the symmetric coupling between quantum dot and superconductors, we have $\Gamma_{\mathrm{SL}} = \Gamma_{\mathrm{SR}} = \Gamma_{\mathrm{S}}$.

In this thesis, we analyze the dynamics of the proximity-induced superconducting pair amplitude. As it describes the dynamics of Cooper pairs which resonantly tunnel between superconductors and quantum dot, our focus lies on the subgap physics. Therefore, it is a reasonable approximation to consider our setup in the infinite-gap limit. In this limit, the superconducting gap is the largest energy scale in the whole system. Hence, we can model the coupling between quantum dot and superconductors exactly since even- and odd-parity dot states decouple and the system can be mapped onto a noninteracting one with renormalized level positions [121].

The exact resummation results in an effective Hamiltonian

$$H_{\mathrm{eff}} = H_{\mathrm{dot}} - H_{\mathrm{p}}, \tag{3.6}$$

for the hybridized system consisting of quantum dot and superconductors. The new full system Hamiltonian is given by

$$H = H_{\mathrm{eff}} + H_{\mathrm{N}} + H_{\mathrm{tun}} + H_{\mathrm{p}}, \tag{3.7}$$

where for symmetric coupling to the superconductors the pairing Hamiltonian is given by

$$H_{\mathrm{p}} = \Gamma_{\mathrm{S}} \cos\left(\frac{\varphi}{2}\right)\left(c_{\downarrow}c_{\uparrow} + c_{\uparrow}^{\dagger}c_{\downarrow}^{\dagger}\right), \tag{3.8}$$

see also Ref. [120]. Due to the infinite-gap limit, the superconducting properties are restricted to the subgap physics. Therefore, we do not need to consider quasiparticle excitations, see Eq. (3.2). We remark that the tunnel Hamiltonian, now, only accounts for the tunneling between the normal conductor and the hybrid system.

The eigenbasis of H_{eff} is given by $|\uparrow\rangle$, $|\downarrow\rangle$ which describe the single-occupied quantum dot with a spin-up or spin-down electron, respectively, and

$$|\pm\rangle = \frac{1}{\sqrt{2}}\left[\mp\sqrt{1 \mp \frac{\delta}{2\epsilon_{\mathrm{A}}}}\,|0\rangle + \sqrt{1 \pm \frac{\delta}{2\epsilon_{\mathrm{A}}}}\,|d\rangle\right]. \tag{3.9}$$

The $|\pm\rangle$ dot states describe a coherent superposition of empty- and doubly-occupied dot states $|0\rangle$, $|d\rangle$ with

$$\epsilon_{\mathrm{A}} = \sqrt{\left(\frac{\delta}{2}\right)^2 + \Gamma_{\mathrm{S}}^2 \cos^2\left(\frac{\varphi}{2}\right)}, \tag{3.10}$$

and the level detuning

$$\delta = 2\epsilon + U, \tag{3.11}$$

which characterizes deviations from the particle-hole symmetric point at $\delta = 0$. The eigenenergies are given by [74, 121]

$$E_{\sigma} = \epsilon, \tag{3.12}$$

$$E_{\pm} = \frac{\delta}{2} \pm \epsilon_{\mathrm{A}}. \tag{3.13}$$

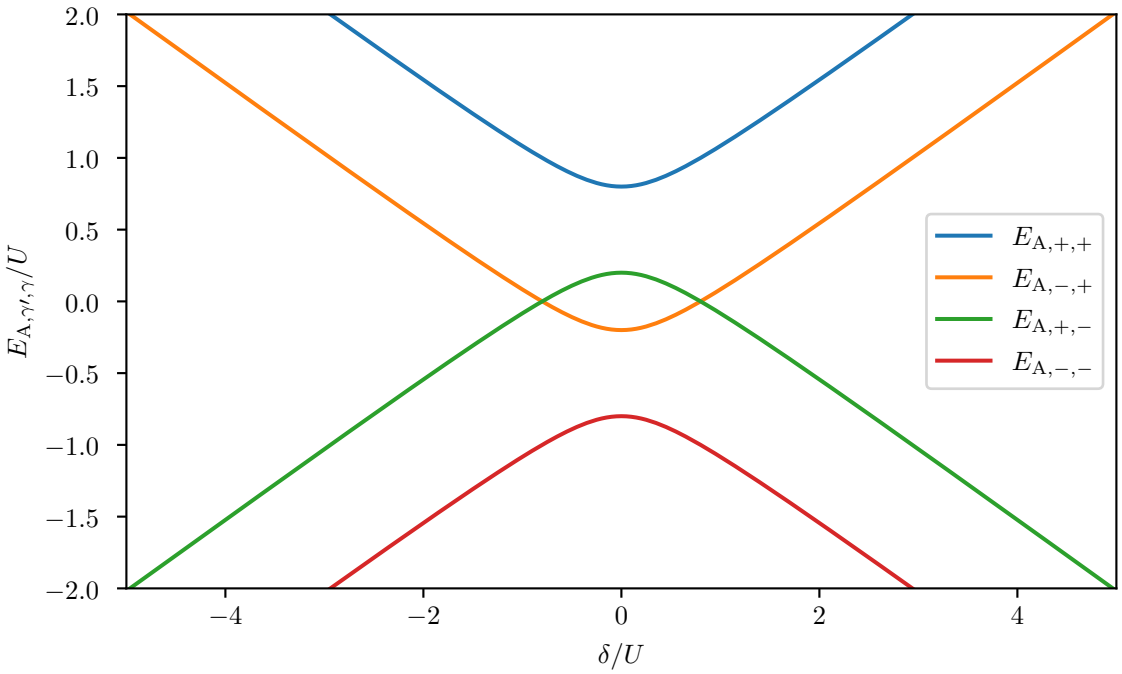

Figure 3.2.: Andreev bound state energies as a function of level detuning in units of the Coulomb potential U. The plot parameters are $\Gamma_{\mathrm{S}} = 0.3\,U$, $\Gamma_{\mathrm{N}} = 5 \times 10^{-3}\,U$, $k_{\mathrm{B}}T = 10^{-2}\,U$ and $\varphi = 0$.

The excitation energies of the quantum dot are given by the differences of the eigenenergies

$$\pm(E_{\pm} - E_{\sigma}), \tag{3.14}$$

and can be identified as the Andreev bound state energies in the infinite-gap limit

$$E_{\mathrm{A},\gamma',\gamma} = \gamma'\frac{U}{2} + \gamma\epsilon_{\mathrm{A}}, \quad \gamma', \gamma \in \{\pm 1\}. \tag{3.15}$$

The Andreev bound state energies are plotted as a function of the level detuning in Fig. 3.2. The highest excitation energies, i.e. Andreev bound state energies, are at large detunings while the smallest excitation energies are at the particle-hole symmetric point for the chosen parameters. Therefore, the superposition of the zero-occupied $|0\rangle$ and doubly occupied dot $|d\rangle$ becomes largest at the particle-hole symmetric point $\delta = 0$. For large detunings, the superposition vanishes and we find the quantum dot approximately in the empty or doubly occupied state.

So far, we have characterized our three-terminal system. In the next section, we introduce the real-time diagrammatics which is used to model the dynamics on the dot in a time-dependent fashion.

3.2. Real-time diagrammatics

The theoretical description of nonlinear, nonequilibrium quantum transport is of key importance for the understanding of phenomena in nanoscale systems. Numerous theoretical descriptions for the transport phenomena in quantum dots have been developed

[122, 123]. Each of these methods is optimized for their parameter regimes which allows for different insights into the nonequilibrium dynamics of the nanoscale structure.

Scattering matrix theory is an early analytic method to calculate transport in mesoscopic systems. Landauer describes the conductance as a transmission through a scattering center in the 50s. In the 80s, Büttiker generalized it for multiterminal systems [124–126]. Stationary as well as nonstationary quantum transport can be described by the scattering matrix theory as long as there are only weak interactions which can be treated on a mean-field level.

One example of the various numerical methods is the scattering state numerical renormalization group (NRG) which establishes an accurate solution for steady-state currents. The scattering-state NRG method is a nonequilibrium extension of the NRG method developed in the 70s. The scattering state NRG method provides a powerful tool to analyze nonequilibrium transport in quantum-dot nanostructures for arbitrary Coulomb interactions, temperatures, magnetic fields, and bias voltages. Per contra, such numerical methods are typically computational demanding [127–132].

Perturbative methods are a more efficient analytic way to study transport effects. The downside is that such analytic methods are restricted to a limited number of applicable cases. In this thesis, we use a systematic perturbation theory in the coupling strength to the normal conductor. With a diagrammatic technique, the method is able to consider in real time arbitrary interactions on the quantum dot and can describe sequential tunneling, inelastic cotunneling and resonant tunneling [133–135].

In the following, we discuss the real-time diagrammatic transport theory according to Ref. [136, 137]. Hereby, we acknowledge the dissertations [138–140] that have explained the derivation of the real-time diagrammatics. Different from the above works, we will formulate the real-time diagrammatic directly in the eigenbasis of the effective dot, see Chapter 3.1. This will lead to minor modification in the derivation below.

The expectation value of an operator A at a time t is given by

$$\langle A(t)\rangle = \mathrm{tr}[\rho_0 A(t)_H], \tag{3.16}$$

where $A(t)_H$ is the operator in the Heisenberg picture and $\rho_0 = \rho(t_0)$ is the initial density matrix of the system at initial time t_0. The system consists of a normal conducting reservoir and the effective superconductor-quantum dot hybrid system. The density matrix is assumed to factorize at time t_0 such that it can be written as

$$\rho_0 = \rho_{\mathrm{eff}}(t_0)\rho_{\mathrm{N}}(t_0). \tag{3.17}$$

The equilibrium density matrix for the reservoir can be expressed with a grand canonical ensemble

$$\rho_{\mathrm{N}}(t_0) = Z^{-1}\exp\left(-\beta(H_{\mathrm{N}} - \mu_{\mathrm{N}}N_{\mathrm{N}})\right). \tag{3.18}$$

Here and in the following, we assume the reservoir to have the inverse temperature $\beta = 1/k_{\mathrm{B}}T$, μ_{N} is the chemical potential of the normal conductor and $N_{\mathrm{N}} = \sum_{\mathbf{k}\sigma} a^\dagger_{\mathbf{k}\sigma}a_{\mathbf{k}\sigma}$ is the number operator of the electrons in the normal conducting reservoir. The normalization Z is chosen such that the density matrix fulfills $\mathrm{tr}\,[\rho_{\mathrm{N}}(t_0) = 1]$.

The effective hybrid part of the initial density matrix is not assumed to be in an equilibrium state. We assume that the initial distribution is diagonal in the basis

$|\chi\rangle \in \{|\uparrow\rangle, |\downarrow\rangle, |+\rangle, |-\rangle\}$

$$\rho_{\text{eff}}(t_0) = \sum_{\chi} P_\chi |\chi\rangle \langle\chi|, \tag{3.19}$$

with normalized probabilities P_χ. At this point, it is convenient to change to the interaction picture with

$$A(t)_I = \tilde{T} \exp\left(i \int_{t_0}^{t} dt' H_{\text{tun}}(t')_I\right) A(t)_H T \exp\left(-i \int_{t_0}^{t} dt' H_{\text{tun}}(t')_I\right), \tag{3.20}$$

where the time ordering and the anti-time ordering operator is given by T and $\tilde{T}$, respectively. Here, we write the integrals as a contour integral over the Keldysh contour. The Keldysh contour is visualized by two horizontal lines. The upper line runs forward from t_0 to t and continues on the lower line running backward from t to t_0.

The quantum statistical expectation value of an operator A in the Heisenberg picture using the Keldysh contour is given by

$$\langle A(t)\rangle = \text{tr}\left[T_K \exp\left(-i \int_K dt' H_{\text{tun}}(t')_I\right) A(t)_I \rho_0\right]. \tag{3.21}$$

Here, we have introduced the time ordering operator T_K which orders all following operators along the Keldysh contour considering the Keldysh time.

To access the time evolution of the hybrid states, we introduce the propagator assuming the operator A is a projection operator of the form $|\chi_2\rangle\langle\chi_1|$. Here, χ_1 and χ_2 represents two hybrid states. As a result, the full propagator of the reduced system is given by

$$\mathbf{\Pi}(t, t_0) = \text{tr}_{\text{N}}\left[T_K \exp\left(-i \int_K dt' H_{\text{tun}}(t')_I\right) \rho_{\text{N}}(t_0)\right]. \tag{3.22}$$

This is a rank four tensor acting on the reduced density matrix ρ_{eff}. The time evolution of an initial dot state $P^{\chi_1'}_{\chi_2'}(t_0) = \langle\chi_1|\rho_{\text{eff}}(t_0)|\chi_2\rangle$ to a state at any time $P^{\chi_1}_{\chi_2}(t)$ can be computed with the help of $\mathbf{\Pi}$

$$P^{\chi_1}_{\chi_2}(t) = \sum_{\chi_1'\chi_2'} \mathbf{\Pi}^{\chi_1\chi_1'}_{\chi_2\chi_2'}(t, t_0) P^{\chi_1'}_{\chi_2'}(t_0). \tag{3.23}$$

The diagrammatic approach allows to visualize the tunneling processes responsible for the rate on the Keldysh contour. To do so, the exponential from Eq. (3.21) is expanded

$$T_K \exp\left(-i \int_K dt' H_{\text{tun}}(t')_I\right) = \sum_{n=0}^{\infty} (-i)^n \int_K dt_1 ... \int_K dt_n T_K \left[H_{\text{tun}}(t_1)_I ... H_{\text{tun}}(t_n)_I\right], \tag{3.24}$$

with $t_1 \leq ... \leq t_n$ to account for the time ordering. In the next step, the lead and hybrid operators are disentangled by taking into account a minus sign whenever hybrid and lead operator are interchanged. With Wick's theorem [141] it is possible to contract pairs of lead operators using

$$\left\langle a^\dagger_{\eta\mathbf{k}\sigma} a_{\eta'\mathbf{k}'\sigma'} \right\rangle = \delta_{\eta\eta'}\delta_{\mathbf{k}\mathbf{k}'}\delta_{\sigma\sigma'} e^{i\epsilon_{\eta\mathbf{k}\sigma}(t-t')} f^+(\epsilon_{\eta\mathbf{k}\sigma}), \tag{3.25}$$

$$\left\langle a_{\eta\mathbf{k}\sigma} a^\dagger_{\eta'\mathbf{k}'\sigma'} \right\rangle = \delta_{\eta\eta'}\delta_{\mathbf{k}\mathbf{k}'}\delta_{\sigma\sigma'} e^{i\epsilon_{\eta\mathbf{k}\sigma}(t-t')} f^-(\epsilon_{\eta\mathbf{k}\sigma}), \tag{3.26}$$

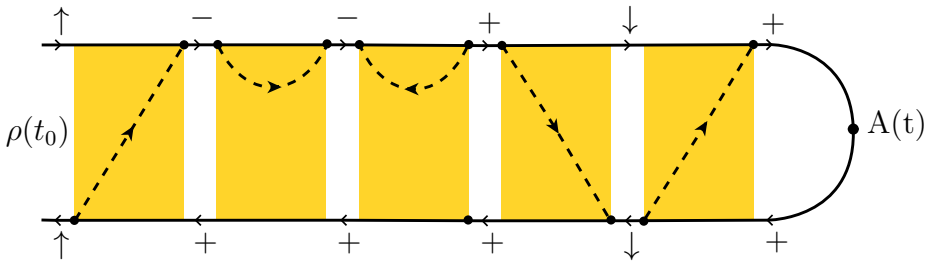

Figure 3.3.: Visualization of the time evolution of the reduced density matrix along the Keldysh contour. The example evolution starts at time t_0 on the upper branch of the contour. The reduced systems evolves along the contour until the time t is reached where the operator A is measured. Afterwards the time path is closed with the lower branch of the Keldysh contour. The tunnel Hamiltonians from the expansion in Eq. (3.24) gives rise to a vertex at which the hybrid state is changed. Each vertex is connected to another vertex by a direct tunneling line.

with the Fermi distribution $f^+(\omega) = 1/(1+\exp(\beta(\omega-\mu_\mathrm{N}))$ which is the probability to find a state with energy ω in the normal conductor occupied. The probability to find an unoccupied state under similar conditions is $f^-(\omega) = 1 - f^+(\omega)$. We remark that the equations above are written in a general form with an arbitrary number of leads with index η. For our system, η accounts only for the normal conducting lead. Hence, we use in the following $\epsilon_{\eta\mathbf{k}\sigma} = \epsilon$.

Figure 3.3 visualizes the time evolution of the reduced system on the Keldysh contour by combining Eqs. (3.20) and (3.24). The evolution starts at time t_0 and follows the upper branch of the Keldysh contour until the final time t is reached. At time t the operator A which is shown in the diagram as a black dot is measured. Afterwards the system evolves on the lower branch back to the initial time t_0. The expansion from equation (3.24) gives rise to a vertex for each tunnel Hamiltonian. Vertices are marked by black dots on the contour. The dashed lines between two vertices denotes pairwise contractions of the reservoir operators. The dashed lines have an orientation. At the vertex where the dashed line starts, an electron is annihilated and in the other vertex an electron is created, i.e. tunneling from the hybrid system to the quantum dot and vice versa, respectively.

The Keldysh contour in Fig. 3.3 consists of two types of blocks. First, the irreducible self-energies $W^{\chi_1\chi_1'}_{\chi_2\chi_2'}(t,t')$ describing the transition from a dot state $P^{\chi_1'}_{\chi_2'}$ at time t' to the state $P^{\chi_1}_{\chi_2}$ at time t. These blocks can be identified by taking vertical cuts through the diagram (yellow blocks in Fig. 3.3). If the vertical cut crosses at least one tunneling line the corresponding block is irreducible. In the case that no tunneling line is crossed, we find the second type of block which we denote as $\Pi^{(0)\chi_1\chi_1'}_{\chi_2\chi_2'}(t,t')$. This type of block separates two irreducible blocks. In this part of the diagram, the time evolution of the reduced quantum system is a free propagation. Taking into account the energy of the upper and lower branch of the Keldysh contour ϵ_{χ_1} and ϵ_{χ_2}, respectively, the free propagator is given by

$$\Pi^{(0)\chi_1\chi_1'}_{\chi_2\chi_2'}(t,t') = \delta_{\chi_1\chi_1'}\delta_{\chi_2\chi_2'}e^{-i(\epsilon_{\chi_1}-\epsilon_{\chi_2})(t-t')}. \tag{3.27}$$

Taking the sum over all alternating irreducible self energies and free propagators in the form of a Dyson equation, the full propagator of the reduced quantum system is

obtained

$$\mathbf{\Pi}(t,t_0) = \mathbf{\Pi}^{(0)}(t,t_0) + \int_{t_0}^{t} dt_2 \int_{t_0}^{t_2} dt_1 \mathbf{\Pi}^{(0)}(t,t_2)\boldsymbol{W}(t_2,t_1)\mathbf{\Pi}(t_1,t_0). \tag{3.28}$$

Multiplying the free propagator with $\rho_{\text{eff}}(t_0)$ by means of Eq. (3.23) and taking the time derivative with respect to t gives the formally exact master equation that describes the time evolution of the reduced density matrix for arbitrary initial states

$$\dot{P}^{\chi_1}_{\chi_2}(t) = -i(\epsilon_{\chi_1} - \epsilon_{\chi_2})P^{\chi_1}_{\chi_2}(t) + \int_{t_0}^{t} dt' \sum_{\chi_1'\chi_2'} W^{\chi_1\chi_1'}_{\chi_2\chi_2'}(t,t')P^{\chi_1'}_{\chi_2'}. \tag{3.29}$$

The first term on the right side of the master equation describes the coherent evolution of the hybrid system. The second term accounts for the dissipative coupling to the normal conductor. To calculate the matrix elements $W^{\chi_1\chi_1'}_{\chi_2\chi_2'}$ for our specific system, see Chapter 3.1, the following rules need to be applied [142]:

1. Draw all topological different first-order diagrams with fixed ordering of the vertices with respect to time. The vertices represents the tunneling of particles. The vertices are connected in pairs by tunneling lines carrying energy ω. All tunneling lines are normal.

2. For each vertical cut between two vertices assign a factor $1/(\Delta E + i0^+)$, where ΔE is the difference between the left- an right-going energies, including the energy of the tunneling particle ω.

3. For each tunneling line assign a factor $\Gamma_{\text{N}}/(2\pi)f^{\pm}(\omega)$ with Fermi function $f^+(\omega) = \{1 + \exp[(\omega - \mu_{\text{N}})/k_{\text{B}}T]\}^{-1}$ and $f^-(\omega) = 1 - f^+(\omega)$. The index $+$ $(-)$ applies for tunneling lines going backward (forward) in time with respect to the Keldysh contour.

4. Each vertex connects a hybrid state $|\alpha\rangle$ with $\alpha \in \{+,-\}$ to another hybrid state $|\sigma\rangle$ with $\sigma \in \{\uparrow,\downarrow\}$ by a tunneling line describing the tunneling of an electron with spin $\sigma' \in \{\uparrow,\downarrow\}$. For each bullet vertex assign a factor $\sqrt{1 - S_\alpha S_\sigma S_{\sigma'} \frac{\delta}{2\epsilon_{\text{A}}}}/\sqrt{2}$ with $S_{\alpha=+} = S_{\sigma=\uparrow} = S_{\sigma'=\uparrow} = 1$ and $S_{\alpha=-} = S_{\sigma=\downarrow} = S_{\sigma'=\downarrow} = -1$

5. Assign a global prefactor $-i$. Furthermore, assign a factor -1 for each bullet on the lower propagator and each outgoing (incoming) vertex ending (starting) in the state $|+\rangle$ or $|\uparrow\rangle$.

6. Integrate over the energy ω and sum over all diagrams belonging to one rate.

For representative calculations of the diagrams and the rate matrix for the density matrix elements $P \in \{P^+_+, P^-_-, P^\uparrow_\uparrow, P^\downarrow_\downarrow, P^-_+.P^+_-\}$, see Appendix A.

After calculating the rates from the diagrams, we obtain the master equation that describes the time evolution of an initial state in the hybridized basis. For a more intuitive picture, we transform the master equation into the pseudospin basis in the next part.

3.3. Pseudospin basis

The master equation can be transformed into a physically more intuitive form by introducing a pseudospin degree of freedom [74, 142]. Besides the pseudospin components, we take into account the real occupation of the quantum dot which is either even or odd. The new density matrix elements are given by

$$P_{\mathrm{e}} = P_{+}^{+} + P_{-}^{-}, \tag{3.30}$$

$$P_{\mathrm{o}} = P_{\uparrow}^{\uparrow} + P_{\downarrow}^{\downarrow}, \tag{3.31}$$

$$I_x = \frac{\Gamma_{\mathrm{S}}}{2\epsilon_{\mathrm{A}}} \cos\frac{\varphi}{2}\left(-P_{+}^{+} + P_{-}^{-}\right) + \frac{\delta}{4\epsilon_{\mathrm{A}}}\left(P_{+}^{-} + P_{-}^{+}\right), \tag{3.32}$$

$$I_y = -\frac{i}{2}\left(P_{+}^{-} + P_{-}^{+}\right), \tag{3.33}$$

$$I_z = \frac{\delta}{4\epsilon_{\mathrm{A}}}\left(P_{+}^{+} - P_{-}^{-}\right) + \frac{\Gamma_{\mathrm{S}}}{2\epsilon_{\mathrm{A}}} \cos\frac{\varphi}{2}\left(P_{+}^{-} + P_{-}^{+}\right). \tag{3.34}$$

With a base transformation, see Appendix B for details, we can calculate the matrix elements $W_{\chi_2\chi_2'}^{\chi_1\chi_1'}$ in the pseudospin base. In the infinite-gap limit, the dynamics of the pseudospin decouples from the dot occupations. The time evolution of the pseudospin is governed by a Bloch type equation [119]

$$\hbar\frac{d\mathbf{I}}{dt} = \mathbf{A} - \mathbf{R}\cdot\mathbf{I} - \mathbf{B}\times\mathbf{I}. \tag{3.35}$$

Here, $\mathbf{A}$ denotes the accumulation vector which describes the accumulation of pseudospin on the quantum dot due to tunneling of electrons. It is given by

$$\mathbf{A} = -\frac{\Gamma_{\mathrm{N}}}{4}\begin{pmatrix} \frac{\Gamma_{\mathrm{S}}}{\epsilon_{\mathrm{A}}}\cos\frac{\varphi}{2}\sum_{\gamma\gamma'=\pm}\gamma f(E_{\mathrm{A},\gamma',\gamma}) \\ \frac{\Gamma_{\mathrm{S}}}{\pi\epsilon_{\mathrm{A}}}\cos\frac{\varphi}{2}\sum_{\gamma\gamma'=\pm}\gamma\varphi(E_{\mathrm{A},\gamma',\gamma}) \\ \sum_{\gamma\gamma'=\pm}\left(1+\gamma\frac{\delta}{2\epsilon_{\mathrm{A}}}\right)\left[\frac{1}{2} - f(E_{\mathrm{A},\gamma',\gamma})\right] \end{pmatrix}, \tag{3.36}$$

where

$$f(x) = \frac{1}{1 + e^{\frac{x-\mu_{\mathrm{N}}}{k_{\mathrm{B}}T}}}, \tag{3.37}$$

denotes the Fermi function and

$$\varphi(x) = \mathrm{Re}\left[\psi\left(\frac{1}{2} + i\frac{x-\mu_{\mathrm{N}}}{2\pi k_{\mathrm{B}}T}\right)\right], \tag{3.38}$$

with the Digamma function $\psi(x)$.

The second term in Eq. (3.35) accounts for the anisotropic relaxation of the pseudospin in terms of the relaxation tensor $\mathbf{R}$. The relaxation tensor describes the decoherence in the system which arises from tunneling of single electrons between quantum

dot and normal conductor. The nonzero elements of the relaxation tensor are

$$R_{xx} = R_{yy} = \frac{\Gamma_\mathrm{N}}{2} \sum_{\gamma\gamma'=\pm} \left(1 - \gamma \frac{\delta}{2\epsilon_\mathrm{A}}\right) \left(\frac{1}{2} - \gamma' f(E_{\mathrm{A},\gamma',\gamma})\right), \tag{3.39}$$

$$R_{zz} = \frac{\Gamma_\mathrm{N}}{2} \sum_{\gamma\gamma'=\pm} \left(1 + \gamma \frac{\delta}{2\epsilon_\mathrm{A}}\right) \left(\frac{1}{2} - \gamma' f(E_{\mathrm{A},\gamma',\gamma})\right), \tag{3.40}$$

$$R_{xz} = R_{zx} = \frac{\Gamma_\mathrm{N}\Gamma_\mathrm{S}}{2\epsilon_\mathrm{A}} \cos\frac{\varphi}{2} \sum_{\gamma\gamma'=\pm} \gamma\gamma' f(E_{\mathrm{A},\gamma',\gamma}). \tag{3.41}$$

The last contribution to the pseudospin dynamics describes the precession of the pseudospin in an effective exchange field

$$\mathbf{B} = \mathbf{B}_0 + \mathbf{B}_1. \tag{3.42}$$

The exchange field has two contributions. The first one

$$\mathbf{B}_0 = \begin{pmatrix} 2\Gamma_\mathrm{S} \cos\frac{\varphi}{2} \\ 0 \\ -\delta \end{pmatrix}, \tag{3.43}$$

is due to the coupling to the superconductors and the level detuning of the quantum dot. The second contribution,

$$\mathbf{B}_1 = -\frac{\Gamma_\mathrm{N}}{2\pi} \begin{pmatrix} \frac{\Gamma_\mathrm{S}}{\epsilon_\mathrm{A}} \cos\frac{\varphi}{2} \sum_{\gamma\gamma'=\pm} \gamma\gamma' \varphi(E_{\mathrm{A},\gamma',\gamma}) \\ 0 \\ \sum_{\gamma\gamma'=\pm} \left(1 - \gamma \frac{\delta}{2\epsilon_\mathrm{A}}\right) \gamma' \varphi(E_{\mathrm{A},\gamma',\gamma}) \end{pmatrix}, \tag{3.44}$$

is due to the renormalization of the dot level positions which arises from virtual tunneling processes between the dot and the normal lead. The level renormalization is an interaction-driven effect that vanishes in the limit of a noninteracting quantum dot. Similar effects are known from quantum-dot spin valves and weakly coupled superconductor-quantum dot hybrids [143, 144]. Since $\mathbf{B}_1$ is of first order in the tunnel coupling Γ_N, it is in general much smaller than $\mathbf{B}_0$.

The proximity effect induces a superconducting pair amplitude on the quantum dot. In general, both an even-frequency spin-singlet as well as an odd-frequency spin-triplet pair amplitude can by induced. The latter require a broken spin-rotation symmetry [145] and, therefore, do not occur in our model. The spin-singlet pair amplitude given by

$$\mathcal{F} = \langle c_\downarrow c_\uparrow \rangle, \tag{3.45}$$

is closely linked to the pseudospin. In particular, the absolute value of the pair amplitude is given by the length of the projection of $\mathbf{I}$ into the x-y plane,

$$|\mathcal{F}| = \sqrt{I_x^2 + I_y^2}. \tag{3.46}$$

We remark that the absolute value of the pair amplitude is a dimensionless number that can take values in the range

$$0 \leq |\mathcal{F}| \leq 1/2. \tag{3.47}$$

3.4. Currents

Experimental access to the pair amplitude can be gained via the currents in the system. The currents in the superconductors can be related to the Green's function of the quantum dot using the approach of Ref. [146]. In the infinite gap limit [142, 147], the currents are given by

$$J_\eta = \frac{2e}{\hbar}\Gamma_\eta |\mathcal{F}| \sin\left(\Psi - \varphi_\eta\right), \tag{3.48}$$

where Ψ is the phase of the pair amplitude and the index $\eta \in \{\mathrm{SL}, \mathrm{SR}, \mathrm{N}\}$ accounts for the left and right superconductor and the normal conductor, respectively. As discussed in Chapter 2.3, the Josephson current flows between the superconductors

$$J_{\mathrm{Jos}} = \frac{1}{2}\left(J_{\mathrm{SL}} - J_{\mathrm{SR}}\right). \tag{3.49}$$

The Andreev current in the normal lead is given by

$$J_{\mathrm{And}} = -\left(J_{\mathrm{SL}} + J_{\mathrm{SR}}\right). \tag{3.50}$$

The currents in the superconducting leads can be written as [142]

$$J_{\mathrm{SL,SR}} = \frac{2e}{\hbar}\Gamma_{\mathrm{S}}\left(I_y \cos\frac{\varphi}{2} \mp I_x \sin\frac{\varphi}{2}\right). \tag{3.51}$$

Inserting this in the equations above yields

$$J_{\mathrm{Jos}} = \frac{2e}{\hbar}\Gamma_{\mathrm{S}} I_x \sin\frac{\varphi}{2}, \tag{3.52}$$

$$J_{\mathrm{And}} = -\frac{4e}{\hbar}\Gamma_{\mathrm{S}} I_y \cos\frac{\varphi}{2}. \tag{3.53}$$

Therefore, the currents are proportional to the isospin components I_x and I_y. Thus, measuring both currents simultaneously gives direct access to the dot's pair-amplitude dynamics.

3.5. Results

Now, we turn to the analysis of the pair-amplitude dynamics induced on the quantum dot by the superconducting proximity effect. First, we investigate the pair-amplitude dynamics after quenching the system. Afterwards, we turn to a periodically driven system in the adiabatic and fast driving limit.

3.5.1. Quench dynamics

In this part of the section, we analyze the relaxation of the pair amplitude on the quantum dot into the stationary nonequilibrium state after it has been quenched in an initial state at time $t_0 = 0$. In an analytic approach, we use that the accumulation vector $\mathbf{A}$ the relaxation tensor $\mathbf{R}$ and the exchange field $\mathbf{B}$ are time independent. We rewrite the Bloch equation, cf. Eq. 3.35, in the form

$$\hbar\frac{d\mathbf{I}}{dt} = \mathbf{A} + \mathbf{M}\cdot\mathbf{I}. \tag{3.54}$$

Here, the matrix $M_{ij} = -R_{ij} - \sum_k \epsilon_{ijk} B_j$ describes the evolution of the pseudospin due to relaxation and rotation around the exchange field. We can formally solve the equation with the following ansatz

$$\mathbf{I}(t) = \exp\left(\frac{\mathbf{M}}{\hbar}t\right)\mathbf{f}(t). \tag{3.55}$$

The time-dependent function $\mathbf{f}(t)$ is calculated as follows. First, we need to derive an expression for $\exp\left(\frac{\mathbf{M}}{\hbar}t\right)$. Using the left and right eigensystem of the matrix $\mathbf{M}$ [148], we get

$$\mathbf{M}\cdot\mathbf{r}_j = \lambda_j \mathbf{r}_j, \tag{3.56}$$
$$\mathbf{l}_j\cdot\mathbf{M} = \lambda_j \mathbf{l}_j, \tag{3.57}$$

with unnormalized left and right eigenvectors

$$\mathbf{l}_j = \begin{pmatrix} B_z(B_x + R_{yz}) + (B_y - R_{xz})(R_{xx} + \lambda_j) \\ B_z(B_y - R_{xz}) - (B_x + R_{yz})(R_{xx} + \lambda_j) \\ B_z^2 + (R_{xx} + \lambda_j)^2 \end{pmatrix}, \tag{3.58}$$

$$\mathbf{r}_j = \begin{pmatrix} B_z(B_x - R_{yz}) - (B_y + R_{xz})(R_{xx} + \lambda_j) \\ B_z(B_y + R_{xz}) + (B_x - R_{yz})(R_{xx} + \lambda_j) \\ B_z^2 + (R_{xx} + \lambda_j)^2 \end{pmatrix}, \tag{3.59}$$

respectively. For the calculation below, the eigenvectors need to be normalized which gives a nontrivial function. The corresponding eigenvalues λ_j are given by the zeros of the characteristic polynomial

$$\begin{aligned} 0 = &-2B_xB_zR_{xz} - B_x^2(R_{xx}+\lambda) - B_z^2(R_{zz}+\lambda) \\ &-(R_{xx}+\lambda)(-R_{xz}^2 + (R_{xx}+\lambda)(R_{zz}+\lambda)). \end{aligned} \tag{3.60}$$

For strong coupling, $\Gamma_\mathrm{S} \ll \Gamma_\mathrm{N}$, one of the eigenvalues is real and the other two are complex-conjugates of each other. Using the normalized eigenvectors, the normalization condition

$$\mathbf{1} = \sum_{j=1}^{3} \mathbf{r}_j \left(\mathbf{l}_j\right)^T, \tag{3.61}$$

is fulfilled. With the help of the left and right eigenvectors, the expression $\exp\left(\frac{\mathbf{M}}{\hbar}t\right)$ can be written as

$$\exp\left(\frac{\mathbf{M}}{\hbar}t\right) = \sum_{j=1}^{3} \exp\left(\frac{\lambda_j}{\hbar}t\right)\mathbf{r}_j\mathbf{l}_j^T. \tag{3.62}$$

With this expression, we can derive $\mathbf{f}(t)$. The first derivative of Eq. (3.55) is given by

$$\dot{\mathbf{I}}(t) = \exp\left(\frac{\mathbf{M}}{\hbar}t\right)\left(\frac{\mathbf{M}}{\hbar}\cdot\mathbf{f}(t) + \dot{\mathbf{f}}(t)\right). \tag{3.63}$$

Inserting this into Eq. (3.54) and using that $\mathbf{M}$ commutes with $\exp\{\pm\mathbf{M}\}$, we get a differential equation for $\mathbf{f}(t)$ which can be integrated with respect to time

$$\dot{\mathbf{f}}(t) = \exp\left(-\frac{\mathbf{M}}{\hbar}t\right)\mathbf{A}. \tag{3.64}$$

The solution for $\mathbf{f}(t)$ is given by

$$\mathbf{f}(t) = -\hbar\mathbf{M}^{-1}\exp\left(-\frac{\mathbf{M}}{\hbar}t\right)\mathbf{A} + \mathbf{C}, \tag{3.65}$$

with integration constant $\mathbf{C}$. By inserting the result for $\mathbf{f}(t)$ into Eq. (3.55), we obtain an expression for the pseudospin

$$\mathbf{I}(t) = \sum_{j=1}^{3}\exp\left(\frac{\lambda_j}{\hbar}t\right)\mathbf{r}_j\mathbf{l}_j^T\cdot\mathbf{C} - \mathbf{M}^{-1}\cdot\mathbf{A}. \tag{3.66}$$

Here, we have used the condition from Eq. (3.62). The integration constant can be expressed in terms of the initial quenched state of the pseudospin $\mathbf{I}^{(0)}$,

$$\mathbf{C} = \mathbf{I}^{(0)} + \mathbf{M}^{-1}\cdot\mathbf{A}. \tag{3.67}$$

Finally, we get the following analytic expression for the dynamics of the pseudospin after an initial quench

$$\mathbf{I}(t) = \sum_{j=1}^{3} e^{\frac{\lambda_j}{\hbar}t}\mathbf{r}_j(\mathbf{l}_j)^T\cdot\left(\mathbf{I}^{(0)} - \mathbf{M}^{-1}\cdot\mathbf{A}\right) + \mathbf{M}^{-1}\cdot\mathbf{A}. \tag{3.68}$$

Equation (3.68) shows that the pseudospin relaxes towards the stationary nonequilibrium state $\mathbf{M}^{-1}\cdot\mathbf{A}$ which is a nontrivial function of the accumulation term, the relaxation tensor and the exchange field. The pseudospin dynamics is driven by the difference between the initial value $\mathbf{I}^{(0)}$ and the stationary state. The dynamics shows in principle two different types of time dependence. On the one hand, the pseudospin relaxes exponentially towards the stationary state with a time constant $\hbar/\Gamma_\mathrm{N}$. Furthermore, there is an oscillatory time dependence which physically arises from a precession of the pseudospin around the exchange field. The precession frequency is given by the absolute value of the exchange field $|\mathbf{B}|$. For strong coupling, the frequency is given by

$$f_0 = \sqrt{\delta^2 + 4\Gamma_\mathrm{S}^2\cos^2\varphi/2}, \tag{3.69}$$

if we neglect contributions first order in Γ_N. This result is in agreement with a previous work on noninteracting superconductor-quantum dot hybrids which found an oscillation frequency of $2\Gamma_\mathrm{S}\cos\varphi/2$ [79]. For a given Γ_S in our system, the precession frequency can be manipulated by the superconducting phase difference φ and by the level detuning of the quantum dot δ. If the superconducting leads are ring shaped their phase can be controlled by the magnetic flux that passes through the ring [149]. The level detuning of the quantum dot can be manipulated by an external gate voltage. We remark that for a detuning much larger than the coupling Γ_S the superconducting proximity

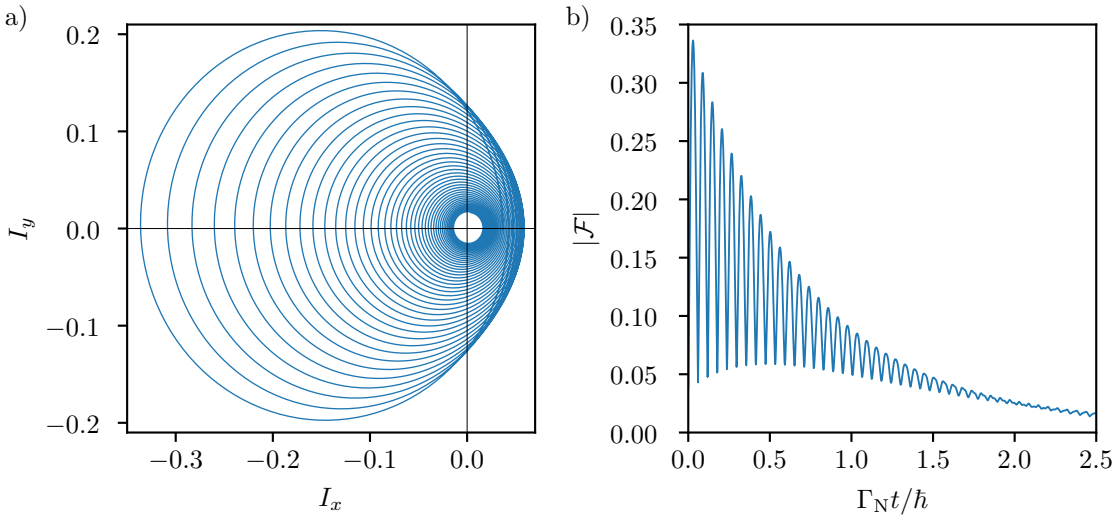

Figure 3.4.: a) Pseudospin in the x-y plane as a function of time after a quench from $\delta = -10\,U$ to $\delta = U/2$. The pseudospin dynamics starts close to the origin and ends after $t = 2.5\,\Gamma_N/\hbar$. The pseudospin rotates counter-clockwise around the exchange field. b) Pair amplitude $|\mathcal{F}|$ as a function of time. For both plots, we choose the parameters $\Gamma_S = U/10$, $\Gamma_N = 5 \times 10^{-3}\,U$, $\mu_N = U/2$, $k_B T = U/100$ and $\varphi = \pi/4$. *Reprinted with permission from Ref. [119]. Copyright 2024 by the American Physical Society.*

effect becomes suppressed which limits the possible precession frequency of the pair amplitude.

In the following, we analyze the quench dynamics for a situation where the quantum dot is prepared in an initial state with a large detuning $\delta = -10\,U$. In consequence, the dot is with a probability close to one doubly occupied which is represented by an initial pseudospin of $\mathbf{I}^{(0)} \approx (0, 0, 1/2)^T$. To start the dynamics, the detuning is subsequently changed to $\delta = U/2$. The time evolution of the pseudospin is calculated with Eq. (3.68). Figure 3.4 a) shows the projection of the pseudospin in the x-y plane. The projected dynamics starts close to the origin and precesses counterclockwise around the exchange field. The relaxation process resulting from single-tunneling events between the normal conductor and the quantum dot is clearly visible by the decreasing spiral movement. With the chosen parameters, the pseudospin follows an almost circular trajectory. A stronger coupling to the superconductors lead to a more elliptical trajectory since the x-component of the exchange field is proportional to the coupling strength to the superconductors. The y-component of the exchange field is zero if we neglect contributions first order in Γ_N. Now, we turn to the dynamics of the superconducting pair amplitude plotted in Fig. 3.4 b). The absolute value of the pair amplitude is given by the length of the pseudospin projection in the x-y plane. At the initial quench, $|\mathcal{F}|$ is small but quickly rises to its maximal value on a timescale $\hbar/\Gamma_S$ due to coherent tunneling of Cooper pairs between superconductors and quantum dot. Subsequentially, the coherent Cooper-pair tunneling gives rise to pronounced oscillations of the pair amplitude on the quantum dot on a timescale $\hbar/\Gamma_S$. In addition, there is an exponential decay of both the oscillatory amplitude and the average of the absolute value of the dot's pair amplitude. The relaxation results from single-electron tunneling between

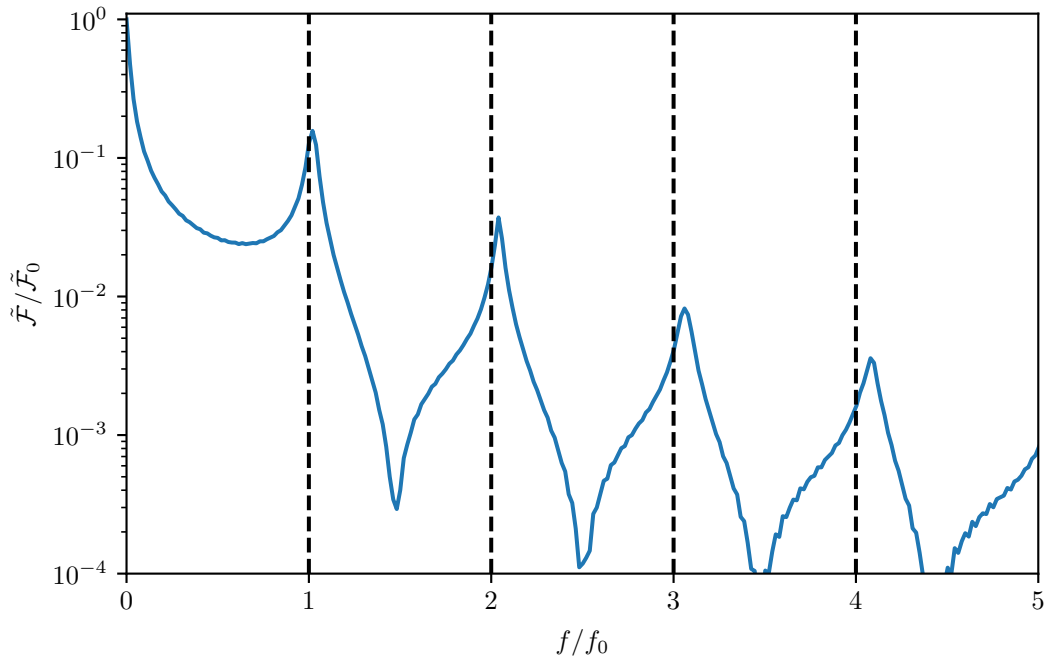

Figure 3.5.: Fourier spectrum of the pair-amplitude dynamics from Fig. 3.4.

normal conductor and quantum dot on a timescale of $\hbar/\Gamma_\mathrm{N}$. With increasing time, there is an interference of oscillations with different frequencies visible. A Fourier analysis, cf. Fig. 3.5, shows that the dominant frequency is given by f_0, see Eq. (3.69). Additionally, there are other frequencies visible in the Fourier spectrum that can be approximated by multiples of f_0. The deviation between the observed frequency and the corresponding multiple of f_0 increases with increasing frequency in a nontrivial manner because f_0 includes only the precession due to $\mathbf{B}_0$ and neglects corrections first order in Γ_N.

Experimental access to the pair-amplitude dynamics is gained by measuring the Josephson and Andreev current. According to Eqs. (3.52) and (3.53) the currents are proportional to the x- and y-components of the pseudospin. Figure 3.6 shows the dynamics of both currents as a function of time. The dynamics of the currents are similar to the pair-amplitude dynamics as expected. Both currents show an interplay of an oscillation on a timescale $\hbar/\Gamma_\mathrm{S}$ and an exponential decay on a timescale $\hbar/\Gamma_\mathrm{N}$. For a coupling strength of $\Gamma_\mathrm{S}/\hbar \approx 1\,\mathrm{GHz}$, the currents are expected to be in the sub-nA regime.

The advantage of the strong coupling over weak coupling between superconductors and quantum dot is the decoupling of the oscillation and relaxation timescales. Since both timescales are independently tuneable, it is possible to choose the oscillatory timescale smaller than the decay timescale which allows to explore rich pair-amplitude dynamics. Another previous work [78] investigates the Higgs-like pair amplitude dynamics in a similar system in the weak coupling limit. Here, a finite gap is considered and thus quasiparticle excitations are possible. The quasiparticle states provides a decay channel for the pair amplitude with a decay rate that is one order of magnitude faster than the precession frequency. Therefore, the decay of the pair amplitude dominates the dynamics after quenching the system and, thus, pair-amplitude oscillations

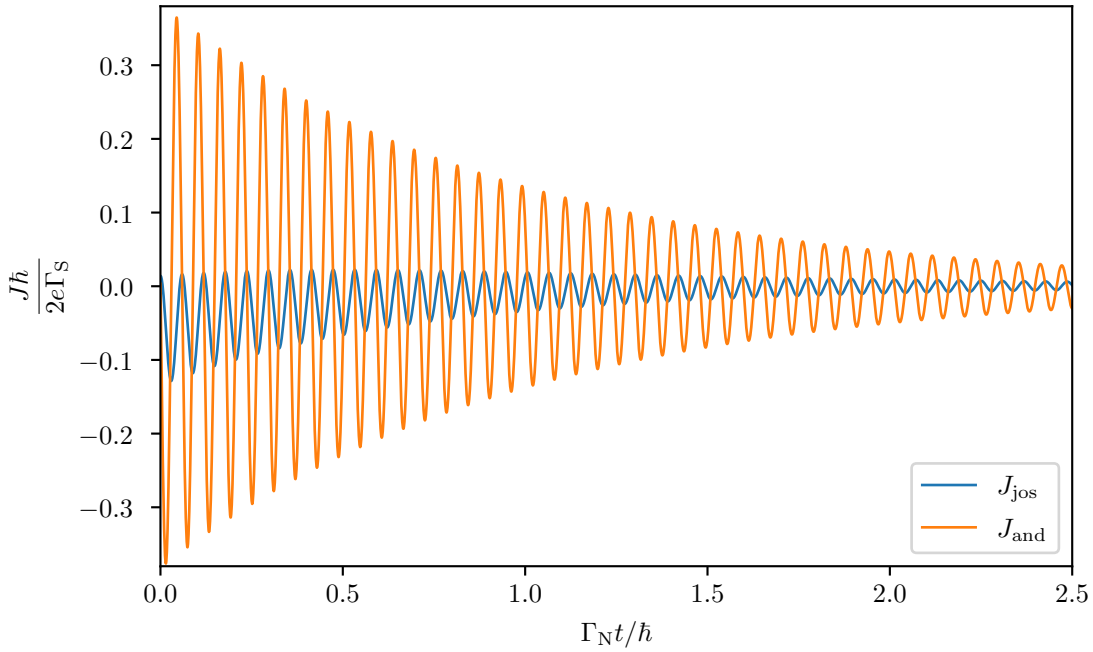

Figure 3.6.: Josephson and Andreev current as a function of time after a quench. The plot parameters can be taken from Fig. 3.4. *Reprinted with permission from Ref. [119]. Copyright 2024 by the American Physical Society.*

cannot be observed. To observe the dynamics of the pair amplitude also in the weak coupling limit, it is necessary to drive the system externally. The response of the pair amplitude in the strong coupling limit under external driving is discussed in the next part.

3.5.2. Adiabatic and fast driving

The damping of the pair amplitude can be overcome by driving the system externally which provides a continuous energy intake. In the following, we discuss two different approaches of driving the system which have the potential to give rise of interesting pair-amplitude dynamics. The first approach is driving the system in the adiabatic limit. The second one is driving the system fast. Possible driving parameters for the system are the phase difference between the superconductors and the level detuning of the quantum dot.

First, we discuss the response of the pair amplitude when the system is driven adiabatically. In this regime, the parameters of the system are changed on a timescale much smaller than the timescales of the dynamics in the system. In this case, the dot's pair amplitude can at any time t be approximated by the stationary solution of the master equation with the parameters given at time t. Hence, the driving frequency must satisfy $\hbar\omega \ll \Gamma$. In addition, the amplitude of the driving parameters needs to fulfill $\hbar\omega\delta_1 \ll (k_B T)^2$ or $\hbar\omega\Gamma_S \ll (k_B T)^2$ in the case of driving the level detuning with an amplitude δ_1 or the superconducting phase difference, respectively [150]. Since non-Markovian memory effects can be neglected in the adiabatic regime, the system is effectively in an instantaneous stationary state at any time which implies that the dynamic properties in the adiabatic regime can be deduced from the static properties

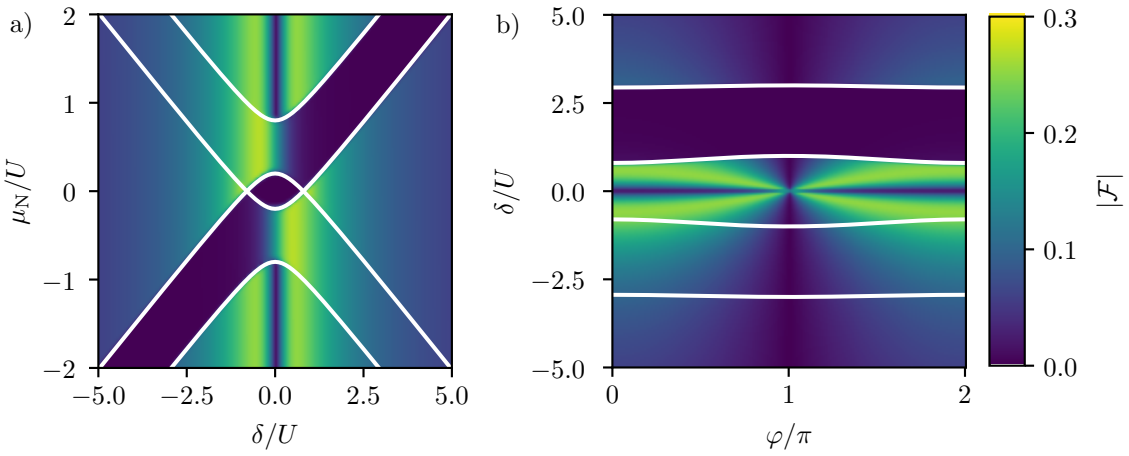

Figure 3.7.: Pair-amplitude as a function of a) chemical potential μ_N and detuning δ and b) detuning δ and phase difference φ in the adiabatic limit. The white contours mark the Andreev bound state energies. The parameters for the plots are $\Gamma_S = 0.3\,U$, $\Gamma_N = 5 \times 10^{-3}\,U$, $k_BT = 10^{-2}\,U$ and a) $\varphi = 0$ and b) $\mu_N = U$. *Reprinted with permission from Ref. [119]. Copyright 2024 by the American Physical Society.*

of our setup. As seen in the analysis of the pair-amplitude dynamics after a quench, the stationary solution of the pseudospin is a nontrivial function of the accumulation vector, relaxation tensor and the exchange field, see also Eq. (3.35). In Fig. 3.7 the dot's pair amplitude is shown as a function of a) detuning and chemical potential and b) detuning and phase difference between the superconducting leads. In Fig. 3.7 a), we find parameter regimes where the pair amplitude of the dot vanishes exactly. For negative detuning this happens between the Andreev bound state energies, cf. Eq. (3.15), $E_{A,+,-}$ and $E_{A,-,-}$ and for positive detuning between $E_{A,+,+}$ and $E_{A,-,+}$, cf. Fig. 3.2. By calculating the real dot occupation for these parameters, we find the quantum dot to be preferably single occupied in this region. Consequently, coherent tunneling of Cooper pairs between the superconductors and the quantum dot is suppressed.

In general, the pair amplitude takes finite values for other parameters. The strongest pair amplitude with up to $|\mathcal{F}| \approx 0.25$ is close to the particle-hole symmetric point $\delta = 0$ where the proximity effect is strongest. Investigating Fig. 3.7 a), we find different ways of driving the system to get pronounced oscillation of the pair amplitude. For example, one can fix the chemical potential $\mu_N = \pm U/2$ and drive the detuning by $\delta/U = \cos\omega t$ to get a smoothly changing pair amplitude. The resulting signal of the pair amplitude in the adiabatic limit is shown in Fig. 3.8 a) as a dashed line. For comparison, show the influence of a finite driving frequency by solving the master equation numerically with an initial pseudospin $\mathbf{I} = 0$. The results are taken after one period to allow the pseudospin to adjust to the external driving. As expected, the lower the driving frequency, the better is the agreement with the adiabatic solution. The deviation between the adiabatic and numeric solution is particularly large around the $\delta = U$ turning point of the detuning level driving. This behavior can be understood by assuming that the pseudospin has an inertia. At the $\delta = -U$ turning point, the smaller pair amplitude leads to a smaller deviation due to a lower inertia of the pseudospin.

Another possibility to drive the pair amplitude is by fixing the level detuning at e.g.

$\delta = \pm U/2$ and drive the pair amplitude by the chemical potential μ_N. In general, the pair amplitude is approximately constant as a function of chemical potential. However, if the chemical potential crosses an Andreev bound state energy there is a jump in the pair amplitude as clearly visible in Fig. 3.7 a).

To discuss the phase driving, we turn to Fig. 3.7 b) which results from a) for $\mu_\mathrm{N} = U$ and plotting it as a function of detuning δ and phase difference φ. As discussed above the pair amplitude $|\mathcal{F}|$ vanishes for detuning $E_{\mathrm{A},-,+} < \delta < E_{\mathrm{A},+,+}$. Similarly, the dot's pair amplitude vanishes for $\varphi = \pi$. Then, both the accumulation vector $\mathbf{A}$ and the exchange field $\mathbf{B}$ point exactly in z-direction. Thus, there is no x- or y-component generated for the pseudospin. For a sufficiently small level detuning $|\delta| \lesssim U$, we also find for phase detuning a considerable pair-amplitude gradient. A possible driving scheme is a linearly increasing phase difference $\varphi = \omega t$ for a fixed detuning $\delta = \pm U/2$. The resulting pair amplitude is plotted in Fig. 3.8 b) for $\delta = -U/2$. Similar to the driving of the level detuning, we compare our analytic solution in the adiabatic limit to the numeric solution of a driven system with frequency ω. As before, the deviation is strongest at the turning point of the driving where the pair amplitude is large. At the other turning point the pair amplitude is zero and there are no deviations visible.

As mentioned above, the pair amplitude is experimentally accessible by the time-dependent charge currents in the system. Interestingly, the Andreev current is in the adiabatic limit much smaller than the Josephson current. This results from the fact that the pseudospin accumulation generates only a small time-dependent y-component of the pseudospin, which is about three orders of magnitude smaller than the x- and z- components of the pseudospin. According Eqs. (3.52) and (3.53), this immediately implies that the Andreev current is always orders of magnitude smaller than the Josephson current. Therefore, it is possible to determine the pair-amplitude dynamics by taking only the Josephson current into account. In addition, this implies that the pair-amplitude dynamics under adiabatic driving is dominated by an oscillation of the absolute value of the pair amplitude while its phase is nearly constant. Thus, the pair amplitude mimics the Higgs mode in bulk superconductors. We remark that this result differs from Ref. [78], Here, it is shown that for weak coupling to the superconductors, the adiabatic driving excites the dynamics of both, the absolute value and the phase of the pair amplitude, unless specific driving schemes are applied.

We turn now to the discussion of the opposite limit when the system is driven with a frequency much greater than the coupling strength to the superconductors. Due to the AC Josephson effect discussed in Chapter 2.3, it is simple to achieve a fast oscillation of the phase difference. Therefore, we will discuss only the case of phase driving in the adiabatic limit. Nevertheless, the deviation for a driving of the detuning is analogue to the calculation below.

We tackle the problem in the limit of a large bias voltage applied to the normal conductor for three reasons. First, this minimizes the relaxation rate in the system such that we can expect a large pair amplitude. Second, if the chemical potential is much larger than the Andreev bound state energies, we can neglect level renormalizations which simplifies our analysis [74]. Finally, transport becomes unidirectional in the large bias limit which further simplifies the master equation to

$$\dot{\mathbf{I}} = \begin{pmatrix} 0 \\ 0 \\ -\Gamma_\mathrm{N}/2 \end{pmatrix} - \Gamma_\mathrm{N}\mathbf{I} - \begin{pmatrix} 2\,\Gamma_\mathrm{S}\cos\varphi/2 \\ 0 \\ -\delta \end{pmatrix} \times \mathbf{I}. \tag{3.70}$$

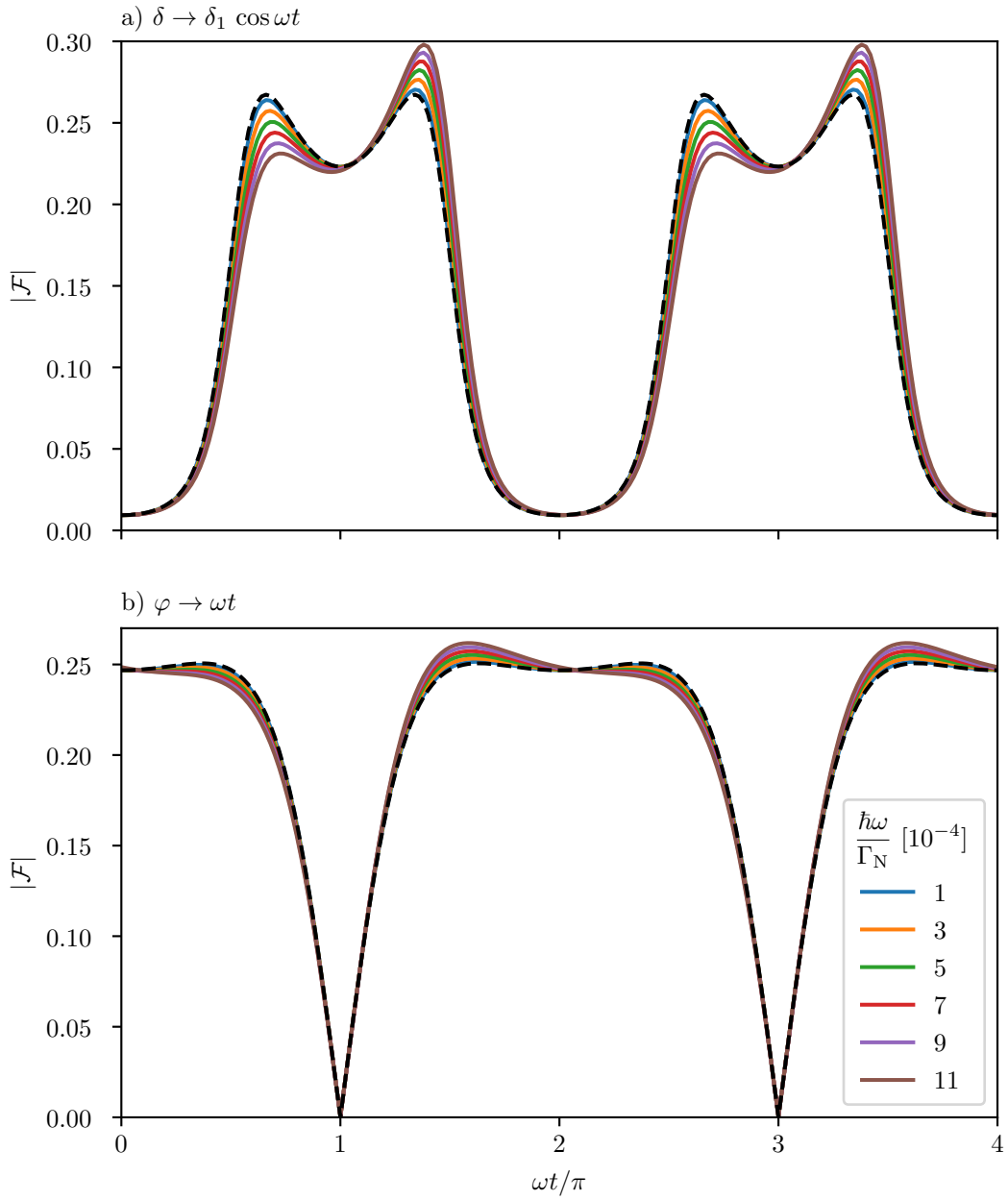

Figure 3.8.: Numerical result of driving the system with a) level detuning $\delta = \delta_1 \cos \omega t$ with $\delta_1 = U$ and b) superconducting phase difference $\varphi = \omega t$ for different driving frequencies ω. The dynamics is initiated with a pseudospin $\mathbf{I} = 0$. The results shown here are taken after one full period to allow the system to reach the dynamic equilibrium. The dashed line shows the analytic result in the adiabatic limit. The plot parameters are the same as in Fig. 3.7 and we choose in a) $\mu_N = U/2$ and in b) $\delta = -U/2$

In the fast driving limit, it is convenient to solve the master equation with a Fourier ansatz for the pseudospin [78]

$$\mathbf{I} = \sum_n \mathbf{I}_n \exp(in\omega t), \tag{3.71}$$

with $n \in \mathbb{Z}$. For a better readability, we double the frequency of the phase driving $\varphi = 2\,\omega t$. Only the exchange field $\mathbf{B}$ is a function of the phase difference. Therefore, it is decomposed into its Fourier components

$$\mathbf{B} = \mathbf{B}_0 + \mathbf{B}_+ \exp(i\omega t) + \mathbf{B}_- \exp(-i\omega t), \tag{3.72}$$

with $\mathbf{B}_0 = (0, 0, -\delta)^T$ and $\mathbf{B}_+ = \mathbf{B}_- = (\Gamma_\mathrm{S}, 0, 0)^T$ for phase driving. By inserting the Fourier ansatz into the master equation, we get

$$\sum_n in\omega \mathbf{I}_n e^{in\omega t} = \sum_n \left[\mathbf{A} - \Gamma_\mathrm{N}\mathbf{I}_n e^{in\omega t} - \left(\mathbf{B}_0 + \mathbf{B}_+ e^{i\omega t} + \mathbf{B}_+ e^{-i\omega t}\right) \times \mathbf{I}_n e^{in\omega t}\right]. \tag{3.73}$$

After a comparison of coefficients, we obtain an infinite hierarchy of equations for the Fourier components of $\mathbf{I}$,

$$\mathbf{G}_n\mathbf{I}_n + \mathbf{B}_{+,\times}(\mathbf{I}_{n-1} + \mathbf{I}_{n+1}) = \delta_{0n}\mathbf{A}, \tag{3.74}$$

with

$$\mathbf{G}_n = (\Gamma_\mathrm{N} + in\omega)\mathbf{1} + \mathbf{B}_{0,\times}. \tag{3.75}$$

Here, we have used that the linear mapping of the cross product can be written as a skew-symmetric matrix [151]

$$\mathbf{B} \times \mathbf{I} = \mathbf{B}_\times \mathbf{I}. \tag{3.76}$$

The type of Eq. (3.74) occurs generically in the Floquet analysis of driven quantum systems and can be solved by the method of matrix-continued fractions [152]. To this end, we introduce ladder operators for lowering and raising

$$\mathbf{L}_n\mathbf{I}_n = \mathbf{I}_{n-1}, \tag{3.77}$$
$$\mathbf{R}_n\mathbf{I}_n = \mathbf{I}_{n+1}, \tag{3.78}$$

the Fourier index n, respectively. The ladder operators can be calculated from Eq. (3.74) for the case $n \neq 0$. The result of the ladder operators are continued fractions

$$\mathbf{R}_{n-1} = -(\mathbf{G}_n + \mathbf{B}_{+,\times}\mathbf{R}_n)^{-1}\mathbf{B}_{+,\times}, \tag{3.79}$$
$$\mathbf{L}_{n+1} = -(\mathbf{G}_n + \mathbf{B}_{+,\times}\mathbf{L}_n)^{-1}\mathbf{B}_{+,\times}. \tag{3.80}$$

With the ladder operators, it is possible to determine $\mathbf{I}_0$ from Eq. (3.74) for $n = 0$

$$\mathbf{I}_0 = [\mathbf{G}_0 + \mathbf{B}_{+,\times}(\mathbf{R}_0 + \mathbf{L}_0)]^{-1}\mathbf{A}. \tag{3.81}$$

The required ladder operators $\mathbf{R}_0$ and $\mathbf{L}_0$ can be calculated from Eqs. (3.79) and (3.80) without violating the ansatz $n \neq 0$. With the raising and lowering operators and $\mathbf{I}_0$, we get a full analytic expression for the pseudospin dynamics for fast driving

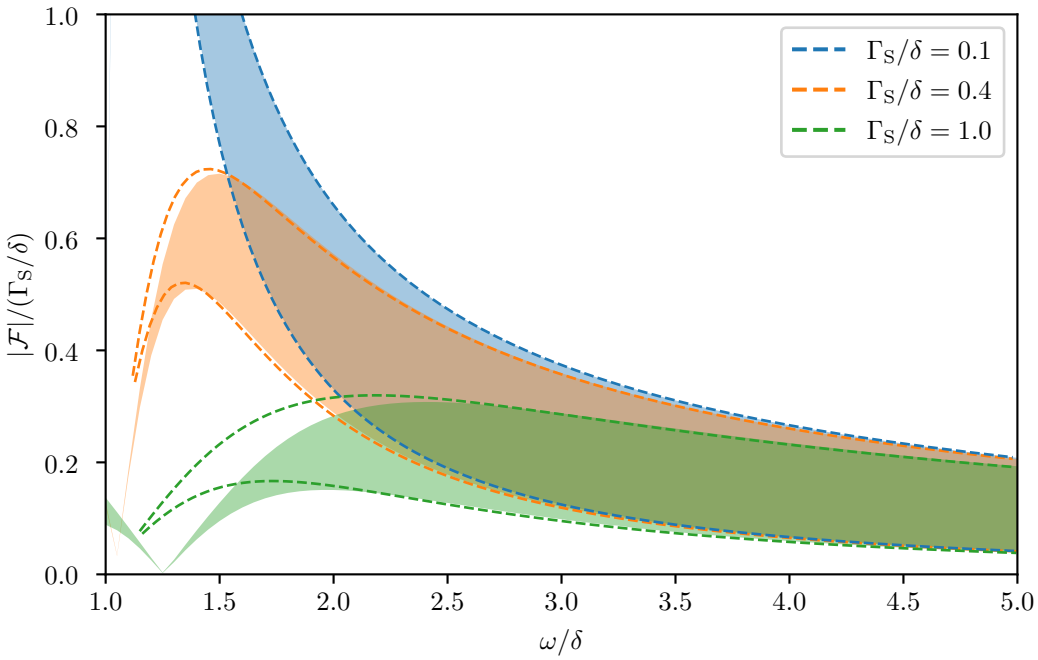

Figure 3.9.: Oscillation amplitude of the pair-amplitude dynamics as a function of the external driving frequency in the fast-driving limit for three different coupling strengths to the superconductors. The dashed lines mark the solution of our analytic approximation and the filled areas the solution of a numeric calculation. For each driving frequency, the plot marks the upper and lower bound of the pair amplitude. The plot parameters are $\Gamma_N = 5 \times 10^{-3}\, U, \delta = U, \mu_N = -10\, U$ and $k_B T = U/100$. *Reprinted with permission from Ref. [119]. Copyright 2024 by the American Physical Society.*

in the infinite bias limit. Formally, the continued-fraction method is a systematic expansion in $\Gamma_S/(\hbar\omega)$. In the fast driving limit, it is sufficient to take only the ladder operators $\mathbf{R}_0$ and $\mathbf{L}_0$ into account. Since we stop evaluating after $\mathbf{R}_0$ and $\mathbf{L}_0$, we neglect the generation of higher harmonics. As discussed in Ref. [78] for the pair-amplitude dynamics of a quantum dot weakly coupled to superconductors with a finite gap, the amplitude of higher harmonics is suppressed as the quantum dot cannot follow the external driving at extremely high frequencies. Therefore, the pseudospin dynamics is suitably described by the Fourier components $\mathbf{I}_0$ and $\mathbf{I}_\pm$.

In Figure 3.9, we show the amplitude of possible pair-amplitude dynamics as a function of driving frequency ω. For sufficiently large driving frequencies, our analytic approach (dashed lines) and the numeric solution (filled area) almost coincide. The smaller the coupling strength between superconductor and quantum dot the earlier we see an agreement between the simulation and our analytic result. Interestingly, the agreement does not improve when we take additional ladder operators and Fourier components into account. The system is able to follow the external driving up to high frequencies that are larger than the coupling to the superconductors. For fast driving, the average pair amplitude scales with $(\Gamma_S/\omega)^2$. This in strong contrast to the system with weakly coupled superconductor-quantum dot hybrids [78] where the pair-amplitude dynamics is strongly suppressed under fast-driving conditions.

3.6. Summary

In this chapter, we have discussed the transient pair-amplitude dynamics of a three-terminal system consisting of two superconductors strongly coupled to a quantum dot which is weakly coupled to a normal conductor. The focus of our investigation has been the nonequilibrium dynamics after quenching the system and under driving the system externally in the adiabatic and fast driving limit.

We have focused on the subgap physics of the system. Therefore, we have considered the system in the infinite-gap limit. Hereby, we have gotten an effective Hamiltonian describing the hybrid system of superconductors and quantum dot. With a real-time diagrammatic approach, we derived a master equation for the reduced density matrix of the hybrid system. With the transformation to the pseudospin basis, we have gotten an intuitive picture to interpret the pair-amplitude dynamics.

To describe the dynamics after a quench, we have derived a compact analytic solution of the Bloch type master equation for the pseudospin. It shows that the relaxation is a result of the tunneling of single electrons between dot and superconductor and the oscillation is due to the coherent tunneling of Cooper pairs between dot and superconductors. The solution gives us deep insights into the dynamics and makes it possible to design the pair-amplitude oscillations by its frequency and shape. In the framework of the pseudospin, the oscillation is nothing but a precession of the pseudospin around the exchange field determined by the level detuning and the phase difference between the superconductors. Both are well controllable parameters in an experiment.

In the limit of adiabatically driving the system, we have found a strong influence of the Andreev bound states. At the Andreev bound states, the pair amplitude shows a discontinuity due to Coulomb blocking of the pair amplitude when the dot becomes preferably singly occupied. The analysis of the pseudospin has revealed that the phase of the pair amplitude is constant under adiabatic driving. Therefore, the dynamics excited by the adiabatic driving shows a Higgs-like behavior.

The fast driven superconductor-quantum dot hybrid can be described within the infinite-bias limit by considering the Fourier components of the pair amplitude. In principle, the Fourier solution is exact if all Fourier components are taken into account. It is possible to derive any Fourier component from the zeroth Fourier component $\mathbf{I}_0$ which can be expressed in a compact form. However, for the calculation it is necessary to take only a limited number of Fourier components into account. We have found that it is sufficient to describe the pseudospin dynamics by $\mathbf{I}_0$ and $\mathbf{I}_\pm$. The analysis has revealed that the strongly-coupled system is able to follow the external driving up to frequencies significantly larger than the coupling strength to the superconductors.

4. Relaxation and transport dynamics of photoexcited electrons

In this chapter, we set up a model to describe the relaxation and transport dynamics of photoexcited electrons in metals. First, we introduce a trajectory-based simulation which follows the path of the electrons from the back side to the front side of the sample. Along the path, the electrons scatter with other electrons and exchange energy. The simulation is used to describe the transport phenomena measured in pump-probe experiments in Fe/Au heterostructures, see Refs. [8, 105, 106]. In the experiment, the pump and probe pulses are spatially separated on opposite sides of the sample. With this measurement scheme, it is possible to reveal the transport features of the electrons in the sample. A material-specific real-time time-dependent density functional theory provides insights into the spin-dependent excitation and injection pattern at the Au/Fe interface [9]. Our simulation is a complementary theory which analyzes the transport and relaxation dynamics of the excited electrons from the Fe/Au interface to the Au surface where the electrons are probed. In the following, we set up the model for the simulation. Afterwards, we discuss the results of the simulation and how they compare to the experimental results. With further investigation, we reveal the underlying transport mechanisms which can be used to identify the ballistic and superdiffusive transport regime. These results have already been published in Ref. [9]. Afterwards, we complete the possible transport regimes by an analysis of the transport effects in a diffusive regime. Here, we model the relaxation dynamics based on the Boltzmann transport equation which is extended by a diffusive propagation of the particles. Finally, we discuss a hopping model to estimate the number of necessary collisions to identify diffusive transport in the trajectory-based simulation.

4.1. Trajectory-based model

We simulate classical, quasiballistic electron trajectories which are injected into a sample of length d at $z = 0$. The sample is assumed to have an infinite lateral extent in the x- and y-direction which is a valid assumption if the sample width is much larger than the mean free path of the electrons. Initially the electron starts the trajectory with an energy E which is chosen randomly from a Gaussian distribution,

$$P(E) = \frac{1}{\sqrt{2\pi(\Delta E)^2}} e^{-\frac{(E-\bar{E})^2}{2(\Delta E)^2}}, \tag{4.1}$$

with mean value $\bar{E} = 1.7\,\mathrm{eV}$ and standard deviation $\Delta E = 0.1\,\mathrm{eV}$. The variables of the distribution are chosen such that they are in agreement with the experimental observation and the calculation from the real-time time-dependent density functional theory. Besides the energy and place, the electrons get an initial direction and propagation length. At injection, the direction is chosen randomly with uniform angular

distribution on a half sphere in order to ensure propagation in the forward (positive z-) direction. The propagation length l is also a random quantity which depends on the energy-dependent mean free path λ. We assume that each electron propagates ballistically over a distance l which is randomly chosen from the distribution

$$P(l) = \frac{1}{\lambda} e^{-l/\lambda}. \tag{4.2}$$

The mean free path can be related to the electron lifetime τ

$$\lambda = \tau v_{\mathrm{F}}, \tag{4.3}$$

via the Fermi velocity v_{F} [113, 153]. In the considered energy range, the Fermi velocity is with a good approximation constant and energy independent with $v_{\mathrm{F}} = 1.4\,\mathrm{nm/fs}$ in bulk gold [154–156]. To get an analytic and realistic energy-dependent lifetime, we parameterize the experimentally determined electron lifetime in gold [99, 105, 106] by

$$\tau = \frac{\tau_0}{1 + \left(\frac{E - E_{\mathrm{F}}}{E_0}\right)^2}. \tag{4.4}$$

Here, $\tau_0 = 170\,\mathrm{fs}$ and $E_0 = 1\,\mathrm{eV}$ provides the best fit to the data. The choice of E_0 differs from standard Fermi liquid theory where the energy unit is $k_{\mathrm{B}}T$ [12]. Due to the anomaly of the electron lifetime in gold at $\sim 1.5\,\mathrm{eV}$, Fermi liquid theory does not describe the electron lifetime in our considered energy range well, see Ref. [99] for a comparison of various lifetime models. When we insert Eqs. (4.3) and (4.4) into Eq. (4.2), we obtain an energy-dependent distribution function for the propagation length which is customized for our specific system.

After the initial parameters are set, the electron propagates with Fermi velocity over the distance l. If the electron does not reach the surface, it collides with another electron which has two consequences. First, the electron transfers a random amount of energy ΔE which is uniformly distributed in the interval $[0, E - E_{\mathrm{F}}]$ to a secondary electron. The secondary electron is excited to a random energy in the interval $[E_{\mathrm{F}}, E_{\mathrm{F}} + \Delta E]$ depending on the previous energy state below the Fermi energy. Using the current position as starting point, the trajectory of the secondary electron is included in the simulation sweep. Second, the electron gets a new random direction chosen from an isotropic distribution on a full sphere and a new propagation length according to the distribution in Eq. (4.2). The secondary electron ensures energy and momentum conservation during the scattering process. We neglect energy redistribution between excited electrons due their small share compared to the total number of electrons in the sample.

The trajectories are simulated until the electrons reach the sample surface at $z = d$. We also need to define criteria where the simulation sweep is aborted to avoid unnecessary calculation costs. The first stop criterion monitors the electron energy. When the energy drops below a threshold value of $0.5\,\mathrm{eV}$ above the Fermi energy the corresponding electron is discarded from the simulation. The threshold value is chosen according to the detectable energy in the experiment [9]. The work function at the measuring spots is approximately $4.5\,\mathrm{eV}$. Therefore, it is not possible to measure below $0.5\,\mathrm{eV}$ with the $4\,\mathrm{eV}$ probe laser. A positive side effect is that the threshold limits the number of electron trajectories in a single sweep. Electrons are also discarded when

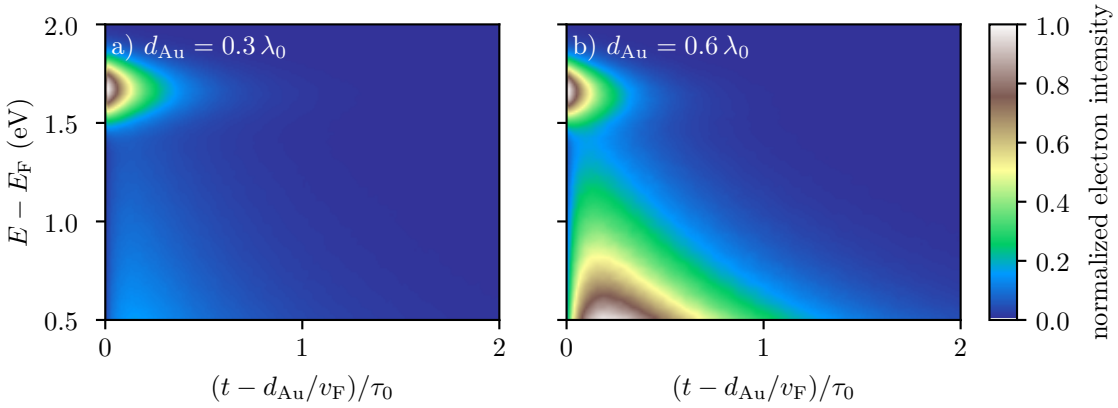

Figure 4.1.: Normalized electron intensity as a function of energy and time for a sample thickness of a) $0.3\,\lambda_0$ and b) $0.6\,\lambda_0$ with $\lambda_0 = v_F\tau_0$. For a better comparison, we choose a thickness-dependent time zero which is determined by the propagation time of ballistic electrons. *Adapted from Ref. [9] under Creative Common Attribution 4.0 International license.*

their z-position becomes negative. In terms of our considered systems, a negative z-component means that the electrons are injected back to the iron layer. Since the relaxation time in iron is much smaller than in gold [105], it is unlikely that the electrons are injected again to the gold layer and reach the surface with an energy above the threshold energy. For a detailed simulation algorithm, see Appendix C. To generate the results discussed below, we record in each simulation sweep the total path length, which is directly linked to the propagation time, the final energy, the number of collisions along the trajectory and the initial propagation direction. In total, we simulate $2 \cdot 10^7$ sweeps following the trajectory of the initial and associated electrons across the sample for each sample thickness.

4.2. Energy- and time-dependent intensity spectra

In the following, we discuss the results generated by the simulation. We start with a comparison of the result of the simulation with the experiment [9] on a qualitative level. In the evaluation process for the electron intensity which is the probability to measure an electron with an energy $E - E_F$ after the time t, the trajectories are sorted according to their final energy and propagation time. For the energy, we consider the interval $(E - E_F) \in [0.5\,\text{eV}, 2\,\text{eV}]$ with a bin width of 25 meV. The considered time interval is set by $t \in [d/v_F, d/v_F + 2\,\tau_0]$ with a bin width of $2 \cdot 10^{-2}\,\tau_0$. Here, the lower time limit d/v_F is set by ballistic electrons crossing the sample fastest as discussed in Chapter 2.4.

The simulation results are shown in Fig. 4.1. We want to highlight the qualitative agreement between the simulated electron intensities and the measured two-photon photoelectron emission spectroscopy in Fig. 2.9 [9, 106].

For both thicknesses, a significant amount of electrons reaches the sample surface with their original injection energy around 1.7 eV at time $t = d/v_F$. This shows essentially that these electrons propagate ballistically, i.e. without any scattering through the sample in a direction parallel to the z-axis. For both thicknesses, the intensity of

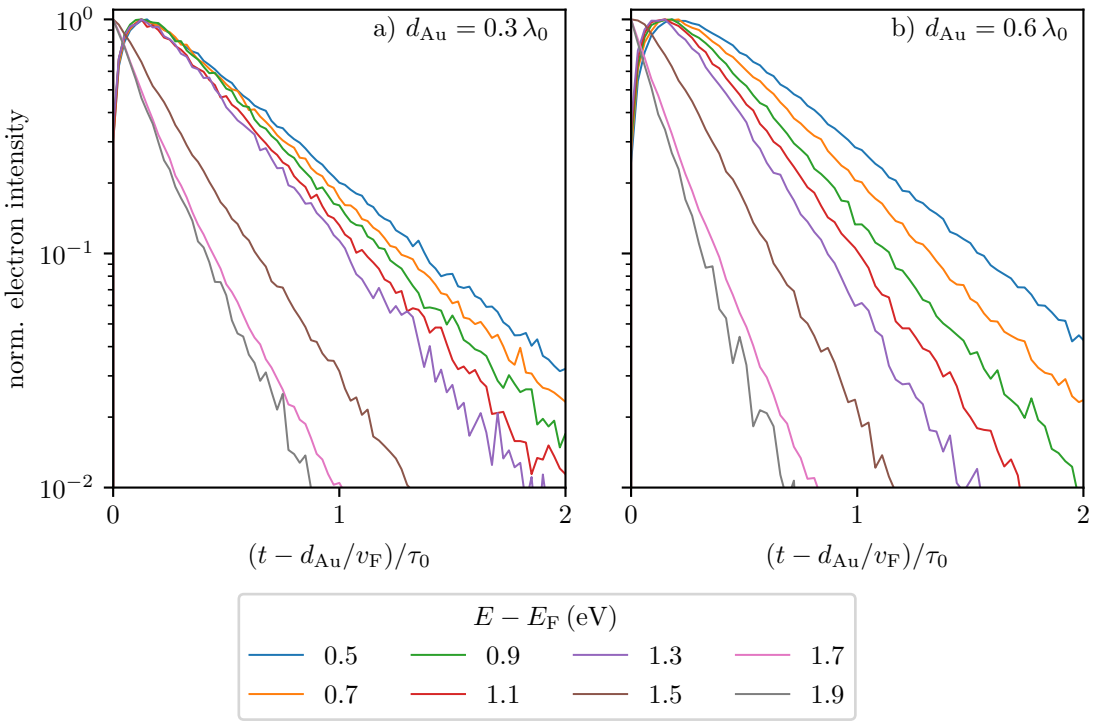

Figure 4.2.: Time evolution of the electron intensity for depicted energies from the spectra in Fig. 4.1 normalized to the maximum intensity of each energy. *Adapted from Ref. [9] under Creative Common Attribution 4.0 International license.*

the feature at 1.7 eV decays exponentially as a function of time as depicted in Fig. 4.2. In thin samples, cf. Fig. 4.1 a), there is a minor feature in the energy range [1.5 eV-0.5 eV]. Since electrons are not injected at this energy the electrons must have collided at least once in order to transfer energy to a secondary electron. When the mean free path is much larger than the sample thickness, a scattering event is unlikely. Therefore, in the thicker sample, cf. Fig. 4.1 b), this feature is more pronounced. Here, inelastic scattering events have a higher probability to occur during propagation because the average path length is much larger. The intensity at lower energies show a different behavior as a function of time compared to energies originally injected. As it is clearly visible in Fig 4.2, the intensity builds up, reaches a maximum and finally decays exponentially with time. In the experiment, cf. Ref. [105], there is no distinguishable shape of the high and low energy feature due to the finite laser pulse widths. The maxima are the most likely transit time of the electrons with a certain final energy. The exact position of the maxima are a function of energy and sample thickness. Therefore, the transport characteristics can be accessed via the relative shift of the maxima as a function of sample thickness which is part of the next section.

So far, we have discussed the agreement between our simulation and the experiment on a qualitative level. On a quantitative level, there is a deviation in the sample thicknesses between simulation and experiment. With $\lambda_0 = 240\,\mathrm{nm}$, the given thicknesses correspond to a) 72 nm and b) 144 nm. In the experiment, a qualitatively equivalent result to Fig. 4.1 b) can be found e.g. at a gold layer thickness of 25 nm or 60 nm which is almost six or three times smaller than expected by the simulation. The major impact could come from neglecting reinjection and reflection at the surfaces at $z = 0$

and $z = d$. The resulting longer trajectories could bias the correct share of scattered and unscattered electrons with increasing time.

Two processes come into mind when including interface processes. The first one is the backscattering into the iron layer and reinjection into the gold layer afterwards. In the iron layer, the electron could transfer a lot of energy in a short time due to the much smaller lifetimes and mean free paths. We assume that this process does not effect the result much since the small lifetimes push the electron energy fast below the threshold. Another process could be reflections at the interfaces Fe/Au and Au/vacuum. This process is related to the question what happens in the experiment after the electron hits the surface. In the simulation, electrons are absorbed after reaching the surface. In the experiment, there is no possibility to escape the sample before the probe laser pulse emits the electrons. Thus, an electron that contributed first to the high energy feature could at a later time contribute to the low energy feature. This process could lead to a more pronounced intensity of the low energy feature and, therefore, leading to a better agreement between simulation and experiment on the quantitative level.

Another impact might be the assumption of the distribution of the initial energy. We have assumed that the electrons are injected with a random energy that is normally distributed with an average energy of 1.7 eV. According to previous experiments and DFT calculations, the electrons are excited mainly in the iron layer in a broad energy spectrum. In addition, the lifetimes in iron are much smaller than in gold. Therefore, the electrons have already been in a relaxation process before reaching the interface to the gold layer. Thus, it is possible that electrons are injected at a lower energy into the gold layer. However, in the experimental result the energy feature at low energies show a clear time delay which indicates that the low energies are populated from higher energy electrons. Hence, the majority of electrons is injected at 1.7 eV which we used in our model [9, 106].

4.3. Insights of the effective electron velocity on the transport regime

In this part, we make use of the detailed information of the simulation to extract possible transport characteristics from the thickness-dependent behavior of the electron energies. Similar to the experiment [9], we define an effective electron velocity given by

$$v_{\text{eff}} = \frac{d}{t - t_0}, \tag{4.5}$$

with maximum position t and position of the reference maximum t_0. In line with the experiment, we choose the highest energy maximum as reference which corresponds to the time in which ballistic electrons propagate through the sample, see Chapter 2.4

For the evaluation of the effective electron velocity, we estimate the peak position of the energies depicted in Fig. 4.2 for sample thicknesses equally distributed in the range $d/\lambda_0 \in [0.05, 0.7]$ with a spacing of $\Delta d = 0.05\,\lambda_0$. Below $d = 0.05\,\lambda_0$, we choose a higher resolution with a spacing of $\Delta d = 0.01\,\lambda_0$ because the time delay changes faster in the beginning. Motivated by the experiment, we subtract the maximum position of the ballistic electrons t_0 for each energy and sample thickness. Per definition, the

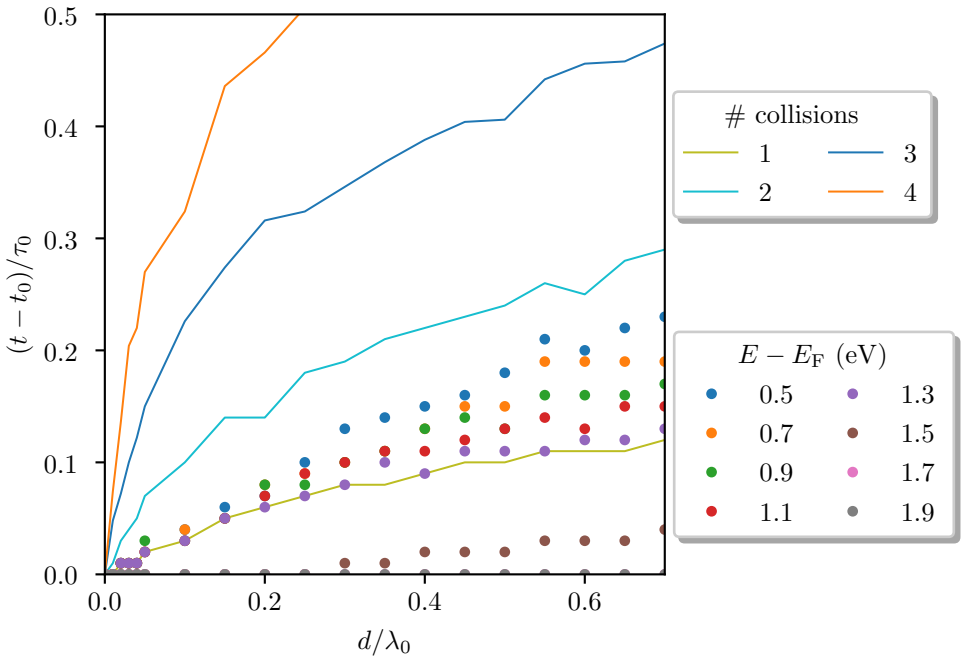

Figure 4.3.: Comparison of the simulated time delay $(t - t_0)$ for different energies as a function of d and the simulated time delay of trajectories with a fixed number of inelastic scattering events.

time delay is zero at $d = 0$. Figure 4.3 shows the simulated time delay $(t - t_0)$ for different energies as a function of sample thickness as data points. For comparison, we sort the simulated trajectories not by energy but by the number of collisions along the trajectory. The resulting time evolution of the intensity is similar to Fig. 4.2. Analogue to the energy groups, we estimate the maximum position for each collision group and calculate the time delay compared to the zero collision group which corresponds to ballistic electrons. In Fig. 4.3, we see that the high energies above 1.5 eV consists of electrons that propagate ballistically through the sample. Electrons at the lower boundary of the initial energy range at 1.5 eV collide on average also less than one time. We conclude that the majority of these electrons propagate ballistically through the sample. All energies below 1.5 eV collide on average at least one time. The lower the energy of the electrons the larger is the time delay. Consequently, the average number of collisions is higher when the final energy of the electrons is lower. The relationship between the number of collisions and the energy fulfills our expectations since with every inelastic scattering event the initial energy decreases. The time delay of the electrons with a fixed number of collisions rises linearly for small thicknesses. The shape changes to a sublinear dependence over a crossover range. For the one collision group, the crossover range already starts from the beginning. The higher the number of collisions in a group the later the crossover initiates. The sublinear dependence is a clear sign of superdiffusive transport since for diffusive transport it is expected that the time delay increases quadratically, cf. Eq. (2.32).

At first glance, it is surprising to find that the ballistic electrons are detected at the highest energies. According to the relaxation times, cf. Eq. (4.4), a higher energy has a lower relaxation time and consequently a shorter mean free path. Due to the Fe/Au

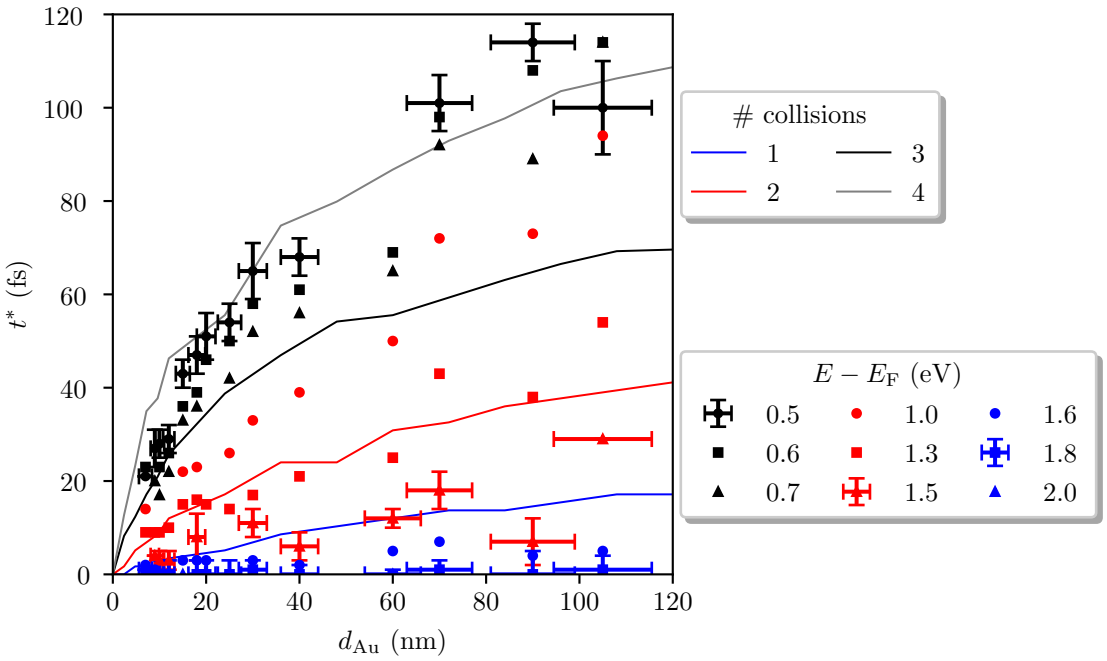

Figure 4.4.: Comparison of the experimentally measured time delay t^* for different $E - E_{\mathrm{F}}$ as function of d_{Au} and the simulated trajectories with a fixed number of collisions. The simulated results are scaled to the SI unit system assuming a ballistic velocity $v_{\mathrm{F}} = 1.4\,\mathrm{nm/fs}$ and $\tau_0 = 170\,\mathrm{fs}$. For a better visibility, only representative error bars are given for each group. *Adapted from Ref. [9] under Creative Common Attribution 4.0 International license.*

interface, the electrons injected to the gold layer have a restricted energy around 1.7 eV. Consequently, electrons with a final energy below 1.5 eV must have been part of at least one scattering event. Thus, electrons with an energy below 1.5 eV cannot propagate ballistically. On the other side, it is possible that high-energy electrons transfer only a small amount of energy to a secondary electron and stay inside the high-energy range above 1.5 eV. However, the share of high energy electrons with one or more collisions is so small that the time delay to ballistic electrons is zero. Only electrons with a final energy of 1.5 eV show a time delay greater than zero at thicknesses $d \geq 0.3\,\lambda_0$. This energy marks the transition from the ballistic to the superdiffusive transport regime for our chosen parameters.

In the next step, we compare the experimentally obtained time delays with our collision analysis, cf. Fig. 4.4. The energy data points are grouped into lower (black), intermediate (red), and higher energy (blue). These groups have an average number of inelastic collisions in the range three to four, one to three and less than one, respectively. In the latter group, we primarily find electrons with their original injection energy which is a clear signature of ballistic transport. The electrons at all the lower energies experience up to four scattering events. Since a sublinear increase is clearly visible, the electrons propagate in the superdiffusive transport regime. The experimental technique is not able to detect electrons that propagate diffusively because at all measured energies the electrons cross the sample either ballistically or superdiffusively. We expect from our analysis to find diffusive electron transport at energies close to the Fermi edge. This expectation is in agreement with a similar experiment [8]. In this

work, the electron dynamics close to the Fermi edge is studied in a back-pump front-probe geometry on a similar sample. The result is compared with a two-temperature model that assumes diffusive transport through the sample. For sufficiently large d_{Au} the experimental result and the theoretical model matches quantitatively which indicates diffusive transport.

A comparison between Fig. 4.3 and 4.4 reveals that in the simulation the average number of collisions is much smaller than in the experiment for energies below 1.5 eV. One possible explanation is our assumption on the relaxation process. We assume that the electrons transfer a random, uniformly distributed amount of energy to a secondary electron which could deviate from reality. The assumed energy loss is on average half the initial energy which means that most probably most electrons scatter up to one time since the sample thickness is smaller than the mean free path. If, as discussed above, we take reflections at the interface into account, we do not expect that the result changes much because it is still the case that the electron energy drops below the threshold after two collisions on average. A possible solution to this problem could be a different relaxation behavior in combination with reflection at the interfaces. If the electrons transfer on average only up to a quarter of their initial energy to a secondary electron the number of average collisions rises for the lower energies. In addition, reflections at the interfaces would guarantee that a total propagation length of four times the mean free path is possible. Changing the energy relaxation scheme is possible but since we have only determined the average amount of energy transferred, such a relaxation scheme lacks of an underlying microscopic picture. Thus, the distribution which is crucial for a better representation of the relaxation process is missing.

Up to now, we have not considered the possibility of elastic scattering events. With elastic scattering events, it is possible to reach longer path lengths and more collisions without changing the energy of the electron. Assuming an energy-independent elastic scattering time which is comparable to the inelastic lifetime of the 2.0 eV hot electrons [113], the measured acceleration cf. Fig. 4.4 would change drastically. While at 2.0 eV the ratio of elastic scattering events would be 1:1, the ratio changes continuously to 4:1 at 0.5 eV. Hence, the total number of scattering events would be much larger than four for the low energy electrons if elastic scattering was present. For such a scenario, the time delay t^* of the low energy electrons would increase linearly in the considered range in Fig. 4.4. Since the data points are far below this limit, the experimental results indicate that the elastic scattering lifetime is much larger than the inelastic lifetime. Consequently, the elastic contributions are negligible in our analysis of the sample. Recalling the single crystalline sample quality, this conclusion is in good agreement with the available sample characterization by a scanning transmission electron microscopy [103, 104] for similar samples.

4.4. Calculation of the electron passage velocity

It is possible to derive the electron passage velocity v_{p} from Eq. (4.5) using the identity

$$v_{\mathrm{F}} = d/t_0, \tag{4.6}$$

where we assume that ballistic electrons propagate predominately orthogonal to the interface and, thus, need the time t_0 to cross a sample of thickness d when propagating

with the Fermi velocity v_F. We define the passage velocity as

$$v_\mathrm{p} = d/t. \tag{4.7}$$

Thus, we assume that passage velocity is given by the ratio of the layer thickness d and the passage time t. The passage velocity reads

$$v_\mathrm{p} = \frac{v_\mathrm{eff} v_\mathrm{F}}{v_\mathrm{eff} + v_\mathrm{F}}. \tag{4.8}$$

Here, we insert Eq. (4.6) and Eq. (4.7) in the definition of the effective velocity $v_\mathrm{eff} = d/t^*$ where $t^* = t - t_0$ is the time delay between the considered electrons and the ballistic electrons. Since v_eff is proportional to $1/t^*$, it is in the range $[0, \infty[$ which might be counter intuitive because the velocity can exceed the Fermi velocity which is the highest possible velocity of the electrons according to our model. The passage velocity is more intuitive since it is in the range $[0, v_\mathrm{F}]$. In the limit $v_\mathrm{eff} \gg v_\mathrm{F}$, the passage velocity is given by

$$v_\mathrm{p} = v_\mathrm{eff} - \frac{v_\mathrm{eff}^2}{v_\mathrm{F}} + \mathcal{O}[v_\mathrm{eff}^3]. \tag{4.9}$$

This limit is of particular importance for the low energy group of Fig. 4.4 because here are the most collisions needed and, therefore, we find here the highest time delay. Due to the definition of the passage velocity, it is clear that ballistic electrons live in the limit $v_\mathrm{eff} \ll v_\mathrm{F}$. From Eq. (4.8), we can calculate the first correction term to the Fermi velocity

$$v_\mathrm{p} = v_\mathrm{F} - \frac{v_\mathrm{F}^2}{v_\mathrm{eff}} + \mathcal{O}[v_\mathrm{eff}^{-2}]. \tag{4.10}$$

The first order correction shows that the group velocity approaches the ballistic velocity with an $-1/v_\mathrm{eff}$ dependence. Figure 4.5 shows the passage velocity as a function of the effective velocity. The effective electron velocity is a quantity which is experimentally easily accessible. However, it is only an intuitive quantity if it is small. That is, if the corresponding electrons have scattered many times. When describing ballistic or almost ballistic electrons that have scattered up to one time, the effective velocity diverges or becomes much larger than the Fermi velocity. The passage velocity provides a more intuitive velocity because it has the Fermi velocity as an upper limit. Figure 4.6 shows the passage velocities for the experimental data from Fig. 4.4 calculated with Eq. (4.8) along with the passage velocities of the simulated trajectories. The simulated passage velocities increase approximately linearly with d_Au. The intermediate (red) and low (blue) energies from the experimental data increase analogue. The high energies (blue) show a different behavior. Their passage velocity increases faster for small d_Au and saturate at the Fermi velocity. Since the electrons with a high energy collide on average less than one time, the deviation to the simulated one collision passage velocity is reasonable.

We remark that the passage velocity depends on the definition of the ballistic velocity, cf. Eq. (4.6). Therefore, it is not possible to derive time zero from the experimental data with the passage velocity. In addition, the passage velocity is only as correct as the assumption of the ballistic passage time. In the next section, we will support the assumption by investigating the injection angles of the ballistic and scattered electrons.

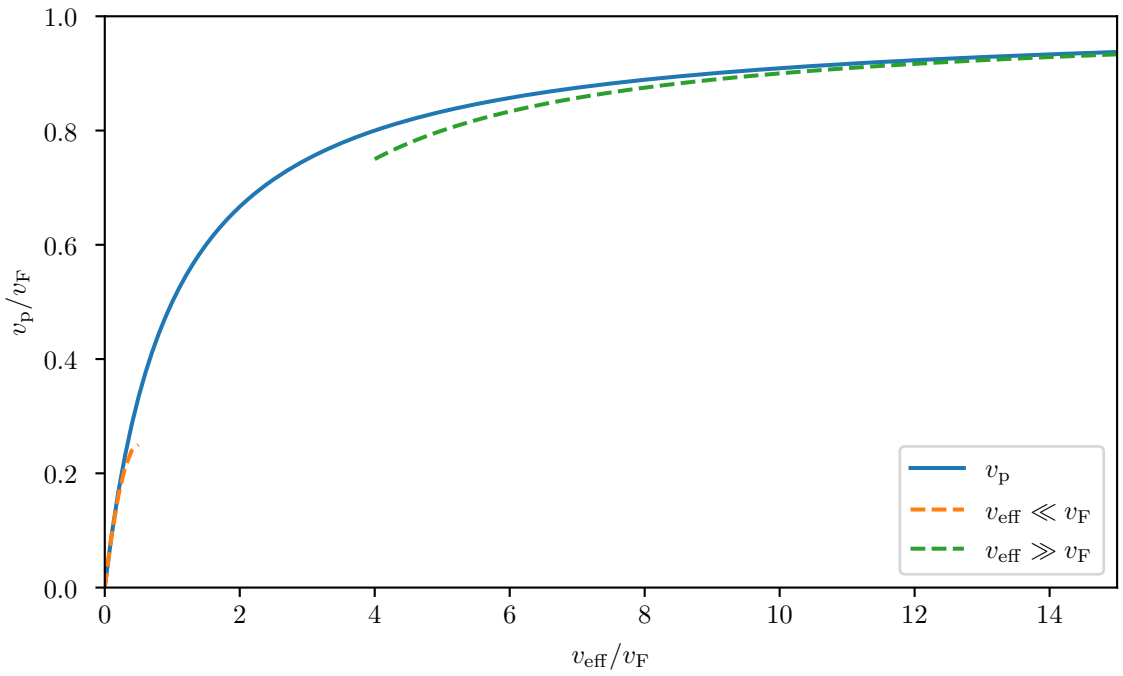

Figure 4.5.: Electron passage velocity as a function of the effective velocity. The dashed lines show the limits $v_{\mathrm{eff}} \gg v_{\mathrm{F}}$ and $v_{\mathrm{eff}} \ll v_{\mathrm{F}}$ with its first nontrivial correction.

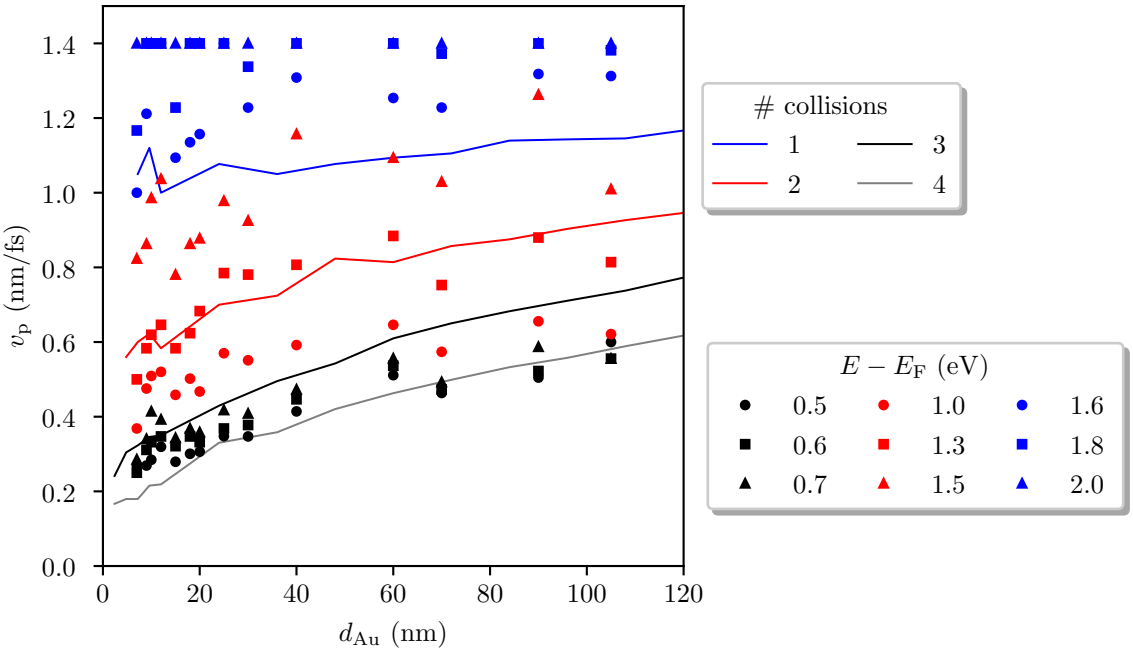

Figure 4.6.: Experimental passage velocity for the given energies in comparison with the passage velocity of the simulated trajectories with different numbers of collisions. The experimental energies are grouped in high (blue), intermediate (red) and low (black), see also Fig. 4.4.

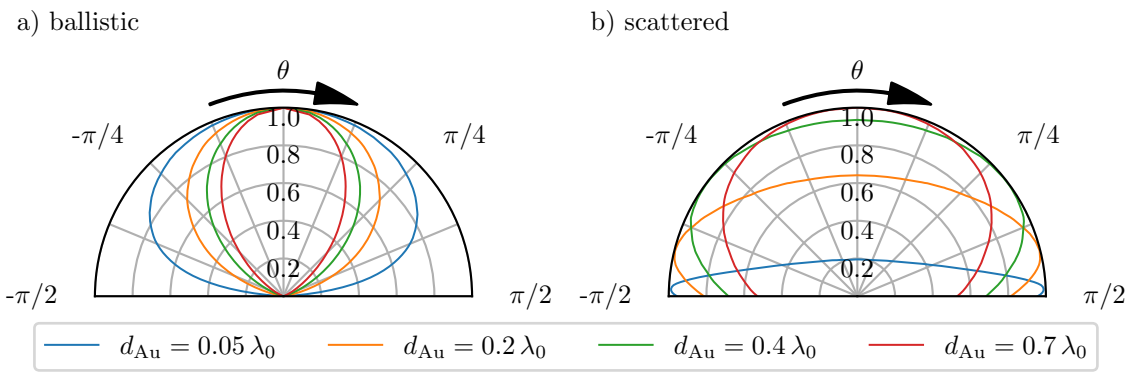

Figure 4.7.: Normalized angular distribution of initial polar angles for a) ballistic and b) scattered electron trajectories for sample thicknesses $d = 0.05\,\lambda_0, 0.2\,\lambda_0, 0.4\,\lambda_0$ and $0.7\,\lambda_0$. An initial angle of $\theta = 0$ corresponds to a propagation parallel to the z-axis. *Adapted from Ref. [9] under Creative Common Attribution 4.0 International license.*

4.5. Angular analysis of the electron injection

From the analysis in Chapter 4.3 and 4.4, we identify superdiffusive electron transport at a final energy below 1.5 eV. Thus, the electrons need to propagate over a distance given by their mean free path. We expect that ballistic and scattered electrons are injected with different angles into the gold layer. For verification, we use again the detailed information given by the simulation. We group the electron trajectories into scattered (superdiffusive) and not scattered (ballistic). In Fig. 4.7, we show the distribution of injection angles θ for ballistic and scattered electrons for four different gold thicknesses d in panel a) and b), respectively. Ballistic electrons propagate always in a narrow cone which is centered around the z-axis. The thicker the sample, the more narrow the cone becomes. In contrast, the scattered electrons need to ensure a path length comparable to the mean free path. Consequently, the electrons need an injection angle almost parallel to the surface normal in very thin samples. With increasing sample thickness the most probable injection angle approaches the z-axis which is reached in Fig. 4.7 b) for the sample thickness $d = 0.7\,\lambda_0$. This behavior explains the observed apparent acceleration of the electrons in both experiment and simulation. Since the scattered electrons have an injection angle parallel to the surface plane, their path is much longer than the ballistic electrons path. Consequently, their effective velocity is much smaller. With increasing gold layer thickness, the absolute value of the injection angle becomes on average smaller resulting in a shorter path. Accordingly, the effective velocity increases as seen in both the experiment [9] and the simulation, see Fig. 4.3. We can extrapolate this analysis to understand the different curvatures in Fig. 4.3 and 4.4. It is simply the case that n scattering events require on average a path length which is equal to n times the mean free path of the electrons. Regarding the passage time this means that the more scattering events occur on the trajectory the longer the electrons need to stay inside the probe. Thus, more collisions are associated with a higher time delay.

For the scattering, we assumed an isotropic distribution of scattering angles which might not be entirely valid in the experiment. The angular dependence, however,

is not affected by applying different scattering schemes. In a thought experiment, we assume a completely different scattering scheme with only forward and backward scattering. We expect that the distribution of initial angles for the ballistic electrons remains unchanged since they are not affected by the new scattering scheme. The scattered electrons, on the other side, still need on average a path length comparable to the mean free path. Therefore, we still expect a similar angular dependence of the scattered electrons. The angular behavior suggests to apply momentum-dependent scattering at buried interfaces for energy selection in electron (or hole) injection across interfaces. A potential design implies electron transmission of high energy electrons along the interface normal and (total) reflection of electrons at larger angles θ.

4.6. Boltzmann equation approach for diffusive electron transport

With our Monte-Carlo simulation, we are able to identify the ballistic and superdiffusive transport regime in the considered energy range by the average number of collisions. However, we are not able to show the transition to the diffusive transport regime. For multiple collisions along the trajectory, the time delay increases linearly. We expect that this trend continuous up to a high gold thickness or rather increases quadratically at a certain point as described by the mean square displacement in a diffusive transport regime, cf. Eq.(2.32). In the following, we discuss a model that combines hot-electron relaxation with diffusive transport. The relaxation is based on the analytic solution of the Boltzmann collision integral by Ref. [12], see Chapter 2.5.2. We expand the relaxation ansatz with diffusive transport by assuming that the distribution function is space dependent. We assume that the total time derivative of the particle distribution f [109] describes a propagation in the diffusive transport regime

$$\dot{f}_\xi = \left(\frac{\partial}{\partial t} - D\frac{\partial^2}{\partial x^2}\right) f_\xi. \tag{4.11}$$

Using this ansatz for Eq. (2.26) does not change the derivation of the relaxation term until Eq. (2.31). With the diffusive ansatz Eq. (2.31) reads

$$\begin{aligned}\tau_0 \left(\frac{\partial}{\partial t} - D\frac{\partial^2}{\partial x^2}\right) \chi(\xi, x, t) = &- \left(1 + \frac{\xi^2}{\pi^2}\right) \chi(\xi, x, t) \\ &+ \frac{3}{\pi^2} \int_{-\infty}^{\infty} d\xi' \chi(\xi', x, t) \frac{\xi - \xi'}{\sinh\left(\frac{\xi - \xi'}{2}\right)},\end{aligned} \tag{4.12}$$

which is a multidimensional integro-differential equation that cannot be solved directly.

To solve the equation, we use a separation ansatz

$$\chi(\xi, x, t) = \chi_\xi(\xi, t)\chi_D(x, t). \tag{4.13}$$

Inserting the ansatz into Eq. (4.12) we find that the differential equation for χ_ξ is given by Eq. (2.31), i.e. the energy relaxation only, when

$$\left(\frac{\partial}{\partial t} - D\frac{\partial^2}{\partial x^2}\right) \chi_D(x, t) = 0. \tag{4.14}$$

Thus the separation ansatz splits the equation into a homogeneous diffusion equation and the equation of the energy relaxation derived by Ref. [12].

The homogeneous diffusion equation is solved by the fundamental solution, cf. Eq. (2.35)

$$\chi_D(x,t) = \frac{1}{\sqrt{4\pi D t}} \int_{-\infty}^{\infty} dx_0 \exp\left[-\frac{(x-x_0)^2}{4Dt}\right] \chi_D(x_0,0). \tag{4.15}$$

The fundamental solution convolutes an arbitrary initial distribution $\chi_D(x_0,0)$ with a time-dependent Gaussian distribution. The standard deviation increases in a square-root fashion over time. The diffusion constant D specifies the strength of the slope. The fundamental solution describes the free evolution of a distribution function. To apply the fundamental solution to the Fe/Au heterostructure, we need to apply boundary conditions. We assume an initial distribution that is symmetric around $x = 0$. To apply the fundamental solution on a boundary at $x = 0$, we mirror the negative half space to the positive half space. Hereby, we assume a total reflection at the Fe/Au interface. The easiest way to implement the mirroring is to multiply the fundamental solution with a factor of two. In principle, it is necessary to mirror the fundamental solution also at $x = d$ where d is the thickness of the sample. Subsequentially, the solution needs to be mirrored again at $x = 0$. Thus, an infinite sum of mirroring processes needs to be applied. Since we focus in the model on ultrafast processes, we can approximate the solution by taking only the first mirroring process at $x = 0$ into account. Thereby, we assume that the hot electrons have reached the stationary state before the second mirroring process comes into play.

4.7. Diffusive transport model

Here, we apply the Boltzmann transport model to a homogeneous one-dimensional sample with thickness d. First, we analyze the time evolution of the collision term neglecting transport effects for different initial excitation schemes. In the next step, we switch on the propagation of electrons and calculate the electron intensity as a function of energy and time. The resulting spectra are compared to the experimental results. Thickness-dependent transport characteristics are analyzed in the last part of this section.

We use Eq. (2.31) to describe the time evolution of the energy relaxation. To solve the equation, we discretize the distribution function $\chi(\xi,t)$ in time and energy. Here, it is important to choose an energy discretization according to the total energy in the system which is determined by the initial distribution. The higher the total energy introduced by the initial excitation, the higher the resolution of the discretization needs to be. The most challenging part of the relaxation calculation is the integration that can only be solved numerically. In principle, it is necessary to sum over the full energy space but it is possible to limit the range $\xi \in [-\xi_{\max}, \xi_{\max}]$. Within the reduced energy range the distribution $\chi(\xi,t)$ must drop to zero for all times t. Otherwise, energy conservation is violated and the calculation becomes unstable. For each time step, the sum has to be evaluated for each energy grid point. Therefore, it has the biggest share

in the calculation costs. The calculation algorithm for the collision term is given by

$$\chi_{i,j+1}(\xi_i, t_{j+1}) = \chi_{ij}(\xi_i, t_j) + \Delta t \left[-\left(1 + \frac{\xi_i^2}{\pi^2}\right) \chi_{ij}(\xi_i, t_j) + \frac{3}{\pi^2} \Delta\xi \sum_{\xi_k=-\xi_{\max}}^{\xi_{\max}} \chi_{ij}(\xi_k.t_j) \frac{\xi_i - \xi_k}{\sinh((\xi_i - \xi_k)/2)} \right], \quad (4.16)$$

where the times t and Δt are chosen in units of $\tau_0 = \frac{2}{\pi^2 K (k_\mathrm{B} T)^2}$.

In the following, we discuss the time evolution of three different excitations or initial distributions. The first distribution is an antisymmetric excitation with an energy $2\,\xi_0$. In this case, electrons are excited from an energy $-\xi_0$ below the Fermi edge to ξ_0. Such an initial distribution is suitable to describe the excitation scheme of a front-pump front-probe measurement where the electrons are excited and probed on the same side of the sample (gold layer). The second distribution describes an continuous excitation where electrons are taken from below the Fermi edge down to an energy $-\xi_0$ and are excited to an energy up to ξ_0. This initial distribution is relevant to describe a measurement scheme where the electrons are pumped and probed on the iron side of the sample, cf. [9, 106]. In the last initial distribution, excited electrons at an energy around $+\xi_0$ are considered. Different from the first scenario there is no counter part below the Fermi edge. The latter scenario is not antisymmetric thus we cannot use Eq. (2.31) as basis for our calculation since we have made the assumption that the distribution χ is antisymmetric. To describe the relaxation process of the injection case properly, we need to go one step back and use Eq. (2.29). The numeric discretization scheme is analogue to Eq. (4.16). The last distribution can be applied to the back-pump front-probe measurement. Here, the electrons are injected into the gold layer in an energy window around 1.7 eV.

Figure 4.8 shows the relaxation process of the above described excitation schemes. The upper right panel shows the initial distribution as a function of energy. At time $t = 0.01\,\tau_\mathrm{e}$, one sees that the high-energy side of the initial peak decays faster than the low energy side in line with Fermi-liquid theory. The energy is transferred to electrons with a lower energy by electron-electron scattering. With increasing time, the electron distribution approaches an excited Fermi sea which is almost reached at $t = 0.9\,\tau_\mathrm{e}$. There are two major differences in the relaxation process of the iron and gold side pumping. Due to the continuous distribution, there are electrons with an energy close to the Fermi energy. Over time, these low-energy electrons scatter with higher energy electrons and gain energy. After the dynamic equilibrium is reached, the two excitation schemes do not differ qualitatively. The final distribution is independent of the initial one and can be approximated by [12]

$$f(t \to \infty, \xi) \sim \xi e^{-\xi^2}. \quad (4.17)$$

The peak position is approximately at $k_\mathrm{B}T$ and the height of the peak is proportional to the total energy introduced via the excitation. The total electron energy of the initial distribution describing a continuous excitation is higher than for the initial distribution where the electrons are excited to a single energy. Therefore, the peak and the temperature of the dynamic equilibrium are higher as indicated by the little shift towards a higher energy in the peak position of the final distribution. The electron

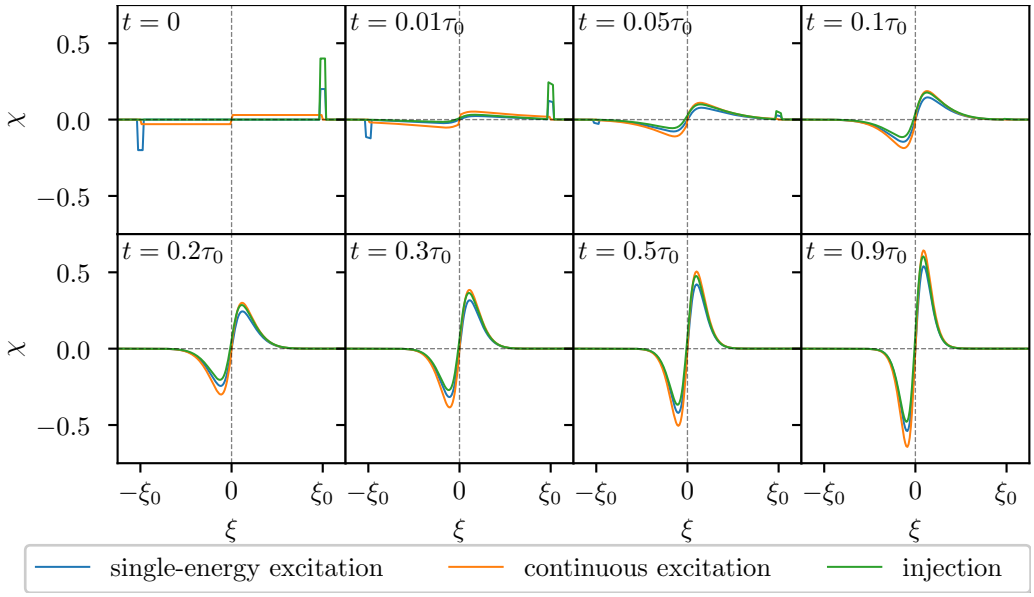

Figure 4.8.: Relaxation process of three different excitation schemes. The relaxation process can be followed by the indicated time stamps in the upper left corner of each panel. Starting at time $t = 0$ in the upper left panel, the electron distributions relax towards an excited Fermi sea which is almost reach at time $t = 0.9\,\tau_0$ in the lower right panel. For simplicity the distribution function of the injection scheme has been renamed to χ.

energy of the excitation to a single energy and the injection of electrons at a certain energy is in both cases the same. Thus, both schemes have an equal temperature after the relaxation process. Due to particle number conservation, the number of electrons above the Fermi edge is in the injection case higher. Therefore, the peak above the Fermi edge is larger than the peak below Fermi energy for the initial distribution describing the injection scenario.

In the next step, we use the diffusive Boltzmann transport equation (4.12) to calculate electron transport in a diffusive regime. For a more realistic model, we use instead of a box function a normal distribution with mean value $\bar{E} = 1.7\,\mathrm{eV}$ and standard deviation $\Delta E = 0.1\,\mathrm{eV}$. Since the energy unit in Eq. (4.12) is $k_\mathrm{B}T$, we assume that the sample has room temperature to convert the energy units. In this case, 1 eV corresponds to approximately $38.67\,k_\mathrm{B}T$.

Figure 4.9 shows the relaxation dynamics after a front pump a) and a back pump b) and c) for two different gold layer thicknesses, respectively. According to Ref. [157] the diffusion coefficient of randomly moving charge carriers in gold is $D = 156\,\mathrm{cm}^2\mathrm{s}$. The relaxation time constant is given by $\tau_0 = 1.2\,\mathrm{ps}$ at room temperature under realistic assumptions [12]. Finally, we find that $\sqrt{D\tau_0} \approx 135\,\mathrm{nm}$ which means that the considered sample thicknesses are comparable the samples used in the experiment. The relaxation itself happens on a slightly faster timescale compared to the experimental result, cf. Fig. 2.9.

The density plots show the normalized electron intensity as a function of energy and time in a diffusive transport regime. The result of front-pump calculation is comparable to the experiment [106] on a qualitative level. There is a prominent feature arising from the initially excited electrons around 1.7 eV. The feature decays exponentially

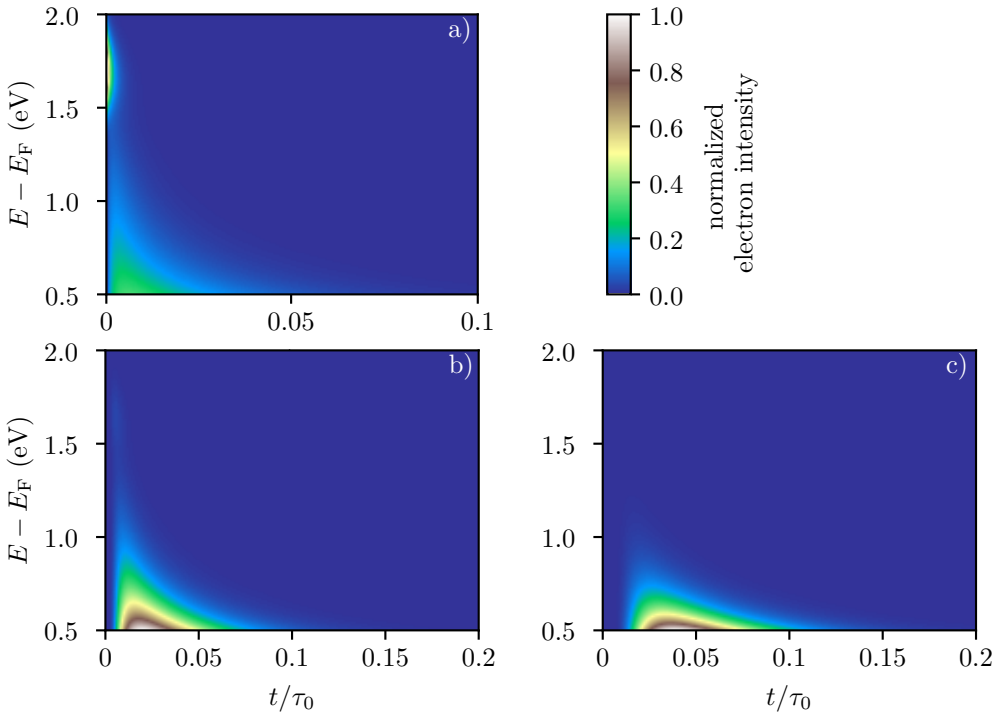

Figure 4.9.: Normalized intensity spectrum after a) a front pump, b) a back pump with sample thickness $d = 0.25\sqrt{D\tau_0}$ and c) a back pump with $d = 0.5\sqrt{D\tau_0}$ as a function of energy and time.

as function of time according to their energy-dependent lifetime, see Eq. (2.30). The second feature is visible below 1 eV. Since it is unlikely that electrons are excited to this energy, the electron intensity rises in the beginning via electron-electron scattering, reaches a maximum and decays afterwards exponentially.

Figure 4.10 shows the electron intensity as a function of time for the depicted energies from Fig. 4.9. The upper panel shows the front-pump case. Here, one can clearly see the difference between both features. The high-energy feature is dominated by an exponential decay while the feature below 1.5 eV shows first a rise in intensity and afterwards an exponential decay. The maxima of the low-energy feature appear the later the lower the energy of the corresponding electrons is. This result clarifies that a shift of the maximum position as a function of energy is not sufficient to prove that transport effects occur in the investigated system.

The calculation of the back-pump case with the thinner gold layer, cf. Fig. 4.9 b), shows only a small intensity at the high-energy feature around 1.7 eV which almost vanishes in the thicker sample cf. Fig. 4.9 c). Different from the front pump scenario, this feature is zero in the beginning and builds up as a function of time. From Fig. 4.10 b) one can see that the electron intensity rises with a smooth shape at all energies, reaches a maximum and decays afterwards. This is in clear contrast to the ballistic simulation, cf. Fig. 4.2, where the ballistic electrons jump to maximum intensity at time $t = d/v_F$. The low-energy feature in Fig. 4.9 b) is comparable to the result from the simulation, cf. Fig. 4.1. As mentioned before, Fig. 4.10 reveals the rise and decay of the intensity for the different energies. In comparison to panel a), the maximum positions have a bigger spacing in between. The spacing becomes even larger when the

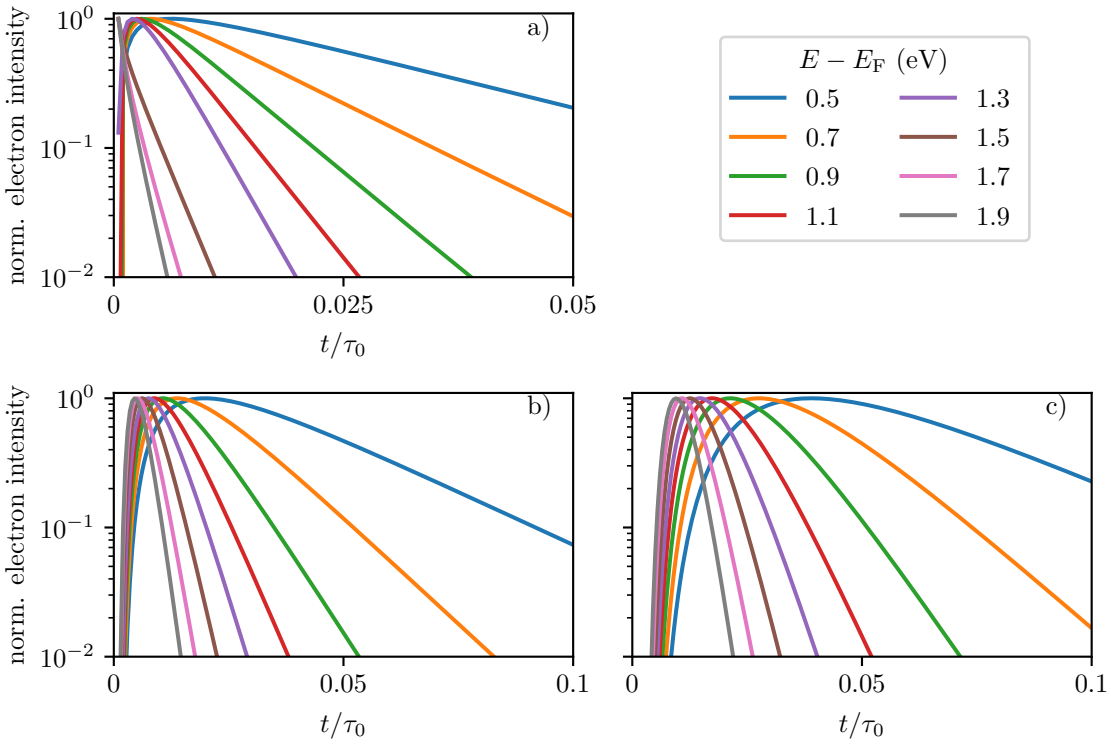

Figure 4.10.: Normalized electron intensity of depicted energies as a function of time in a) front pump set up and back pump set with sample thickness b) $d = 0.25\sqrt{D\tau_e}$ and c) $d = 0.5\sqrt{D\tau_e}$.

gold layer thickness is increased, cf. Fig. 4.10 c). Here, we also see that the position of the highest energy peak appears at later time compared to the thinner sample. Both, the spacing and the delayed appearance of the high-energy peak are part of the transport features we analyze next.

In the back-pump front-probe measurement, the experiment is only sensitive to the time delay between the maximum position. Therefore, we will analyze only this transport effect in the following. In principle, we expect for both that the time delay follows the relation from the mean square displacement, cf. Eq. (2.32). In Figure 4.11, the time delay as a function of sample thickness for the depicted energies is shown. In contrast to Fig. 4.3, the time delay increases faster than linear in the diffusive transport regime as expected. For the evaluation of Fig. 4.3 and Fig. 4.4, we use that all energies and collisions pass through the point (0,0). In the diffusive case, this seems not to be true. The time delay of electrons with an energy below 1.5 eV saturates clearly at a time delay $\Delta t > 0$. For the high-energy electrons, we find zero time delay for small d_{Au} in agreement with the front pump excitation scheme, cf. Fig. 4.10 a). Since the energies below 1.5 eV need to be populated via electron-electron scattering first, there is always a time delay present. In the simulation, this is different since there is always a finite probability to have n scattering events when the gold layer thickness goes to zero.

The diffusive transport calculation supports our assumption of ballistic and superdiffusive electron transport for the experiment. While the analysis of intensity spectra at a fixed gold layer thickness shows comparable results to the experiment, the increasing time delay as a function of gold layer thickness shows a clearly different curvature. As

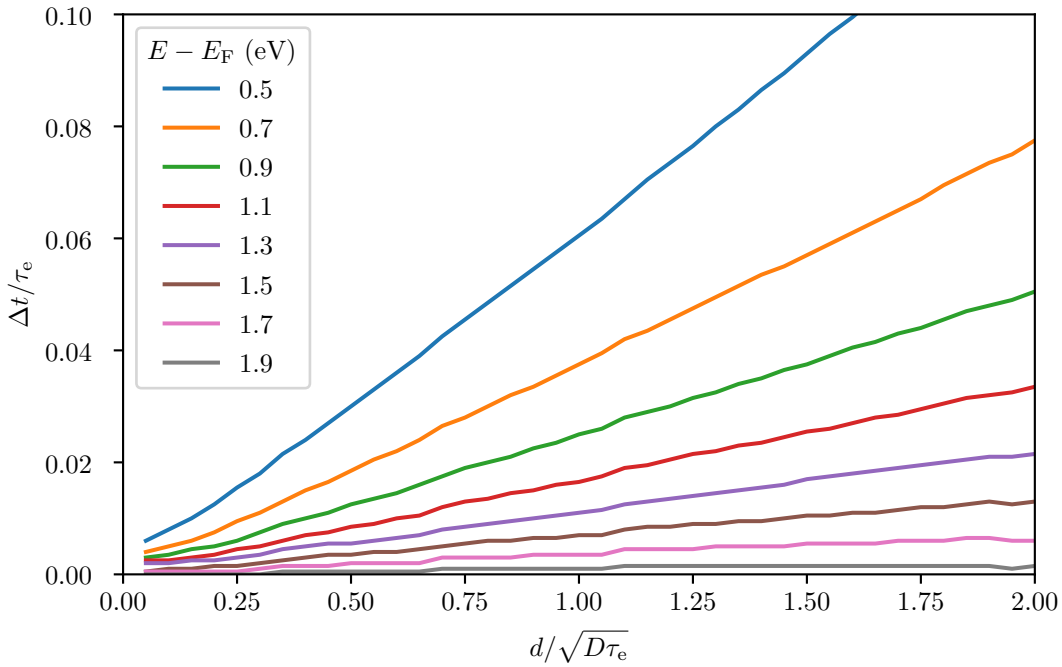

Figure 4.11.: Time delay between the peak position of the 2.0 eV and the indicated energy as a function of sample thickness.

expected, we found the quadratically increasing time delay for the diffusive calculation while in the experiment the time delay appears to be in a sublinear fashion. From the simulation results, we expected that the linear trend found for small d_{Au} will continue over the considered range. This is also supported by our diffusive calculation since the quadratic dependence is only distinguishable from a linear one when sample thicknesses which are twice as large as used in the experiment are taken into account.

4.8. Transition to diffusive transport

In the experiment, we find electrons that are detected with the original injection energy have propagate in a ballistic transport regime. Lower energies need to be populated first which requires a certain amount of electron-electron scattering events. The average number of electron-electron scattering events is for all energies considered in the experiment below the diffusive limit. Nevertheless, there must be a transition from the superdiffusive to the diffusive regime when the number of scattering events increases. When we extrapolate the time delay as a function of gold layer thickness for trajectories with more than four collisions in Fig. 4.4, we get a linear function for small thicknesses. We expect that at a certain number of collisions the shape of the function changes from sublinear to superlinear which refers to a change from the superdiffusive to the diffusive transport regime.

To determine an approximate number of collisions that sets the transition between the diffusive Boltzmann model and the trajectory based simulation, we set up a toy model. As a start, we consider that an electron propagates always over a constant distance λ before it collides. In the next step, we consider a one-dimensional slab of length $L = (n-1)\lambda$ with $n \in \mathbb{N}^{>1}$. The slab has an injection point at $z = 0$ where the

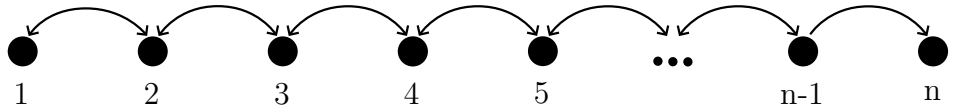

Figure 4.12.: Sketch of the one-dimensional toy model to determine the number of collisions necessary to identify diffusive transport. The slab ranges over all black spots. At position 1 the electrons are injected into the sample and at position n the electrons are extracted. At each collision point in between, the electrons can either propagate forward of backward with equal probability as indicated by the arrows.

electron always moves to the right and an extraction point at $z = (n-1)\lambda$ which serves as an absorbing state and $n-2$ collision points in between. At each collision point, the electron can move in both direction with equal probability. Thus, the electron randomly walks across the sample. The system is sketched in Fig. 4.12. The transport in such a model is per definition diffusive. For $n = 2$ the transport regime cannot be distinguished from a ballistic transport. The question is how long the slab needs to be and how many collisions are necessary to identify a diffusive behavior. Therefore, we need an algorithm to calculate the probability of the electron to reach the extraction point at position n after t jumps or, equivalently, $t-1$ collisions. To describe the hopping between the sites, we define the transition matrix $\mathbf{M}$ with the size $n \times n$ where the only nonzero elements are on the subdiagonal and superdiagonal. All entries are $1/2$ except for the element $m_{12} = 1$ and $m_{n-1,n} = 0$ for the injection and absorbing state, respectively. The matrix is given by

$$M = \begin{bmatrix} 0 & 1 & 0 & \cdots & \cdots & 0 \\ 1/2 & 0 & 1/2 & \ddots & \ddots & \vdots \\ 0 & 1/2 & \ddots & \ddots & \ddots & \vdots \\ \vdots & \ddots & \ddots & \ddots & 1/2 & 0 \\ \vdots & \ddots & \ddots & 1/2 & 0 & 1/2 \\ 0 & \cdots & \cdots & 0 & 0 & 0 \end{bmatrix}. \tag{4.18}$$

We are interested in the probability to reach the absorption point n after t jumps which is calculated by the iteration

$$\mathbf{P}_{t+1} = \mathbf{M} \cdot \mathbf{P}_t. \tag{4.19}$$

Here, $\mathbf{P}_t$ is the probability vector of length n after t jumps where each element gives the probability to find the electron at the corresponding site. The iteration is started with the injection vector

$$\mathbf{P}_0 = (1, 0, 0, 0, ...)^T, \tag{4.20}$$

which has a one in the first entry and zeros in all other entries.

Figure 4.13 shows the normalized electron intensity as a function of jumps t. One can clearly see how a maximum builds up and decays afterwards. Similar to the analysis above, it is possible to determine the relative distance between the fastest electrons and the maximum position for different system sizes. The result is depicted in Fig. 4.14.

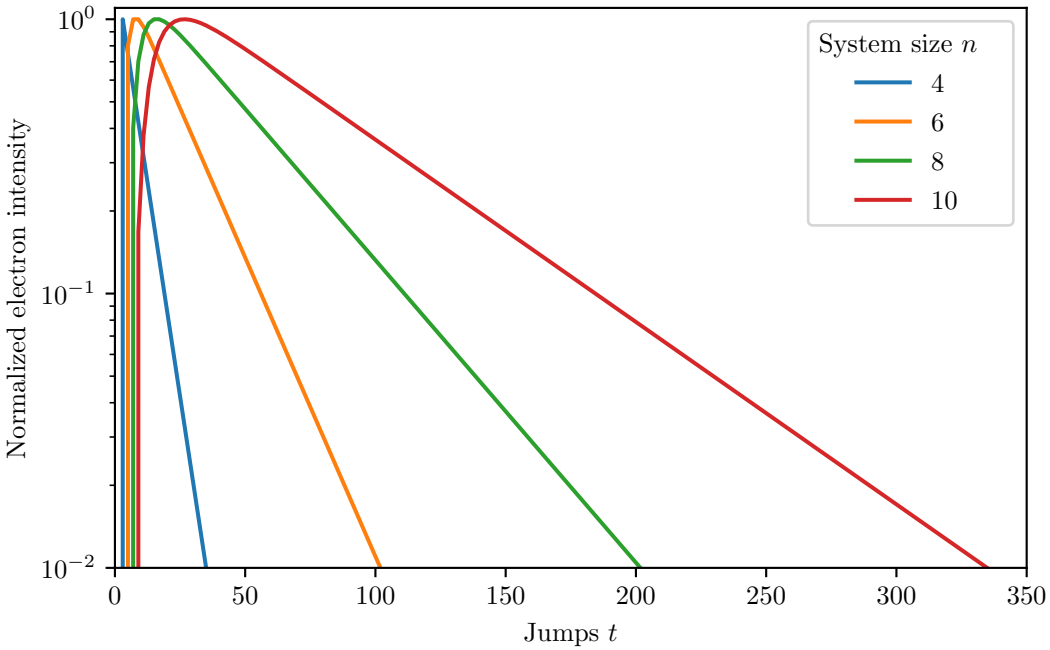

Figure 4.13.: Normalized electron intensity at the absorption site as a function of jumps t for different system sizes n.

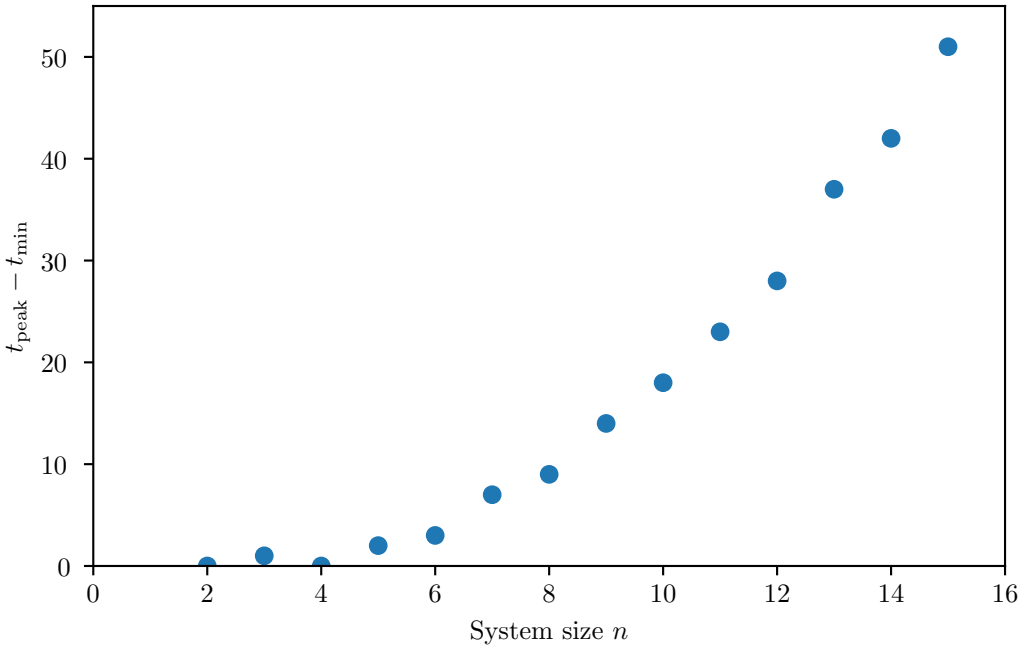

Figure 4.14.: Difference between the most probable number of jumps and the minimum number of jumps as a function of system size n. The diffusive characteristic of the transport is clearly visible in the quadratic shape of the function. The small offsets between an even and odd system size is an artifact of the discretization.

The curve shows the expected quadratic dependence for diffusive transport. We can use Fig. 4.14 to give a rough estimation of the required system size and number of collisions that is required to identify diffusive transport in the trajectory-based simulation. First, we need to decide at which system size it is possible to distinguish between a linear function and a parabola. We assume from the figure that this point is approximately at a system size of ten which corresponds to a sample length of $L = 9\,\lambda$. At such a size, the most probable number of jumps is approximately 30 jumps since at least 9 jumps are required by the fastest electrons. To conclude, there are also approximately 30 collisions necessary to distinguish diffusive and superdiffusive transport clearly.

In three dimension, the necessary sample thickness might be smaller. Nevertheless, we expect that the number of collisions is in the correct order of magnitude. Both results from experiment and simulation are far below our estimate of diffusive transport. Therefore, we do not find any signature of diffusive transport with the simulation in the current set up. Possibly, an analysis at energies close to the Fermi energy may reveal a diffusive transport regime in both experiment and simulation. However, the calculation costs for the trajectory-based model increases when we consider a threshold energy closer to the Fermi energy since more electron paths need to be followed. The Boltzmann calculation is suited best for transport with electrons close to the Fermi edge and show clearly the diffusive behavior that has been verified by the estimation above.

4.9. Summary

In this chapter, we have introduced two relaxation and transport models for photo-excited electrons that are capable of analyzing possible ballistic, superdiffusive and diffusive transport features. Both models have been used to interpret the results from Refs. [9, 105, 106]. The Monte-Carlo simulation combines a random-walk transport with a uniformly distributed energy exchange between electrons. In the simulation, the trajectories of the electrons are tracked and information about the number of scattering events, the injection angle, the total path length as well as the final electron energy are extracted. The energy window in which the electrons are injected into the gold layer has been chosen as indicated by the experimental results as well as by a complementary DFT study of the heterostructure. The electronic lifetimes have been chosen such that they match with the experimentally determined lifetimes in bulk gold in the considered energy range. A comparison of our simulated electron intensity and the experimentally determined two-photon photoelectron emission intensity shows a qualitative agreement.

For both, the simulation and the experiment, the effective velocity has been analyzed as a function of gold layer thickness. The effective velocity is given by the ratio of gold layer thickness and the time delay between ballistic and scattered electrons. In both cases, we have found a sublinearly increasing effective electron velocity. Using the detailed information from the simulation, it has been possible to link this behavior to the average number of collisions on the trajectories. With the analysis, it has been possible to identify high-energy electrons as ballistic and low-energy electrons as superdiffusive. In addition to the effective velocity, the passage velocity has been introduced as the ratio of the gold layer thickness and the real propagation time of the electrons. The passage velocity provides a more intuitive velocity that appears in the

system. It is linearly increasing for the low-energy electrons while it saturates for the high-energy electrons at the Fermi velocity indicating their ballistic nature.

An angular analysis of the injection pattern has been used to explain the apparent acceleration of the electrons with increasing sample thickness. Here, the injection angles of the simulated trajectories have been analyzed for scattered and ballistic electrons. The ballistic electrons are injected predominantly orthogonally to the interface in a narrow cone. The opening angle of the cone decreases with increasing sample thickness. In contrast, the scattered electrons are injected almost parallely to the interface for thin sample. With increasing sample thickness, the predominant injection angle becomes smaller and electrons that scatter are also injected orthogonally to the interface for the largest sample thickness.

The second model describes diffusive electron transport with an energy relaxation according the Boltzmann equation. Here, we have expanded the analytic solution by Ref. [12] with a diffusive transport model. First, the relaxation for the initial scenarios which are excitation from one energy below to one energy above, continuous excitation and injection in a certain energy window has been discussed. Afterwards, the influence of the diffusive transport has been analyzed. The diffusive nature of the transport changes the dependence of the time delay between scattered and ballistic electrons as a function of gold layer thickness. For diffusive transport, we have found a quadratic dependence of the time delay as expected.

Finally, we have shown how many collisions on the trajectory are necessary to distinguish the superdiffusive and the diffusive transport regime in the thickness-dependent analysis of the trajectory-based simulation. For that, we have set up a one-dimensional random-walk toy model where an electron distribution is inserted at the one side and measured at the end of the chain. The results reveal that the number of scattering events to distinguish both regimes is around 30. In the considered energy range of the Monte-Carlo simulation, the number of collisions is far below this limit. Hence, there is no diffusive transport in this range. Closer to the Fermi edge, the number of collisions could be in the right order of magnitude to identify diffusive transport.

5. Conclusions

In nanoscale conductors, several transport phenomena can be studied. The charge carrier dynamics are the result of a nonequilibrium condition induced, for example, by a strong nonlinear excitation leading to a charge carrier distribution far away from the ground state Fermi distribution. The specific relaxation of the system is influenced by the various physical effects present in the system. Possible effects include Coulomb and spin interactions as well as quantization and superconducting correlations. Rich transport and relaxation dynamics occurs in systems where different physical effects interplay.

In this thesis, we have studied two particular examples of nonequilibrium nanoscale transport in the time domain. The first example is the pair-amplitude dynamics in a strongly-coupled superconductor-quantum dot hybrid. The pair amplitude is connected to the Cooper pairs. Hence, we have focused on the subgap physics and have, therefore, chosen to describe the dynamics in the infinite-gap limit. In this limit, we have been able to describe the tunneling between the superconductors and the quantum dot exactly by introducing an effective Hamiltonian that hybridizes quantum dot and superconductors in the strong-coupling regime. In addition, the system is coupled weakly to a normal conductor. With a real-time diagrammatic approach, we have set up a master equation to calculate the dynamics of the quantum dot. Due to the weak coupling to the normal conductor, we have had to consider only first-order diagrams in the coupling to the normal conductor. We have formulated the master equation in the pseudospin basis to get a physically intuitive form to interpret the dynamics of the quantum dot system. In this basis, the length of the pseudospin in the x-y plane gives the absolute value of the pair amplitude. In addition, the pseudospin components $\mathbf{I}_x$ and $\mathbf{I}_y$ are experimentally accessible by measuring the Josephson and Andreev currents in the hybrid structure.

The focus of our investigation of the superconductor-quantum dot hybrid has relied on the nonequilibrium pair-amplitude dynamics. First, we have considered the quantum dot in a quenched state by applying a gate voltage. We have derived an analytic solution for the Bloch-type master equation to calculate the dynamics exactly at any time. When setting the gate voltage close to the particle-hole symmetric point, rich oscillation and exponential relaxation dynamics develop as a function of time. With the help of the pseudospin, we have interpreted the oscillation of the pair amplitude as a rotation of the pseudospin in the exchange field. The exchange field can be manipulated by the phase difference of the superconductors and the gate voltage applied on the quantum dot. Hence, it is possible to control the pair-amplitude oscillation experimentally. The relaxation of the pair amplitude arises from the dissipative coupling to the normal conductor and is therefore determined by the coupling strength to the normal conductor only. The advantage of this setup is that the relaxation and oscillation of the pair amplitude occur on different timescales. Therefore, it is possible to probe rich dynamics in such a system.

This result is in strong contrast to a previous work [78]. Here, the superconductors are weakly coupled to the quantum dot. In this case, it is not possible to take only the subgap physics into account. Here, the quasiparticles with an energy above the superconducting gap play an important role for the dynamics. The quasiparticles provide an additional dissipative channel for the pair amplitude. The dissipation rate of the pair amplitude in the weak coupling limit is an order of magnitude higher than the oscillation frequency. Therefore, the oscillation has not been visible by quenching the system. The only possibility to find Higgs-like pair-amplitude dynamics is to apply specific driving schemes to the system.

Furthermore, we have discussed two driving schemes to continuously excite pair-amplitude dynamics on the quantum dot. In the adiabatic limit, the dynamics of the pair amplitude has been derived from the stationary solution of the master equation. When the Fermi energy of the normal conductor crosses an Andreev bound state energy, a rapid change of the pair amplitude is possible. Here, the dot occupation changes from a superposition which allows pair-amplitude dynamics to an odd occupation where the pair amplitude is suppressed. By exploiting these rapid transition, an oscillation of the pair amplitude can be excited when driving the Fermi energy across the Andreev bound state energy. Further promising driving parameters are close to the particle-hole symmetric points which give rise to pronounced pair-amplitude dynamics under driving either the phase difference or the level detuning.

In the fast driving limit, we have approximated the dynamics analytically by a Fourier ansatz. We have found that the zeroth and its neighboring Fourier components are sufficient to describe the resulting pair-amplitude dynamics. For strong coupling between the superconductors and the quantum dot the pair amplitude is able to follow the fast external driving up to high frequencies. The ratio between the coupling strength to the superconductors and the level detuning determines the scaling of the pair amplitude with increasing frequency. For a larger ratio, we have found a larger amplitude with increasing frequency.

Our second example of nonequilibrium nanoscale transport is motivated by recent experiments on a Fe/Au heterostructure which have revealed an intriguing transport effect. It seems that the electrons cross the sample the faster the thicker the gold layer is. To understand this apparent acceleration, we have modeled the transport and relaxation dynamics in the Fe/Au heterostructure by a trajectory-based Monte-Carlo simulation. Here, we have substituted the excitation in the Fe layer by the pump laser and the subsequent injection of charge carriers across the Fe/Au interface by assuming that electrons start at a certain energy above the Fermi energy in the Au layer. Hence, we have focused on the dynamics inside the Au layer only. We have assumed that the electrons are injected and scattered isotropically. Between the scattering events, the electrons propagate quasiballistically with Fermi velocity. When the electrons reach the sample surface, they are absorbed. Regarding the energy, we have assumed that an electron transfers a uniformly distributed random amount of energy to a secondary electron. The secondary electron has been included to the simulation as well. The analysis of the energy and time dependence has required the detailed information of the simulation regarding the injection angle, the number of collision and the total path length i.e. the passage time.

In a first step, we have compared the electron intensity as a function of energy and time to the experimentally determined analogue. Like in the experiment, we have found

two distinct features in the intensity. First, there is a high-energy feature of electrons with their original injection energy that cross the sample ballistically. Ballistic electrons move through the sample on a path which is predominantly parallel to the interface normal. Assuming that all electrons move with the same velocity, the Fermi velocity, the ballistic electrons are the first electrons that are detected at the front side of the sample. Therefore, ballistic electrons have been used as reference to calculate the time delay in the experiment since it has not been possible to determine the time when the pump pulse excited the electrons in the system. The high-energy feature looses intensity with increasing Au thickness due to a higher scattering probability with increasing path length. The second feature arises from scattered electrons below the injection energy. Electrons have not been injected at this energy. Thus, these electrons must have undergone at least one inelastic scattering event on their path to be detected at this energy. There is a time delay between the maximum intensity of the ballistic electron feature and the maximum of the scattered electrons because a finite time is required in which the energy is populated due to electron-electron scattering. There is an excellent qualitative agreement between the simulated data and the experiment.

Since the absolute time the electrons need to propagate through the sample is not experimentally accessible, the transport regimes cannot be identified in the experimental data directly. During this thesis, we have discussed another scheme to determine the transport regime. As it has already been found in the experiment, the time delay of the low-energy feature increases sublinear as a function of Au thickness. Thus, the effective velocity of the scattered electron crossing the sample increases with increasing sample thickness. By analyzing the simulated data, we have connected the apparent acceleration to the number of scattering events. The acceleration is due to the fact that scattered electrons need on average a path which is comparable to the mean free path to ensure scattering. If the Au layer is much smaller than this path length the passage time of the scattered electrons is increased compared to the ballistic electrons. With decreasing difference between the minimum path length and the Au thickness, the time delay rises slower resulting in an apparent acceleration.

We have found that the more collisions occur on a trajectory, the longer the trajectory needs to be. Furthermore, assuming that the number of collisions to reach a certain energy is the larger the lower the energy, we have concluded that the lower the electron energy the larger is the time delay. Since the number of collisions to reach a certain energy is approximately independent of the gold layer thickness, the time delay as a function of thickness increases faster the lower the electron energy. A comparison of the measured energies with the simulated trajectories for a certain number of collisions has revealed the different transport regimes. Electrons with energies close to the injection energy scatter on average less than one time and propagate therefore ballistically. Electrons with an energy below the injection energy scatter at least one time and cross the sample in a superdiffusive transport regime. With the simulation, we have been able to reveal the single scattering events in the Fe/Au heterostructure.

We have verified our assumption on the increased path of scattered electrons by analyzing the injection angle of the electrons. An injection parallel to the surface normal is the most probable injection angle for ballistic electrons. With increasing sample thickness, the injection cone of the ballistic electrons becomes more narrow. For a small Au thickness, the injection pattern of the scattered electrons is different from ballistic electrons. The maximum intensity occurs at an injection almost parallel to the sur-

face normal. With increasing sample thickness, the maximum intensity shifts towards an injection parallel to the surface normal. This supports our interpretation that the apparent acceleration is due to more direct trajectories of the scattered electrons with increasing Au thickness.

With the simulation, it has been possible to show the transport features of ballistic and superdiffusive transport. To complete our understanding of photoexcited electron transport in Fe/Au, we have addressed the diffusive transport regime by a Boltzmann transport model. Hereby, we have extended a previous work [12] where the relaxation dynamics of an electronic system via electron-electron scattering with the Boltzmann equation has been calculated analytically. With a separation ansatz, we have solved the time evolution of an excited electron pulse as a function of space and energy. The solution of the diffusive propagation is given by the fundamental solution of the diffusion equation.

In analogy to the simulation, we have calculated the electron intensity as a function of energy and time. The dependence of the time delay as a function of the Au thickness shows a significantly different behavior in comparison with the result obtained by the simulation. For an underlying diffusive transport, the time delay increases faster than linear. Since the experimental data showed a sublinearly increasing time delay the diffusive calculation has underlined that the transport regime in the experiment is superdiffusive or ballistic.

According to our simulation, the number of scattering events on a trajectory determines the transport regime. There is a transition from the ballistic transport regime with less then one collision over superdiffusive with a few collisions to diffusive with multiple collisions. With the trajectory-based simulation we have been able to determine the transition from the ballistic to the superdiffusive transport regime. The simulation results show also a hint how the transition to the diffusive regime can be determined. There is a linearly increasing time delay as a function of gold layer thickness. The more collisions occur, the thicker the gold layer needs to be to identify the superdiffusive regime. With more scattering events, the diffusive regime would appear as a linearly increasing time delay that changes to a quadratic function with increasing gold layer thickness.

To determine the necessary number of scattering events we have set up a simple one-dimensional hopping model. We have found that the necessary number of scattering events to identify the diffusive regime is a few dozen. Hence, for the considered energy range in our simulation, there has been no diffusion visible. From the analysis, we have concluded that the diffusive transport regime occurs for electrons close to the Fermi energy. It is challenging to simulate the transport close to the Fermi energy with our trajectory-based model since the calculation costs increases rapidly when the threshold energy where electrons are discarded decreases. To simulate the transport near the Fermi level and to find the diffusive transport, a new random walk model optimized for the transport near the Fermi level is required.

Both analyzed nonequilibrium transport models pave the way for further analysis. The superconductor-quantum dot hybrid promises a multifaceted playground to study quantum transport effects that are connected to the collective excitation in bulk superconductors. Since the pair-amplitude dynamics is accessible via the Andreev and Josephson current, it possible to measure the dynamics with modern experimental setups. The analysis of ultrafast transport and relaxation processes opens new insights

to the occurring dynamics. It is a promising tool to support experimental results with a theoretical method to determine the transport regimes. Most certainly, the method can be extended to other systems with appropriate modifications. A two-dimensional metal film could be a good candidate for further testing our model. Another promising sample could be a multilayer system that consists of many gold and iron layers. The simulation could be used to model the transport within each layer. Together with a hopping model that covers the transition between the layers a full theoretical description for the transport in the system could be obtained.

Appendix A.

Calculation of real-time diagrams

Here, we show the calculation of four diagrams, see Fig. A.1 that represents all basic example calculations of the diagrams. The rules to derive the rates are given in Chapter 3.2. We remark that one diagram does not represent a complete rate from the rate matrix but only one contribution to the corresponding rate.

During the calculation we will find integrals of the form

$$\int_{-\infty}^{\infty} d\omega \frac{f^{\pm}(\omega)}{x-\omega+i0^{+}(-1)^{j}}, \tag{A.1}$$

with $j \in \{0,1\}$. We can split the integral into a real and imaginary part

$$\int_{-\infty}^{\infty} d\omega \frac{f^{\pm}(\omega)}{x-\omega+i0^{+}(-1)^{j}} = -\phi^{\pm}(x) - i\pi f^{\pm}(x)(-1)^{j}, \tag{A.2}$$

with

$$\phi^{\pm}(x) = \fint d\omega \frac{f^{\pm}(\omega)}{\omega - x} = \mp \ln\left(\frac{E_{\mathrm{C}}}{2\pi k_{\mathrm{B}}T}\right) \pm \mathrm{Re}\left[\psi\left(\frac{1}{2} + i\frac{x-\mu}{2\pi k_{\mathrm{B}}T}\right)\right]. \tag{A.3}$$

Here, we used the Cauchy principal value integral which can be solved by introducing a Lorentzian cutoff with cutoff energy E_{C}, see Ref. [158] for details. When summing up all diagrams for one rate the first term of Eq. (A.3) cancels for our system. In the diagrams we calculate below, the first term is part of the result.

$W^{\uparrow+}_{\uparrow+}$

The diagram is one of four diagrams that contribute to the rate $W^{\uparrow+}_{\uparrow+}$. In the given diagram, the dot starts in the + state. One $\downarrow$-electron tunnels from the upper Keldysh branch to the lower. It is also possible that the $\downarrow$-electron tunnels from the lower to

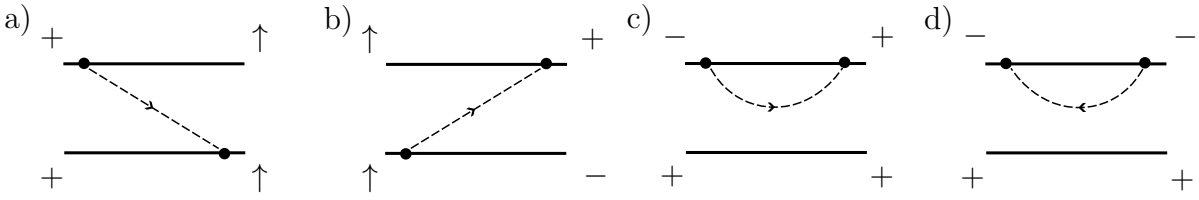

Figure A.1.: Examples of first order diagrams from the Keldysh contour contributing to the rates a) $W^{\uparrow+}_{\uparrow+}$, b) $W^{+\uparrow}_{-\uparrow}$, c) W^{+-}_{++} and d) W^{--}_{++}.

the upper branch or that a ↑-electron tunnels from the lower to upper branch or vice versa. In the case of an ↑-electron tunnel event, the tunnel line goes from the lower left corner to the upper right corner. These are all diagrams that need to be drawn according to the first rule.

For the second rule, we need to identify the left- and right-going energies. The only left going energy is E_+ on the lower branch. The tunneling line and the upper branch is right-going. Here, we need to account for the energies ω and ϵ, respectively. According to the second rule, we find

$$\frac{1}{E_+ - \epsilon - \omega + i0^+}. \tag{A.4}$$

The tunneling line goes forward with respect to the time on the Keldysh contour. Therefore, we need to assign a factor $\frac{1}{2\pi}\Gamma_\mathrm{N} f^-(\omega)$. Thus, we find according to the third rule

$$\frac{1}{2\pi}\Gamma_\mathrm{N} f^-(\omega)\frac{1}{E_+ - \epsilon - \omega + i0^+}. \tag{A.5}$$

For the fourth rule, we focus on the vertices on the Keldysh contour. The vertex on the upper branch connects the state $|+\rangle$ with $|\uparrow\rangle$ by tunneling of an $\downarrow$ electron. We assign for this vertex the factor $\sqrt{1+\frac{\delta}{2\epsilon_\mathrm{A}}}/\sqrt{2}$. The same factor needs to be accounted for the other vertex which describes the same on the lower branch. Hence, according the fourth rule we find

$$\frac{1}{4\pi}\Gamma_\mathrm{N}\left(1+\frac{\delta}{2\epsilon_\mathrm{A}}\right) f^-(\omega)\frac{1}{E_+ - \epsilon - \omega + i0^+}. \tag{A.6}$$

According to rule five, we assign a prefactor $-i$ and -1 for the vertex on the lower propagator. Furthermore, the upper bullet has an outgoing tunnel line and ends in the state $|\uparrow\rangle$ and the lower bullet has an incoming tunnel line starting and starts in the state $|\uparrow\rangle$. Hence, we need to assign -1 two more times

$$\frac{i}{4\pi}\Gamma_\mathrm{N}\left(1+\frac{\delta}{2\epsilon_\mathrm{A}}\right) f^-(\omega)\frac{1}{E_+ - \epsilon - \omega + i0^+}. \tag{A.7}$$

In the final step, we need to integrate over ω the diagram results to

$$\frac{i}{4\pi}\Gamma_\mathrm{N}\left(1+\frac{\delta}{2\epsilon_\mathrm{A}}\right)\int_{-\infty}^{\infty} d\omega f^-(\omega)\frac{1}{E_+ - \epsilon - \omega + i0^+}. \tag{A.8}$$

After solving the integral, we find

$$\frac{i\Gamma_\mathrm{N}}{4\pi}\left(1+\frac{\delta}{2\epsilon_\mathrm{A}}\right)\left[-\phi^-(E_+ - \epsilon) - i\pi f^-(E_+ - \epsilon)\right]. \tag{A.9}$$

$W^{+\uparrow}_{-\uparrow}$

The diagram is one of four diagrams that contribute to the rate $W^{+\uparrow}_{-\uparrow}$. In the given diagram, the dot starts in a spin-up state and switch to a superposition of a + and −

state by a tunneling of a spin-down electron from the lower to the upper branch of the Keldysh contour. The other diagrams that contribute to the rate are drawn analogue to the description above. A new aspect compared to the diagram before is that the tunneling line goes backward in time.

As a start, we identify the left- and right-going energies. Only the energy E_- on the lower branch is left going. The tunnel energy ω and the energy on the upper branch ϵ is right going. Thus, we have

$$\frac{1}{E_- - \epsilon - \omega + i0^+}. \tag{A.10}$$

Different from above, the tunneling line goes backward with respect to the time. Therefore we assign

$$\frac{1}{2\pi}\Gamma_\mathrm{N} f^+(\omega)\frac{1}{E_- - \epsilon - \omega + i0^+}, \tag{A.11}$$

according to the third rule. The upper vertex connects the states $|\uparrow\rangle$ with $|+\rangle$ by the tunneling of a spin-down electron. Here, we assign a factor $\sqrt{1+\frac{\delta}{2\epsilon_\mathrm{A}}}/\sqrt{2}$. The lower bullet connects the states $|-\rangle$ with $|\uparrow\rangle$ under tunneling of the same electron. Thus we assign $\sqrt{1-\frac{\delta}{2\epsilon_\mathrm{A}}}/\sqrt{2}$. Thus, with the fourth rule we find

$$\frac{1}{4\pi}\Gamma_\mathrm{N}\sqrt{1-\frac{\delta^2}{4\epsilon_\mathrm{A}^2}} f^+(\omega)\frac{1}{E_- - \epsilon - \omega + i0^+}. \tag{A.12}$$

The next step is assigning the global prefactor $-i$ and a -1 for the bullet on the lower propagator. The upper vertex starts in the state $|\uparrow\rangle$ with an incoming tunnel line and the lower vertex ends in the state $|\uparrow\rangle$. Hence, we assign for each vertex a -1. After integration over all energies, we find for the diagram

$$\frac{i}{4\pi}\Gamma_\mathrm{N}\sqrt{1-\frac{\delta^2}{4\epsilon_\mathrm{A}^2}}\int_{-\infty}^{\infty} d\omega \frac{f^+(\omega)}{E_- - \epsilon - \omega + i0^+}, \tag{A.13}$$

which yields

$$\frac{i}{4\pi}\Gamma_\mathrm{N}\sqrt{1-\frac{\delta^2}{4\epsilon_\mathrm{A}^2}}\left[-\phi^+(E_- - \epsilon) - i\pi f^+(E_- - \epsilon)\right]. \tag{A.14}$$

W^{+-}_{++}

The diagram is one of two diagrams contributing to the rate W^{+-}_{++}. In the other diagram, the tunneling line goes in the opposite direction. In both diagrams, the dot starts in a superposition state which is described by the density matrix element ρ^-_+. By the tunneling of an electron, the dot changes to the $|+\rangle$ state. The new aspect compared to the diagrams above is that the diagram represents two equivalent diagrams since either a spin-up or spin-down electron can tunnel. Nevertheless, for both spin directions the calculation is the same. Thus, we account for two spins by an additional factor of two.

In the given diagram, there is one left-going energy E_+ and two right-going ϵ and ω. According to the second rule, we start with

$$\frac{2}{E_+ - \epsilon - \omega + i0^+}. \tag{A.15}$$

The tunneling line goes in forward direction. Hence, we find

$$\frac{1}{\pi}\Gamma_\mathrm{N} f^-(\omega)\frac{1}{E_+ - \epsilon - \omega + i0^+}. \tag{A.16}$$

The left vertex connects the state $|-\rangle$ with the state $|\sigma\rangle$ by tunneling of an electron with σ'. Here, σ' means that the tunneling electron has opposite spin to the dot electron state $|\sigma\rangle$. Independent of the actual spin, we assign for this vertex the factor $\sqrt{1-\frac{\delta}{2\epsilon_\mathrm{A}}}/\sqrt{2}$. The right vertex connects the state $|\sigma\rangle$ to $|+\rangle$ by tunneling of an electron with spin σ'. The resulting factor that needs to be assigned is $\sqrt{1+\frac{\delta}{2\epsilon_\mathrm{A}}}/\sqrt{2}$. Thus, with the fourth rule we find

$$\frac{1}{2\pi}\Gamma_\mathrm{N}\sqrt{1-\frac{\delta^2}{4\epsilon_\mathrm{A}^2}} f^-(\omega)\frac{1}{E_+ - \epsilon - \omega + i0^+}. \tag{A.17}$$

For the fifth rule, we assign a global prefactor of $-i$. There is no bullet on the lower propagator, thus, we only need to consider the tunneling processes. In the case of a tunneling spin-up electron, we do not need to assign a -1. In the case of a tunneling spin-down electron we need to assign a -1 for both vertices. Hence, also for the fifth rule, the result is independent of the electron spin. Applying also the integration, we find

$$-\frac{i}{2\pi}\Gamma_\mathrm{N}\sqrt{1-\frac{\delta^2}{4\epsilon_\mathrm{A}^2}}\int_{-\infty}^{\infty} d\omega \frac{f^-(\omega)}{E_+ - \epsilon - \omega + i0^+}, \tag{A.18}$$

which yields

$$-\frac{i}{2\pi}\Gamma_\mathrm{N}\sqrt{1-\frac{\delta^2}{4\epsilon_\mathrm{A}^2}}\left[-\phi^-(E_+ - \epsilon) - i\pi f^-(E_+ - \epsilon)\right]. \tag{A.19}$$

W^{--}_{++}

The diagram is one of four different diagrams that contribute to the rate W^{--}_{++}. Even though the dot state does not change in consequence to the tunneling, we need to consider the rate for our master equation. As above, the diagram allows for the tunneling of a spin-up and a spin-down electron at the same time but the result for each spin is the same. This holds also for the other diagrams contributing to the rate. The other possible diagrams are with a tunneling line going in the opposite direction and a tunneling line on the lower propagator that is either left or right going. The new aspect here is that the tunneling line is left going which is important for the Cauchy integral, see Eq. (A.2).

In the given diagram, there are two left-going energies E_+ and ω and one right-going energy ϵ. With the factor of two to account for the spins, we find

$$\frac{2}{E_+ - \epsilon + \omega + i0^+}. \tag{A.20}$$

The tunneling line goes backward in time, so we assign

$$\frac{1}{\pi}\Gamma_{\mathrm{N}} f^+(\omega)\frac{1}{E_+ - \epsilon + \omega + i0^+}. \tag{A.21}$$

The left vertex connects the state $|-\rangle$ with the state $|\sigma\rangle$ by a tunneling of an electron with spin $\sigma' = \sigma$ because the electron tunnels in at this vertex and continuous on the Keldysh contour. At the other vertex, the same happens with exchange dot states. Thus, we find

$$\frac{1}{2\pi}\Gamma_{\mathrm{N}}\left(1 + \frac{\delta}{2\epsilon_{\mathrm{A}}}\right) f^+(\omega)\frac{1}{E_+ - \epsilon + \omega + i0^+}. \tag{A.22}$$

With the global prefactor of $-i$ and either no assigned -1 for a tunneling spin-down electron or twice assigned -1 for a tunneling spin-up electron, we get for the integration

$$-\frac{i}{2\pi}\Gamma_{\mathrm{N}}\left(1 + \frac{\delta}{2\epsilon_{\mathrm{A}}}\right)\int_{-\infty}^{\infty} d\omega \frac{f^+(\omega)}{E_+ - \epsilon + \omega + i0^+}. \tag{A.23}$$

Before performing the integration, we need to bring the denominator to a form of $x - \omega + i0^+(-1)^j$

$$\frac{i}{2\pi}\Gamma_{\mathrm{N}}\left(1 + \frac{\delta}{2\epsilon_{\mathrm{A}}}\right)\int_{-\infty}^{\infty} d\omega \frac{f^+(\omega)}{\epsilon - E_+ - \omega - i0^+}. \tag{A.24}$$

The solution of this integral is

$$\frac{i}{2\pi}\Gamma_{\mathrm{N}}\left(1 + \frac{\delta}{2\epsilon_{\mathrm{A}}}\right)\left[-\phi^+(\epsilon - E_+) + i\pi f^+(\epsilon - E_+)\right]. \tag{A.25}$$

Appendix B.

Basis transformation of the pseudospin

The time evolution of the reduced density matrix is given by

$$\begin{pmatrix} \dot{P}_{+}^{+} \\ \dot{P}_{-}^{-} \\ \dot{P}_{\uparrow}^{\uparrow} \\ \dot{P}_{\downarrow}^{\downarrow} \\ \dot{P}_{+}^{-} \\ \dot{P}_{-}^{+} \end{pmatrix} = \begin{pmatrix} W_{++}^{++} & 0 & W_{+\uparrow}^{+\uparrow} & W_{+\downarrow}^{+\downarrow} & W_{++}^{+-} & W_{+-}^{++} \\ 0 & W_{--}^{--} & W_{-\uparrow}^{-\uparrow} & W_{-\downarrow}^{-\downarrow} & W_{-+}^{--} & W_{--}^{-+} \\ W_{\uparrow+}^{\uparrow+} & W_{\uparrow-}^{\uparrow-} & W_{\uparrow\uparrow}^{\uparrow\uparrow} & 0 & W_{\uparrow+}^{\uparrow-} & W_{\uparrow-}^{\uparrow+} \\ W_{\downarrow+}^{\downarrow+} & W_{\downarrow-}^{\downarrow-} & 0 & W_{\downarrow\downarrow}^{\downarrow\downarrow} & W_{\downarrow+}^{\downarrow-} & W_{\downarrow-}^{\downarrow+} \\ W_{++}^{-+} & W_{+-}^{--} & W_{+\uparrow}^{-\uparrow} & W_{+\downarrow}^{-\downarrow} & W_{++}^{--} & 0 \\ W_{-+}^{+} & W_{--}^{+-} & W_{-\uparrow}^{+\uparrow} & W_{-\downarrow}^{+\downarrow} & 0 & W_{--}^{++} \end{pmatrix} \begin{pmatrix} P_{+}^{+} \\ P_{-}^{-} \\ P_{\uparrow}^{\uparrow} \\ P_{\downarrow}^{\downarrow} \\ P_{+}^{-} \\ P_{-}^{+} \end{pmatrix}. \tag{B.1}$$

Here, the coherent evolution of the dot state according to Eq. (3.23) is already included into the rates. This is relevant for the rates W_{++}^{--} and W_{--}^{++}. The rates of the matrix are given by

$$W_{++}^{++} = -\Gamma_{\mathrm{N}} \sum_{\gamma=\pm(1)} \left(1+\gamma\frac{\delta}{2\epsilon_{\mathrm{A}}}\right)\left(\frac{1+\gamma}{2} - \gamma f(E_{\mathrm{A},\gamma,\gamma})\right), \tag{B.2}$$

$$W_{+\sigma}^{+\sigma} = \frac{\Gamma_{\mathrm{N}}}{2} \sum_{\gamma=\pm(1)} \left(1+\gamma\frac{\delta}{2\epsilon_{\mathrm{A}}}\right)\left(\frac{1-\gamma}{2} + \gamma f(E_{\mathrm{A},\gamma,\gamma})\right), \tag{B.3}$$

$$W_{++}^{+-} = \frac{\Gamma_{\mathrm{N}}\Gamma_{\mathrm{S}}\cos\frac{\varphi}{2}}{2\epsilon_{\mathrm{A}}} \sum_{\gamma=\pm} \left(f(E_{\mathrm{A},\gamma,\gamma}) - \gamma\frac{i}{\pi}\phi(E_{\mathrm{A},\gamma,\gamma}) - \frac{1}{2}\right), \tag{B.4}$$

$$W_{+-}^{++} = \frac{\Gamma_{\mathrm{N}}\Gamma_{\mathrm{S}}\cos\frac{\varphi}{2}}{2\epsilon_{\mathrm{A}}} \sum_{\gamma=\pm} \left(f(E_{\mathrm{A},\gamma,\gamma}) + \gamma\frac{i}{\pi}\phi(E_{\mathrm{A},\gamma,\gamma}) - \frac{1}{2}\right), \tag{B.5}$$

$$W_{--}^{--} = -\Gamma_{\mathrm{N}} \sum_{\gamma=\pm(1)} \left(1+\gamma\frac{\delta}{2\epsilon_{\mathrm{A}}}\right)\left(\frac{1-\gamma}{2} + \gamma f(E_{\mathrm{A},-\gamma,\gamma})\right), \tag{B.6}$$

$$W_{-\sigma}^{-\sigma} = \frac{\Gamma_{\mathrm{N}}}{2} \sum_{\gamma=\pm(1)} \left(1+\gamma\frac{\delta}{2\epsilon_{\mathrm{A}}}\right)\left(\frac{1+\gamma}{2} - \gamma f(E_{\mathrm{A},-\gamma,\gamma})\right), \tag{B.7}$$

$$W_{-+}^{--} = \frac{\Gamma_{\mathrm{N}}\Gamma_{\mathrm{S}}\cos\frac{\varphi}{2}}{2\epsilon_{\mathrm{A}}} \sum_{\gamma=\pm} \left(f(E_{\mathrm{A},-\gamma,\gamma}) - \gamma\frac{i}{\pi}\phi(E_{\mathrm{A},-\gamma,\gamma}) - \frac{1}{2}\right), \tag{B.8}$$

$$W_{--}^{-+} = \frac{\Gamma_{\mathrm{N}}\Gamma_{\mathrm{S}}\cos\frac{\varphi}{2}}{2\epsilon_{\mathrm{A}}} \sum_{\gamma=\pm} \left(f(E_{\mathrm{A},-\gamma,\gamma}) + \gamma\frac{i}{\pi}\phi(E_{\mathrm{A},-\gamma,\gamma}) - \frac{1}{2}\right), \tag{B.9}$$

$$W_{\sigma+}^{\sigma+} = \frac{\Gamma_{\mathrm{N}}}{2} \sum_{\gamma=\pm(1)} \left(1+\gamma\frac{\delta}{2\epsilon_{\mathrm{A}}}\right)\left(\frac{1+\gamma}{2} - \gamma f(E_{\mathrm{A},\gamma,\gamma})\right), \tag{B.10}$$

$$W_{\sigma-}^{\sigma-} = \frac{\Gamma_\mathrm{N}}{2} \sum_{\gamma=\pm(1)} \left(1+\gamma\frac{\delta}{2\epsilon_\mathrm{A}}\right)\left(\frac{1-\gamma}{2}+\gamma f(E_{\mathrm{A},-\gamma,\gamma})\right), \tag{B.11}$$

$$W_{\sigma\sigma}^{\sigma\sigma} = -\frac{\Gamma_\mathrm{N}}{2} \sum_{\gamma\gamma'=\pm(1)} \left(1+\gamma\frac{\delta}{2\epsilon_\mathrm{A}}\right)\left(\frac{1-\gamma'}{2}+\gamma' f(E_{\mathrm{A},\gamma',\gamma})\right), \tag{B.12}$$

$$W_{\sigma+}^{\sigma-} = \frac{\Gamma_\mathrm{N}\Gamma_\mathrm{S}\cos\frac{\varphi}{2}}{4\epsilon_\mathrm{A}} \sum_{\gamma\gamma'=\pm} \left(\frac{1}{2}-f(E_{\mathrm{A},\gamma',\gamma})+\gamma\frac{i}{\pi}\phi(E_{\mathrm{A},\gamma',\gamma})\right), \tag{B.13}$$

$$W_{\sigma-}^{\sigma+} = \frac{\Gamma_\mathrm{N}\Gamma_\mathrm{S}\cos\frac{\varphi}{2}}{4\epsilon_\mathrm{A}} \sum_{\gamma\gamma'=\pm} \left(\frac{1}{2}-f(E_{\mathrm{A},\gamma',\gamma})-\gamma\frac{i}{\pi}\phi(E_{\mathrm{A},\gamma',\gamma})\right), \tag{B.14}$$

$$W_{++}^{-+} = \frac{\Gamma_\mathrm{N}\Gamma_\mathrm{S}\cos\frac{\varphi}{2}}{2\epsilon_\mathrm{A}} \sum_{\gamma=\pm} \left(f(E_{\mathrm{A},\gamma,\gamma})-\gamma\frac{i}{\pi}\phi(E_{\mathrm{A},\gamma,\gamma})-\frac{1}{2}\right), \tag{B.15}$$

$$W_{+-}^{--} = \frac{\Gamma_\mathrm{N}\Gamma_\mathrm{S}\cos\frac{\varphi}{2}}{2\epsilon_\mathrm{A}} \sum_{\gamma=\pm} \left(f(E_{\mathrm{A},-\gamma,\gamma})-\gamma\frac{i}{\pi}\phi(E_{\mathrm{A},-\gamma,\gamma})-\frac{1}{2}\right), \tag{B.16}$$

$$W_{+\sigma}^{-\sigma} = \frac{\Gamma_\mathrm{N}\Gamma_\mathrm{S}\cos\frac{\varphi}{2}}{4\epsilon_\mathrm{A}} \sum_{\gamma\gamma'=\pm} \left(f(E_{\mathrm{A},\gamma',\gamma})-\gamma\frac{i}{\pi}\phi(E_{\mathrm{A},\gamma',\gamma})-\frac{1}{2}\right), \tag{B.17}$$

$$\begin{aligned} W_{++}^{--} =& 2i\epsilon_\mathrm{A} \\ & -\frac{\Gamma_\mathrm{N}}{2} \sum_{\gamma\gamma'=\pm(1)} \left(1-\gamma\frac{\delta}{2\epsilon_\mathrm{A}}\right)\left(\frac{1+\gamma'}{2}-\gamma' f(E_{\mathrm{A},\gamma',\gamma})+\gamma\gamma'\frac{i}{\pi}\phi(E_{\mathrm{A},\gamma',\gamma})\right), \end{aligned} \tag{B.18}$$

$$W_{-+}^{++} = \frac{\Gamma_\mathrm{N}\Gamma_\mathrm{S}\cos\frac{\varphi}{2}}{2\epsilon_\mathrm{A}} \sum_{\gamma=\pm} \left(f(E_{\mathrm{A},\gamma,\gamma})+\gamma\frac{i}{\pi}\phi(E_{\mathrm{A},\gamma,\gamma})-\frac{1}{2}\right), \tag{B.19}$$

$$W_{--}^{+-} = \frac{\Gamma_\mathrm{N}\Gamma_\mathrm{S}\cos\frac{\varphi}{2}}{2\epsilon_\mathrm{A}} \sum_{\gamma=\pm} \left(f(E_{\mathrm{A},-\gamma,\gamma})+\gamma\frac{i}{\pi}\phi(E_{\mathrm{A},-\gamma,\gamma})-\frac{1}{2}\right), \tag{B.20}$$

$$W_{-\sigma}^{+\sigma} = \frac{\Gamma_\mathrm{N}\Gamma_\mathrm{S}\cos\frac{\varphi}{2}}{4\epsilon_\mathrm{A}} \sum_{\gamma\gamma'=\pm} \left(f(E_{\mathrm{A},\gamma',\gamma})+\gamma\frac{i}{\pi}\phi(E_{\mathrm{A},\gamma',\gamma})-\frac{1}{2}\right), \tag{B.21}$$

$$\begin{aligned} W_{--}^{++} =& -2i\epsilon_\mathrm{A} \\ & -\frac{\Gamma_\mathrm{N}}{2} \sum_{\gamma\gamma'=\pm(1)} \left(1-\gamma\frac{\delta}{2\epsilon_\mathrm{A}}\right)\left(\frac{1+\gamma'}{2}-\gamma' f(E_{\mathrm{A},\gamma',\gamma})-\gamma\gamma'\frac{i}{\pi}\phi(E_{\mathrm{A},\gamma',\gamma})\right). \end{aligned} \tag{B.22}$$

Here, we used the definition of the Andreev bound state energies

$$E_{\mathrm{A},\gamma',\gamma} = \begin{cases} E_+ - \epsilon & \gamma'=+,\gamma=+ \\ \epsilon - E_+ & \gamma'=-,\gamma=- \\ E_- - \epsilon & \gamma'=+,\gamma=- \\ \epsilon - E_- & \gamma'=-,\gamma=+ \end{cases}, \tag{B.23}$$

and from Eq. (3.10)

$$4\epsilon_\mathrm{A}^2 = \delta^2 + 4\Gamma_\mathrm{S}^2\cos^2\frac{\varphi}{2}. \tag{B.24}$$

A physically more intuitive form is the representation of the master equation in the pseudospin base. The pseudospin base is given by Eqs. (3.30)-(3.34). We write this

into a transformation matrix $\mathbf{U}$

$$\begin{pmatrix} P_{\mathrm{e}} \\ P_{\mathrm{o}} \\ I_x \\ I_y \\ I_z \end{pmatrix} = \begin{pmatrix} 1 & 1 & 0 & 0 & 0 & 0 \\ 0 & 0 & 1 & 1 & 0 & 0 \\ -\frac{\Gamma_{\mathrm{S}}\cos\frac{\varphi}{2}}{2\epsilon_{\mathrm{A}}} & \frac{\Gamma_{\mathrm{S}}\cos\frac{\varphi}{2}}{2\epsilon_{\mathrm{A}}} & 0 & 0 & \frac{\delta}{4\epsilon_{\mathrm{A}}} & \frac{\delta}{4\epsilon_{\mathrm{A}}} \\ 0 & 0 & 0 & 0 & -\frac{i}{2} & \frac{i}{2} \\ \frac{\delta}{4\epsilon_{\mathrm{A}}} & -\frac{\delta}{4\epsilon_{\mathrm{A}}} & 0 & 0 & \frac{\Gamma_{\mathrm{S}}\cos\frac{\varphi}{2}}{2\epsilon_{\mathrm{A}}} & \frac{\Gamma_{\mathrm{S}}\cos\frac{\varphi}{2}}{2\epsilon_{\mathrm{A}}} \end{pmatrix} \begin{pmatrix} P_+^+ \\ P_-^- \\ P^{\uparrow}_{\uparrow} \\ P^{\downarrow}_{\downarrow} \\ P_+^- \\ P_-^+ \end{pmatrix}. \tag{B.25}$$

To change the basis of the master equation, we insert $\mathbf{U}$ and its inverse $\mathbf{U}^{-1}$

$$\dot{\rho}_{\pm} = \mathbf{W}_{\pm}\rho_{\pm}, \tag{B.26}$$
$$\Leftrightarrow \dot{\rho}_{\pm} = \mathbf{W}_{\pm}\mathbf{U}^{-1}\mathbf{U}\rho_{\pm}, \tag{B.27}$$
$$\Leftrightarrow \mathbf{U}\dot{\rho}_{\pm} = \mathbf{U}\mathbf{W}_{\pm}\mathbf{U}^{-1}\mathbf{U}\rho_{\pm}, \tag{B.28}$$
$$\Leftrightarrow \dot{\rho}_{\mathbf{I}} = \mathbf{W}_{\mathbf{I}}\rho_{\mathbf{I}}. \tag{B.29}$$

Here, the index $\pm$ denotes that the density matrix elements of ρ and the rate matrix $\mathbf{W}$ are in the $\pm$ basis and the index $\mathbf{I}$ that they are in the pseudospin base. The rates in the pseudospin base are given by

$$W_{ee} = \frac{\Gamma_{\mathrm{N}}}{2}\sum_{\gamma\gamma'=\pm}\left(1+\gamma\frac{\delta}{2\epsilon_{\mathrm{A}}}\right)\left(\gamma' f(E_{\mathrm{A},\gamma',\gamma}) - \frac{1}{2}\right), \tag{B.30}$$
$$W_{eo} = \frac{\Gamma_{\mathrm{N}}}{2}\sum_{\gamma\gamma'=\pm}\left(1+\gamma\frac{\delta}{2\epsilon_{\mathrm{A}}}\right)\left(\gamma' f(E_{\mathrm{A},\gamma',\gamma}) + \frac{1}{2}\right), \tag{B.31}$$
$$W_{eI_x} = -\frac{\Gamma_{\mathrm{N}}\Gamma_{\mathrm{S}}\cos\frac{\varphi}{2}}{\epsilon_{\mathrm{A}}}\sum_{\gamma\gamma'=\pm}\gamma f(E_{\mathrm{A},\gamma',\gamma}), \tag{B.32}$$
$$W_{eI_y} = \frac{\Gamma_{\mathrm{N}}\Gamma_{\mathrm{S}}\cos\frac{\varphi}{2}}{\pi\epsilon_{\mathrm{A}}}\sum_{\gamma\gamma'=\pm}\gamma\phi(E_{\mathrm{A},\gamma',\gamma}), \tag{B.33}$$
$$W_{eI_z} = \Gamma_{\mathrm{N}}\sum_{\gamma\gamma'=\pm}\left(1+\gamma\frac{\delta}{2\epsilon_{\mathrm{A}}}\right)\left(f(E_{\mathrm{A},\gamma',\gamma}) - \frac{1}{2}\right), \tag{B.34}$$
$$W_{oe} = -\frac{\Gamma_{\mathrm{N}}}{2}\sum_{\gamma\gamma'=\pm}\left(1+\gamma\frac{\delta}{2\epsilon_{\mathrm{A}}}\right)\left(\gamma' f(E_{\mathrm{A},\gamma',\gamma}) - \frac{1}{2}\right), \tag{B.35}$$
$$W_{oo} = -\frac{\Gamma_{\mathrm{N}}}{2}\sum_{\gamma\gamma'=\pm}\left(1+\gamma\frac{\delta}{2\epsilon_{\mathrm{A}}}\right)\left(\gamma' f(E_{\mathrm{A},\gamma',\gamma}) + \frac{1}{2}\right), \tag{B.36}$$
$$W_{oI_x} = \frac{\Gamma_{\mathrm{N}}\Gamma_{\mathrm{S}}\cos\frac{\varphi}{2}}{\epsilon_{\mathrm{A}}}\sum_{\gamma\gamma'=\pm}\gamma f(E_{\mathrm{A},\gamma',\gamma}), \tag{B.37}$$
$$W_{oI_y} = -\frac{\Gamma_{\mathrm{N}}\Gamma_{\mathrm{S}}\cos\frac{\varphi}{2}}{\pi\epsilon_{\mathrm{A}}}\sum_{\gamma\gamma'=\pm}\gamma\phi(E_{\mathrm{A},\gamma',\gamma}), \tag{B.38}$$
$$W_{oI_z} = -\Gamma_{\mathrm{N}}\sum_{\gamma\gamma'=\pm}\left(1+\gamma\frac{\delta}{2\epsilon_{\mathrm{A}}}\right)\left(f(E_{\mathrm{A},\gamma',\gamma}) - \frac{1}{2}\right), \tag{B.39}$$
$$W_{I_xe} = -\frac{\Gamma_{\mathrm{N}}\Gamma_{\mathrm{S}}\cos\frac{\varphi}{2}}{4\epsilon_{\mathrm{A}}}\sum_{\gamma\gamma'=\pm}\gamma f(E_{\mathrm{A},\gamma',\gamma}), \tag{B.40}$$

$$W_{I_xo} = -\frac{\Gamma_\mathrm{N}\Gamma_\mathrm{S}\cos\frac{\varphi}{2}}{4\epsilon_\mathrm{A}} \sum_{\gamma\gamma'=\pm} \gamma f(E_{\mathrm{A},\gamma',\gamma}), \tag{B.41}$$

$$W_{I_xI_x} = \frac{\Gamma_\mathrm{N}}{2} \sum_{\gamma\gamma'=\pm} \left(1 - \gamma\frac{\delta}{2\epsilon_\mathrm{A}}\right)\left(\gamma' f(E_{\mathrm{A},\gamma',\gamma}) - \frac{1}{2}\right), \tag{B.42}$$

$$W_{I_xI_y} = -\delta - \frac{\Gamma_\mathrm{N}}{2\pi} \sum_{\gamma\gamma'=\pm} \left(1 - \gamma\frac{\delta}{2\epsilon_\mathrm{A}}\right)\gamma'\phi(E_{\mathrm{A},\gamma'\gamma}), \tag{B.43}$$

$$W_{I_xI_z} = -\frac{\Gamma_\mathrm{N}\Gamma_\mathrm{S}\cos\frac{\varphi}{2}}{2\epsilon_\mathrm{A}} \sum_{\gamma\gamma'=\pm} \gamma\gamma' f(E_{\mathrm{A},\gamma',\gamma}), \tag{B.44}$$

$$W_{I_ye} = -\frac{\Gamma_\mathrm{N}\Gamma_\mathrm{S}\cos\frac{\varphi}{2}}{4\pi\epsilon_\mathrm{A}} \sum_{\gamma\gamma'=\pm} \gamma\phi(E_{\mathrm{A},\gamma',\gamma}), \tag{B.45}$$

$$W_{I_yo} = -\frac{\Gamma_\mathrm{N}\Gamma_\mathrm{S}\cos\frac{\varphi}{2}}{4\pi\epsilon_\mathrm{A}} \sum_{\gamma\gamma'=\pm} \gamma\phi(E_{\mathrm{A},\gamma',\gamma}), \tag{B.46}$$

$$W_{I_yI_x} = \delta + \frac{\Gamma_\mathrm{N}}{2\pi} \sum_{\gamma\gamma'=\pm} \left(1 - \gamma\frac{\delta}{2\epsilon_\mathrm{A}}\right)\gamma'\phi(E_{\mathrm{A},\gamma'\gamma}), \tag{B.47}$$

$$W_{I_yI_y} = \frac{\Gamma_\mathrm{N}}{2} \sum_{\gamma\gamma'=\pm} \left(1 - \gamma\frac{\delta}{2\epsilon_\mathrm{A}}\right)\left(\gamma' f(E_{\mathrm{A},\gamma',\gamma}) - \frac{1}{2}\right), \tag{B.48}$$

$$W_{I_yI_z} = 2\Gamma_\mathrm{S}\cos\frac{\varphi}{2} - \frac{\Gamma_\mathrm{N}\Gamma_\mathrm{S}\cos\frac{\varphi}{2}}{2\pi\epsilon_\mathrm{A}} \sum_{\gamma\gamma'=\pm} \gamma\gamma'\phi(E_{\mathrm{A},\gamma',\gamma}), \tag{B.49}$$

$$W_{I_ze} = \frac{\Gamma_\mathrm{N}}{4} \sum_{\gamma\gamma'=\pm} \left(1 + \gamma\frac{\delta}{2\epsilon_\mathrm{A}}\right)\left(f(E_{\mathrm{A},\gamma',\gamma}) - \frac{1}{2}\right), \tag{B.50}$$

$$W_{I_zo} = \frac{\Gamma_\mathrm{N}}{4} \sum_{\gamma\gamma'=\pm} \left(1 + \gamma\frac{\delta}{2\epsilon_\mathrm{A}}\right)\left(f(E_{\mathrm{A},\gamma',\gamma}) - \frac{1}{2}\right), \tag{B.51}$$

$$W_{I_zI_x} = -\frac{\Gamma_\mathrm{N}\Gamma_\mathrm{S}\cos\frac{\varphi}{2}}{2\epsilon_\mathrm{A}} \sum_{\gamma\gamma'=\pm} \gamma\gamma' f(E_{\mathrm{A},\gamma',\gamma}), \tag{B.52}$$

$$W_{I_zI_y} = -2\Gamma_\mathrm{S}\cos\frac{\varphi}{2} + \frac{\Gamma_\mathrm{N}\Gamma_\mathrm{S}\cos\frac{\varphi}{2}}{2\pi\epsilon_\mathrm{A}} \sum_{\gamma\gamma'=\pm} \gamma\gamma'\phi(E_{\mathrm{A},\gamma',\gamma}), \tag{B.53}$$

$$W_{I_zI_z} = \frac{\Gamma_\mathrm{N}}{2} \sum_{\gamma\gamma'=\pm} \left(1 + \gamma\frac{\delta}{2\epsilon_\mathrm{A}}\right)\left(\gamma' f(E_{\mathrm{A},\gamma',\gamma}) - \frac{1}{2}\right). \tag{B.54}$$

Using that $P_\mathrm{e} + P_\mathrm{o} = 1$, we write the time evolution of the pseudospin in a Bloch-type equation

$$\dot{\mathbf{I}} = \begin{pmatrix} W_{I_xe} \\ W_{I_ye} \\ W_{I_ze} \end{pmatrix} + \begin{pmatrix} W_{I_xI_x} & W_{I_xI_y} & W_{I_xI_z} \\ W_{I_yI_x} & W_{I_yI_y} & W_{I_yI_z} \\ W_{I_zI_x} & W_{I_zI_y} & W_{I_zI_z} \end{pmatrix} \mathbf{I}, \tag{B.55}$$

where the first vector is the accumulation vector and the matrix is a composition of the relaxation matrix and the exchange field from Eq. (3.54).

Appendix C.

Algorithm for the trajectory-based Monte-Carlo simulation

Here, we explain in more detail the main body of the trajectory-based simulation. The algorithm for a single sweep is sketched in Fig. C.1. The ellipses represent the start and the end of the sweep. In the rectangles, the calculations and orders are shown. The rotated squares are decisions which asks for a condition which is either true or false. Finally, there is one rhomboid which is the output of the simulation sweep. The sweep starts by defining the sample by its thickness d_{Au}. Then, an electron is initialized by defining its place which is $\{x, y, z\} = 0$ and energy E. For the injection, a polar θ_{init} and azimuth angle φ_{init} is isotropically set by a random number generator. The initial electron is the first entry in the list of electrons. Secondary electrons that are excited due to electron-electron scattering are added in the list consecutively. The entries for each electron in the list are its current place and energy, the initial angles, the angles for the current direction, the total path length and the number of collisions. This list is updated every time when one of its entries is changed during the sweep.

After the initialization, the first decision asks if all electrons in the list have been simulated. If true, the sweep ends and, if false, the electron trajectory starts. In the following rectangle, a path length is determined by a random number generator according to the distribution function in Eq. (4.2) which is subsequentially added to the total path length. After calculating the new position of the electron, the next conditions are queried.

At first, we ask if the z-component greater than d_{Au} which means that the electron has reached the surface of the sample. In this case, the total path length is corrected and the final energy, the corrected total path length, the initial angle and the number of collisions is exported. If there is another electron in the list, the next electron is simulated. If the z-component is smaller than the gold thickness, we look if the electron has been reinjected into the Fe layer. If true, the electron is discarded from the simulation sweep and we continue with the next electron if possible. If the electron is still inside the sample, a scattering event is initialized.

Here, we take care of the energy transfer. We calculate the new energy by multiplying the old energy with a random number X between zero and one. Afterwards, we take the energy difference and add one collision for the electron. Next, we initialize the secondary electron which gets an energy in the range $[0, \Delta E]$ set by another random number X. In the next step, it is proofed if the secondary electron is included to the list of electrons. This is the case when the energy of the secondary electron is larger than the cutoff energy E_{cut}. The list entries are given by the current entries of the parent electron except for the energy and the angles for the direction which are chosen

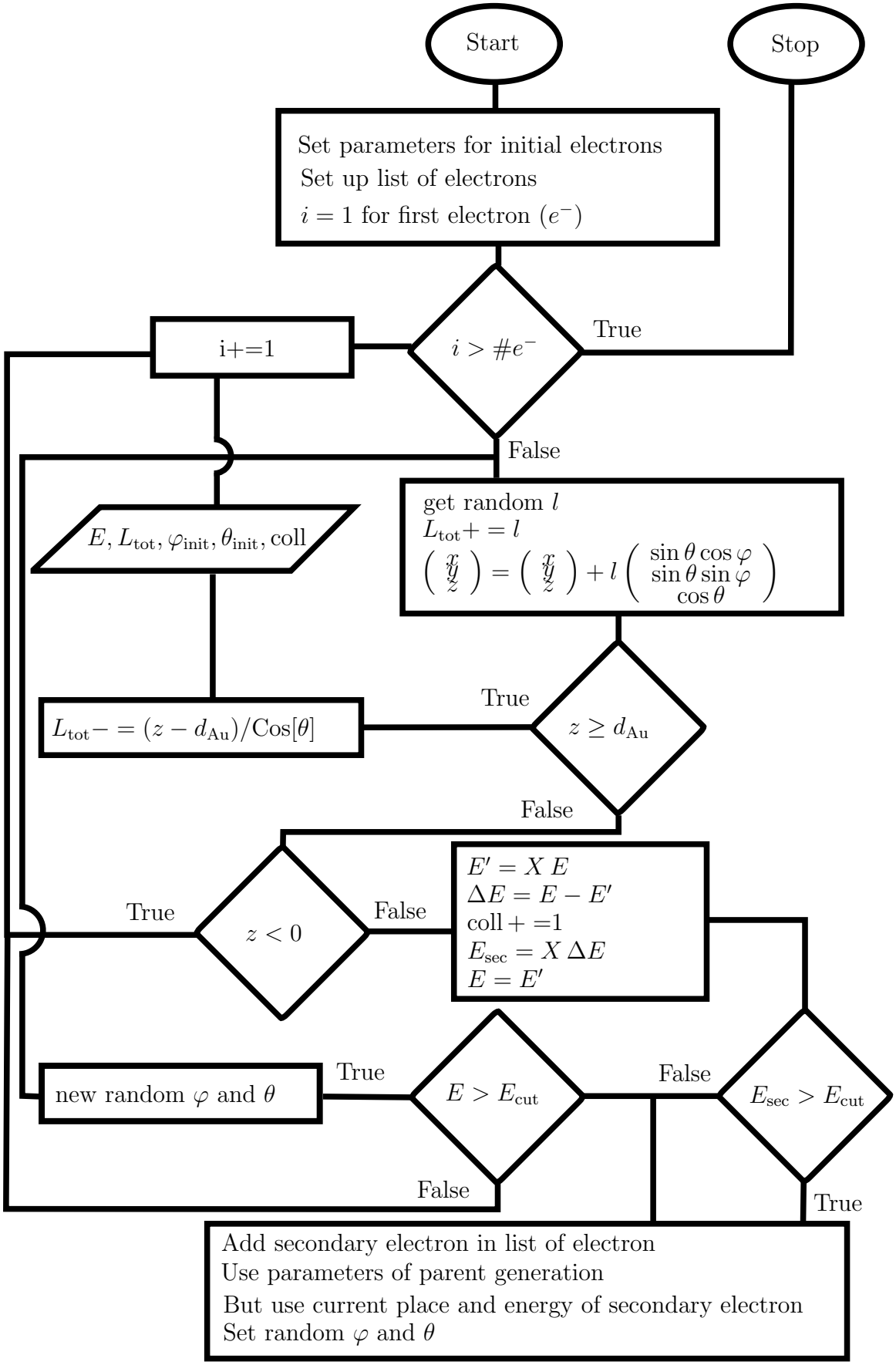

Figure C.1.: Program flow chart for one simulation sweep. See text for details.

randomly.

Afterwards or if the secondary electron is discarded, we continue with the parent electron. For this electron, we also need to check if the energy has dropped below the threshold. If this is the case, the electron is discarded and we continue with the next electron if possible. In the other case, when the electron energy is still above E_{cut}, the electron gets new random angles and the sweep continues with a new path length determined by a random number generator, see above.

In the best case, at least one electron reaches the sample surface and we get the corresponding export. However, if the cutoff energy is high or the sample thickness large, it becomes more likely that all electrons in the sweep are discarded. In this case, the sweep is restarted to ensure that the demanded number of electrons contribute to the statistics.

Bibliography

[1] B. Dibner, *Oersted and the discovery of electromagnetism*, 2nd ed. (Blaisdell Publ., 1962).

[2] W. Demtröder, *Experimentalphysik 2: Elektrizität und Optik*, Springer-Lehrbuch (Springer, Berlin, Heidelberg, 2013).

[3] M. Faraday, V. Experimental researches in electricity, Philosophical Transactions of the Royal Society of London **122**, 125 (1997).

[4] F. E. Talke, An Overview of Current Tribology Problems in Magnetic Disk Recording Technology, in *Tribology Series*, Thinning Films and Tribological Interfaces, Vol. 38, edited by D. Dowson, M. Priest, C. M. Taylor, P. Ehret, T. H. C. Childs, G. Dalmaz, A. A. Lubrecht, Y. Berthier, L. Flamand, and J. M. Georges (Elsevier, 2000) pp. 15–24.

[5] D. Kumar, T. Jin, R. Sbiaa, M. Kläui, S. Bedanta, S. Fukami, D. Ravelosona, S.-H. Yang, X. Liu, and S. N. Piramanayagam, Domain wall memory: Physics, materials, and devices, Physics Reports Domain Wall Memory: Physics, Materials, and Devices, **958**, 1 (2022).

[6] K. S. Novoselov, Z. Jiang, Y. Zhang, S. V. Morozov, H. L. Stormer, U. Zeitler, J. C. Maan, G. S. Boebinger, P. Kim, and A. K. Geim, Room-Temperature Quantum Hall Effect in Graphene, Science **315**, 1379 (2007).

[7] K. v. Klitzing, G. Dorda, and M. Pepper, New Method for High-Accuracy Determination of the Fine-Structure Constant Based on Quantized Hall Resistance, Physical Review Letters **45**, 494 (1980).

[8] F. Kühne, Y. Beyazit, B. Sothmann, J. Jayabalan, D. Diesing, P. Zhou, and U. Bovensiepen, Ultrafast transport and energy relaxation of hot electrons in Au/Fe/MgO(001) heterostructures analyzed by linear time-resolved photoelectron spectroscopy, Physical Review Research **4**, 033239 (2022).

[9] M. Heckschen, Y. Beyazit, E. Shomali, F. Kühne, J. Jayabalan, P. Zhou, D. Diesing, M. E. Gruner, R. Pentcheva, A. Lorke, B. Sothmann, and U. Bovensiepen, Spatio-Temporal Electron Propagation Dynamics in Au/Fe/MgO(001) in Nonequilibrium: Revealing Single Scattering Events and the Ballistic Limit, PRX Energy **2**, 043009 (2023).

[10] N. S, H. Singh, and A. U. N, An extensive review on quantum computers, Advances in Engineering Software **174**, 103337 (2022).

[11] L. Hofstetter, S. Csonka, J. Nygård, and C. Schönenberger, Cooper pair splitter realized in a two-quantum-dot Y-junction, Nature **461**, 960 (2009).

[12] V. V. Kabanov and A. S. Alexandrov, Electron relaxation in metals: Theory and exact analytical solutions, Physical Review B **78**, 174514 (2008).

[13] H. Kammerlingh Onnes, The superconductivity of mercury, Comm. Phys. Lab. Univ. Leiden **122**, 122 (1911).

[14] D. van Delft and P. Kes, The discovery of superconductivity, Physics Today **63**, 38 (2010).

[15] M. Stemmle, F. Merschel, M. Noe, and A. Hobl, AmpaCity - Installation of advanced superconducting 10 kV system in city center replaces conventional 110 kV cables, Proceedings of the International Conference on Applied Superconductivity and Electromagnetic Devices (ASEMD2013), Beijing, CHN, October 25-27, 2013 , 323 (2013).

[16] J. E. Kunzler, E. Buehler, F. S. L. Hsu, and J. H. Wernick, Superconductivity in Nb_3Sn at High Current Density in a Magnetic Field of 88 kgauss, Physical Review Letters **6**, 89 (1961).

[17] S. Hahn, K. Kim, K. Kim, X. Hu, T. Painter, I. Dixon, S. Kim, K. R. Bhattarai, S. Noguchi, J. Jaroszynski, and D. C. Larbalestier, 45.5-tesla direct-current magnetic field generated with a high-temperature superconducting magnet, Nature **570**, 496 (2019).

[18] J. M. Gambetta, J. M. Chow, and M. Steffen, Building logical qubits in a superconducting quantum computing system, npj Quantum Information **3**, 1 (2017).

[19] M. Kjaergaard, M. E. Schwartz, J. Braumüller, P. Krantz, J. I.-J. Wang, S. Gustavsson, and W. D. Oliver, Superconducting Qubits: Current State of Play, Annual Review of Condensed Matter Physics **11**, 369 (2020).

[20] G. Wendin, Quantum information processing with superconducting circuits: a review, Reports on Progress in Physics **80**, 106001 (2017).

[21] R. S. Mong, D. J. Clarke, J. Alicea, N. H. Lindner, P. Fendley, C. Nayak, Y. Oreg, A. Stern, E. Berg, K. Shtengel, and M. P. Fisher, Universal Topological Quantum Computation from a Superconductor-Abelian Quantum Hall Heterostructure, Physical Review X **4**, 011036 (2014).

[22] Y. Wu, W.-S. Bao, S. Cao, F. Chen, M.-C. Chen, X. Chen, T.-H. Chung, H. Deng, Y. Du, D. Fan, M. Gong, C. Guo, C. Guo, S. Guo, L. Han, L. Hong, H.-L. Huang, Y.-H. Huo, L. Li, N. Li, S. Li, Y. Li, F. Liang, C. Lin, J. Lin, H. Qian, D. Qiao, H. Rong, H. Su, L. Sun, L. Wang, S. Wang, D. Wu, Y. Xu, K. Yan, W. Yang, Y. Yang, Y. Ye, J. Yin, C. Ying, J. Yu, C. Zha, C. Zhang, H. Zhang, K. Zhang, Y. Zhang, H. Zhao, Y. Zhao, L. Zhou, Q. Zhu, C.-Y. Lu, C.-Z. Peng, X. Zhu, and J.-W. Pan, Strong Quantum Computational Advantage Using a Superconducting Quantum Processor, Physical Review Letters **127**, 180501 (2021).

[23] M. Tinkham, *Introduction to Superconductivity: Second Edition*, second edition ed. (Dover Publications, Mineola, NY, 2004).

[24] J. Bardeen, L. N. Cooper, and J. R. Schrieffer, Theory of Superconductivity, Physical Review **108**, 1175 (1957).

[25] H. Fröhlich, Isotope Effect in Superconductivity, Proceedings of the Physical Society. Section A **63**, 778 (1950).

[26] C. Kittel, *Introduction to Solid State Physics*, 8th ed. (Wiley John + Sons, Hoboken, NJ, 2004).

[27] N. N. Bogoljubov, On a new method in the theory of superconductivity, Il Nuovo Cimento (1955-1965) **7**, 794 (1958).

[28] J. G. Valatin, Comments on the theory of superconductivity, Il Nuovo Cimento (1955-1965) **7**, 843 (1958).

[29] P. W. Anderson, Coherent Excited States in the Theory of Superconductivity: Gauge Invariance and the Meissner Effect, Physical Review **110**, 827 (1958).

[30] Y. Nambu, Quasi-Particles and Gauge Invariance in the Theory of Superconductivity, Physical Review **117**, 648 (1960).

[31] P. W. Anderson, Plasmons, Gauge Invariance, and Mass, Physical Review **130**, 439 (1963).

[32] D. Pekker and C. Varma, Amplitude/Higgs Modes in Condensed Matter Physics, Annual Review of Condensed Matter Physics **6**, 269 (2015).

[33] R. Shimano and N. Tsuji, Higgs Mode in Superconductors, Annual Review of Condensed Matter Physics **11**, 103 (2020).

[34] W. L. Chan, J. Deibel, and D. M. Mittleman, Imaging with terahertz radiation, Reports on Progress in Physics **70**, 1325 (2007).

[35] R. Sooryakumar and M. V. Klein, Raman Scattering by Superconducting-Gap Excitations and Their Coupling to Charge-Density Waves, Physical Review Letters **45**, 660 (1980).

[36] R. Sooryakumar and M. V. Klein, Raman scattering from superconducting gap excitations in the presence of a magnetic field, Physical Review B **23**, 3213 (1981).

[37] R. Matsunaga, Y. I. Hamada, K. Makise, Y. Uzawa, H. Terai, Z. Wang, and R. Shimano, Higgs Amplitude Mode in the BCS Superconductors $Nb_{1-x}Ti_xN$ Induced by Terahertz Pulse Excitation, Physical Review Letters **111**, 057002 (2013).

[38] Y.-Z. Chou, Y. Liao, and M. S. Foster, Twisting Anderson pseudospins with light: Quench dynamics in terahertz-pumped BCS superconductors, Physical Review B **95**, 104507 (2017).

[39] F. Yang and M. W. Wu, Gauge-invariant microscopic kinetic theory of superconductivity: Application to the optical response of Nambu-Goldstone and Higgs modes, Physical Review B **100**, 104513 (2019).

[40] R. Matsunaga, N. Tsuji, H. Fujita, A. Sugioka, K. Makise, Y. Uzawa, H. Terai, Z. Wang, H. Aoki, and R. Shimano, Light-induced collective pseudospin precession resonating with Higgs mode in a superconductor, Science **345**, 1145 (2014).

[41] N. Tsuji and H. Aoki, Theory of Anderson pseudospin resonance with Higgs mode in superconductors, Physical Review B **92**, 064508 (2015).

[42] A. Behrle, T. Harrison, J. Kombe, K. Gao, M. Link, J.-S. Bernier, C. Kollath, and M. Köhl, Higgs mode in a strongly interacting fermionic superfluid, Nature Physics **14**, 781 (2018).

[43] L. Schwarz, B. Fauseweh, N. Tsuji, N. Cheng, N. Bittner, H. Krull, M. Berciu, G. S. Uhrig, A. P. Schnyder, S. Kaiser, and D. Manske, Classification and characterization of nonequilibrium Higgs modes in unconventional superconductors, Nature Communications **11**, 287 (2020).

[44] H. Chu, M.-J. Kim, K. Katsumi, S. Kovalev, R. D. Dawson, L. Schwarz, N. Yoshikawa, G. Kim, D. Putzky, Z. Z. Li, H. Raffy, S. Germanskiy, J.-C. Deinert, N. Awari, I. Ilyakov, B. Green, M. Chen, M. Bawatna, G. Cristiani, G. Logvenov, Y. Gallais, A. V. Boris, B. Keimer, A. P. Schnyder, D. Manske, M. Gensch, Z. Wang, R. Shimano, and S. Kaiser, Phase-resolved Higgs response in superconducting cuprates, Nature Communications **11**, 1793 (2020).

[45] H. Krull, N. Bittner, G. S. Uhrig, D. Manske, and A. P. Schnyder, Coupling of Higgs and Leggett modes in non-equilibrium superconductors, Nature Communications **7**, 11921 (2016).

[46] M. Buzzi, G. Jotzu, A. Cavalleri, J. I. Cirac, E. A. Demler, B. I. Halperin, M. D. Lukin, T. Shi, Y. Wang, and D. Podolsky, Higgs-Mediated Optical Amplification in a Nonequilibrium Superconductor, Physical Review X **11**, 011055 (2021).

[47] D. Bera, L. Qian, T.-K. Tseng, and P. H. Holloway, Quantum Dots and Their Multimodal Applications: A Review, Materials **3**, 2260 (2010).

[48] S. Coe-Sullivan, Quantum dot developments, Nature Photonics **3**, 315 (2009).

[49] K.-S. Cho, E. K. Lee, W.-J. Joo, E. Jang, T.-H. Kim, S. J. Lee, S.-J. Kwon, J. Y. Han, B.-K. Kim, B. L. Choi, and J. M. Kim, High-performance crosslinked colloidal quantum-dot light-emitting diodes, Nature Photonics **3**, 341 (2009).

[50] R. M. Taylor, K. H. Church, and M. I. Sluch, Red light emission from hybrid organic/inorganic quantum dot AC light emitting displays, Displays **28**, 92 (2007).

[51] J. S. Steckel, J. P. Zimmer, S. Coe-Sullivan, N. E. Stott, V. Bulović, and M. G. Bawendi, Blue Luminescence from (CdS)ZnS Core–Shell Nanocrystals, Angewandte Chemie International Edition **43**, 2154 (2004).

[52] J. Song, X. Sun, Z. Li, L. Yu, J. Zhuang, Y. Chen, H. Huang, C. Xiang, J. J. G. Lee, and D. Fu, 24.4: Invited Paper: The Breakthrough of large size electrical luminescence H-Q LED TV, with 4K resolution and top emission device architecture, fabricated by ink jet printing technology, SID Symposium Digest of Technical Papers **50**, 243 (2019).

[53] D. L. Huffaker, G. Park, Z. Zou, O. B. Shchekin, and D. G. Deppe, 1.3 μm room-temperature GaAs-based quantum-dot laser, Applied Physics Letters **73**, 2564 (1998).

[54] U. W. Pohl and D. Bimberg, Semiconductor Disk Lasers Based on Quantum Dots, in *Semiconductor Disk Lasers* (John Wiley & Sons, Ltd, 2010) pp. 187–211.

[55] Y. Wang and N. Herron, Photoconductivity of CdS nanocluster-doped polymers, Chemical Physics Letters **200**, 71 (1992).

[56] P. Lodahl, S. Mahmoodian, and S. Stobbe, Interfacing single photons and single quantum dots with photonic nanostructures, Reviews of Modern Physics **87**, 347 (2015).

[57] H. S. Nguyen, G. Sallen, C. Voisin, P. Roussignol, C. Diederichs, and G. Cassabois, Ultra-coherent single photon source, Applied Physics Letters **99**, 261904 (2011).

[58] C. Matthiesen, A. N. Vamivakas, and M. Atatüre, Subnatural Linewidth Single Photons from a Quantum Dot, Physical Review Letters **108**, 093602 (2012).

[59] C. Matthiesen, M. Geller, C. H. H. Schulte, C. Le Gall, J. Hansom, Z. Li, M. Hugues, E. Clarke, and M. Atatüre, Phase-locked indistinguishable photons with synthesized waveforms from a solid-state source, Nature Communications **4**, 1600 (2013).

[60] Y.-M. He, Y. He, Y.-J. Wei, D. Wu, M. Atatüre, C. Schneider, S. Höfling, M. Kamp, C.-Y. Lu, and J.-W. Pan, On-demand semiconductor single-photon source with near-unity indistinguishability, Nature Nanotechnology **8**, 213 (2013).

[61] S. L. Portalupi and P. Michler, Resonantly Excited Quantum Dots: Superior Non-classical Light Sources for Quantum Information, in *Quantum Dots for Quantum Information Technologies*, Nano-Optics and Nanophotonics, edited by P. Michler (Springer International Publishing, Cham, 2017) pp. 77–121.

[62] D. Loss and D. P. DiVincenzo, Quantum computation with quantum dots, Physical Review A **57**, 120 (1998).

[63] G. Burkard, H.-A. Engel, and D. Loss, Spintronics and Quantum Dots for Quantum Computing and Quantum Communication, Fortschritte der Physik **48**, 965 (2000).

[64] C. Kloeffel and D. Loss, Prospects for Spin-Based Quantum Computing in Quantum Dots, Annual Review of Condensed Matter Physics **4**, 51 (2013).

[65] H. Ishikuro and T. Hiramoto, Quantum mechanical effects in the silicon quantum dot in a single-electron transistor, Applied Physics Letters **71**, 3691 (1997).

[66] H.-A. Engel, P. Recher, and D. Loss, Electron spins in quantum dots for spintronics and quantum computation, Solid State Communications **119**, 229 (2001).

[67] S. De Franceschi, S. Sasaki, J. M. Elzerman, W. G. van der Wiel, S. Tarucha, and L. P. Kouwenhoven, Electron Cotunneling in a Semiconductor Quantum Dot, Physical Review Letters **86**, 878 (2001).

[68] J. B. Ketterson and S. N. Song, *Superconductivity* (Cambridge University Press, Cambridge, 1999).

[69] K. Kopitzki and P. Herzog, Supraleitung, in *Einführung in die Festkörperphysik*, edited by K. Kopitzki and P. Herzog (Springer, Berlin, Heidelberg, 2017) pp. 287–388.

[70] A. Martín-Rodero and A. Levy Yeyati, Josephson and Andreev transport through quantum dots, Advances in Physics **60**, 899 (2011).

[71] S. De Franceschi, L. Kouwenhoven, C. Schönenberger, and W. Wernsdorfer, Hybrid superconductor-quantum dot devices, Nature Nanotechnology **5**, 703 (2010).

[72] D. Futterer, M. Governale, M. G. Pala, and J. König, Nonlocal Andreev transport through an interacting quantum dot, Physical Review B **79**, 054505 (2009).

[73] A. G. Moghaddam, M. Governale, and J. König, Driven superconducting proximity effect in interacting quantum dots, Physical Review B **85**, 094518 (2012).

[74] D. Futterer, J. Swiebodzinski, M. Governale, and J. König, Renormalization effects in interacting quantum dots coupled to superconducting leads, Physical Review B **87**, 014509 (2013).

[75] J. Schindele, A. Baumgartner, R. Maurand, M. Weiss, and C. Schönenberger, Nonlocal spectroscopy of Andreev bound states, Physical Review B **89**, 045422 (2014).

[76] R. S. Souto, A. Martín-Rodero, and A. L. Yeyati, Andreev Bound States Formation and Quasiparticle Trapping in Quench Dynamics Revealed by Time-Dependent Counting Statistics, Physical Review Letters **117**, 267701 (2016).

[77] R. S. Souto, A. Martín-Rodero, and A. L. Yeyati, Quench dynamics in superconducting nanojunctions: Metastability and dynamical Yang-Lee zeros, Physical Review B **96**, 165444 (2017).

[78] M. Kamp and B. Sothmann, Higgs-like pair amplitude dynamics in superconductor–quantum-dot hybrids, Physical Review B **103**, 045414 (2021).

[79] R. Taranko, T. Kwapiński, and T. Domański, Transient dynamics of a quantum dot embedded between two superconducting leads and a metallic reservoir, Physical Review B **99**, 165419 (2019).

[80] K. Wrześniewski, B. Baran, R. Taranko, T. Domański, and I. Weymann, Quench dynamics of a correlated quantum dot sandwiched between normal-metal and superconducting leads, Physical Review B **103**, 155420 (2021).

[81] L. L. Hinchey and D. L. Mills, Magnetic properties of superlattices formed from ferromagnetic and antiferromagnetic materials, Physical Review B **33**, 3329 (1986).

[82] K. G. Günther, Aufdampfschichten aus halbleitenden III-V-Verbindungen, Zeitschrift für Naturforschung A **13**, 1081 (1958).

[83] J. Xu, M. A. Howson, P. Hucknall, B. J. Hickey, R. Venkataraman, C. Hammond, M. J. Walker, and D. Greig, Systematic study of molecular beam epitaxy growth and magnetic properties of Fe on Au(111), Journal of Applied Physics **81**, 3908 (1997).

[84] K. Shintaku, Y. Daitoh, and T. Shinjo, Magnetoresistance effect and interlayer exchange coupling in epitaxial Fe/Au(100) and Fe/Au(111) multilayers, Physical Review B **47**, 14584 (1993).

[85] P. Grünberg, R. Schreiber, Y. Pang, M. B. Brodsky, and H. Sowers, Layered Magnetic Structures: Evidence for Antiferromagnetic Coupling of Fe Layers across Cr Interlayers, Physical Review Letters **57**, 2442 (1986).

[86] G. Binasch, P. Grünberg, F. Saurenbach, and W. Zinn, Enhanced magnetoresistance in layered magnetic structures with antiferromagnetic interlayer exchange, Physical Review B **39**, 4828 (1989).

[87] A. Fert, Nobel Lecture: Origin, development, and future of spintronics, Reviews of Modern Physics **80**, 1517 (2008).

[88] D. T. Dekadjevi, P. A. Ryan, B. J. Hickey, B. D. Fulthorpe, and B. K. Tanner, Experimental Evidence for Electron Channeling in Fe /Au (100) Superlattices, Physical Review Letters **86**, 5787 (2001).

[89] A. Alekhin, I. Razdolski, N. Ilin, J. P. Meyburg, D. Diesing, V. Roddatis, I. Rungger, M. Stamenova, S. Sanvito, U. Bovensiepen, and A. Melnikov, Femtosecond Spin Current Pulses Generated by the Nonthermal Spin-Dependent Seebeck Effect and Interacting with Ferromagnets in Spin Valves, Physical Review Letters **119**, 017202 (2017).

[90] K. Uchida, S. Takahashi, K. Harii, J. Ieda, W. Koshibae, K. Ando, S. Maekawa, and E. Saitoh, Observation of the spin Seebeck effect, Nature **455**, 778 (2008).

[91] A. Slachter, F. L. Bakker, J.-P. Adam, and B. J. van Wees, Thermally driven spin injection from a ferromagnet into a non-magnetic metal, Nature Physics **6**, 879 (2010).

[92] E. Beaurepaire, J.-C. Merle, A. Daunois, and J.-Y. Bigot, Ultrafast Spin Dynamics in Ferromagnetic Nickel, Physical Review Letters **76**, 4250 (1996).

[93] M. Battiato, K. Carva, and P. M. Oppeneer, Superdiffusive Spin Transport as a Mechanism of Ultrafast Demagnetization, Physical Review Letters **105**, 027203 (2010).

[94] M. D. Stiles, Spin-dependent interface transmission and reflection in magnetic multilayers (invited), Journal of Applied Physics **79**, 5805 (1996).

[95] A. Hirohata and K. Takanashi, Future perspectives for spintronic devices, Journal of Physics D: Applied Physics **47**, 193001 (2014).

[96] S. Okamoto, Spin injection and spin transport in paramagnetic insulators, Physical Review B **93**, 064421 (2016).

[97] G. L. Eesley, Observation of Nonequilibrium Electron Heating in Copper, Physical Review Letters **51**, 2140 (1983).

[98] H. E. Elsayed-Ali, T. B. Norris, M. A. Pessot, and G. A. Mourou, Time-resolved observation of electron-phonon relaxation in copper, Physical Review Letters **58**, 1212 (1987).

[99] M. Bauer, A. Marienfeld, and M. Aeschlimann, Hot electron lifetimes in metals probed by time-resolved two-photon photoemission, Progress in Surface Science **90**, 319 (2015).

[100] R. W. Schoenlein, W. Z. Lin, J. G. Fujimoto, and G. L. Eesley, Femtosecond studies of nonequilibrium electronic processes in metals, Physical Review Letters **58**, 1680 (1987).

[101] J. Briones, H. C. Schneider, and B. Rethfeld, Monte Carlo simulation of ultrafast nonequilibrium spin and charge transport in iron, Journal of Physics Communications **6**, 035001 (2022).

[102] J. Briones, M. Weber, B. Stadtmüller, H. C. Schneider, and B. Rethfeld, Effect of iron thicknesses on spin transport in a Fe/Au bilayer system, Journal of Applied Physics **134**, 043907 (2023).

[103] A. Melnikov, I. Razdolski, T. O. Wehling, E. T. Papaioannou, V. Roddatis, P. Fumagalli, O. Aktsipetrov, A. I. Lichtenstein, and U. Bovensiepen, Ultrafast Transport of Laser-Excited Spin-Polarized Carriers in Au/Fe/MgO(001), Physical Review Letters **107**, 076601 (2011).

[104] I. Razdolski, A. Alekhin, N. Ilin, J. P. Meyburg, V. Roddatis, D. Diesing, U. Bovensiepen, and A. Melnikov, Nanoscale interface confinement of ultrafast spin transfer torque driving non-uniform spin dynamics, Nature Communications **8**, 15007 (2017).

[105] Y. Beyazit, J. Beckord, P. Zhou, J. Meyburg, F. Kühne, D. Diesing, M. Ligges, and U. Bovensiepen, Local and Nonlocal Electron Dynamics of Au/Fe/MgO(001) Heterostructures Analyzed by Time-Resolved Two-Photon Photoemission Spectroscopy, Physical Review Letters **125**, 076803 (2020).

[106] Y. Beyazit, F. Kühne, D. Diesing, P. Zhou, J. Jayabalan, B. Sothmann, and U. Bovensiepen, Ultrafast electron dynamics in Au/Fe/MgO(001) analyzed by Au- and Fe-selective pumping in time-resolved two-photon photoemission spectroscopy: Separation of excitations in adjacent metallic layers, Physical Review B **107**, 085412 (2023).

[107] S. Kaltenborn, Y.-H. Zhu, and H. C. Schneider, Wave-diffusion theory of spin transport in metals after ultrashort-pulse excitation, Physical Review B **85**, 235101 (2012).

[108] Y. Beyazit, *Local and Nonlocal Relaxation Dynamics of Hot Electrons in Au/Fe/MgO(001) Thin Films*, PhD Thesis, Universität Duisburg-Essen, Duisburg (2023).

[109] F. Schwabl, *Statistische Mechanik*, Springer-Lehrbuch (Springer, Berlin, Heidelberg, 2006).

[110] D. W. Snoke and J. P. Wolfe, Population dynamics of a Bose gas near saturation, Physical Review B **39**, 4030 (1989).

[111] D. W. Snoke, W. W. Rühle, Y.-C. Lu, and E. Bauser, Evolution of a nonthermal electron energy distribution in GaAs, Physical Review B **45**, 10979 (1992).

[112] B. Y. Mueller and B. Rethfeld, Relaxation dynamics in laser-excited metals under nonequilibrium conditions, Physical Review B **87**, 035139 (2013).

[113] D. M. Nenno, B. Rethfeld, and H. C. Schneider, Particle-in-cell simulation of ultrafast hot-carrier transport in Fe/Au heterostructures, Physical Review B **98**, 224416 (2018).

[114] M. Battiato, K. Carva, and P. M. Oppeneer, Theory of laser-induced ultrafast superdiffusive spin transport in layered heterostructures, Physical Review B **86**, 024404 (2012).

[115] V. Kumar, K. Chandan, K. V. Nagaraja, and M. V. Reddy, Heat Conduction with Krylov Subspace Method Using FEniCSx, Energies **15**, 8077 (2022).

[116] H. Kareem Jalghaf, I. Omle, and E. Kovács, A Comparative Study of Explicit and Stable Time Integration Schemes for Heat Conduction in an Insulated Wall, Buildings **12**, 824 (2022).

[117] M. H. Jacobs, Diffusion Processes, in *Diffusion Processes*, edited by M. H. Jacobs (Springer, Berlin, Heidelberg, 1935) pp. 1–145.

[118] J. H. Lienhard, *A Heat Transfer Textbook: Fifth Edition*, reprint edition ed. (Dover Publications Inc., Mineola, New York, 2019).

[119] M. Heckschen and B. Sothmann, Pair-amplitude dynamics in strongly coupled superconductor–quantum dot hybrids, Physical Review B **105**, 045420 (2022).

[120] D. Futterer, *Transport through Hybrid Superconducting/Normal Nanostructures*, PhD Thesis, Universität Duisburg-Essen (2013).

[121] A. V. Rozhkov and D. P. Arovas, Interacting-impurity Josephson junction: Variational wave functions and slave-boson mean-field theory, Physical Review B **62**, 6687 (2000).

[122] R. Biele and R. D'Agosta, Beyond the State of the Art: Novel Approaches for Thermal and Electrical Transport in Nanoscale Devices, Entropy **21**, 752 (2019).

[123] D. Sánchez and M. Moskalets, Quantum Transport in Mesoscopic Systems, Entropy **22**, 977 (2020).

[124] R. Landauer, Spatial Variation of Currents and Fields Due to Localized Scatterers in Metallic Conduction, IBM Journal of Research and Development **1**, 223 (1957).

[125] M. Büttiker, Y. Imry, R. Landauer, and S. Pinhas, Generalized many-channel conductance formula with application to small rings, Physical Review B **31**, 6207 (1985).

[126] M. Büttiker, Four-Terminal Phase-Coherent Conductance, Physical Review Letters **57**, 1761 (1986).

[127] F. B. Anders, Steady-State Currents through Nanodevices: A Scattering-States Numerical Renormalization-Group Approach to Open Quantum Systems, Physical Review Letters **101**, 066804 (2008).

[128] S. Hershfield, Reformulation of steady state nonequilibrium quantum statistical mechanics, Physical Review Letters **70**, 2134 (1993).

[129] F. B. Anders and A. Schiller, Real-Time Dynamics in Quantum-Impurity Systems: A Time-Dependent Numerical Renormalization-Group Approach, Physical Review Letters **95**, 196801 (2005).

[130] F. B. Anders and A. Schiller, Spin precession and real-time dynamics in the Kondo model: Time-dependent numerical renormalization-group study, Physical Review B **74**, 245113 (2006).

[131] F. B. Anders, A numerical renormalization group approach to non-equilibrium Green functions for quantum impurity models, Journal of Physics: Condensed Matter **20**, 195216 (2008).

[132] C. J. Lindner, F. B. Kugler, V. Meden, and H. Schoeller, Renormalization group transport theory for open quantum systems: Charge fluctuations in multilevel quantum dots in and out of equilibrium, Physical Review B **99**, 205142 (2019).

[133] H. Schoeller and G. Schön, Mesoscopic quantum transport: Resonant tunneling in the presence of a strong Coulomb interaction, Physical Review B **50**, 18436 (1994).

[134] J. König and H. Schoeller, Strong Tunneling in the Single-Electron Box, Physical Review Letters **81**, 3511 (1998).

[135] J. König, H. Schoeller, and G. Schön, Resonant Tunneling and Coulomb Oscillations, Europhysics Letters **31**, 31 (1995).

[136] J. König, H. Schoeller, and G. Schön, Cotunneling and renormalization effects for the single-electron transistor, Physical Review B **58**, 7882 (1998).

[137] J. König, H. Schoeller, and G. Schön, Cotunneling at Resonance for the Single-Electron Transistor, Physical Review Letters **78**, 4482 (1997).

[138] J. König, *Quantum fluctuations in the single-electron transistor*, PhD Thesis, Universität Karlsruhe (TH), Karlsruhe (1999).

[139] B. Sothmann, *Influence of spin excitations on transport through a quantum-dot spin valve*, PhD Thesis, Universität Duisburg-Essen (2011).

[140] A. Bauer, *Phase-dependent heat transport in topologically nontrivial Josephson junctions*, PhD Thesis, Universität Duisburg-Essen, Duisburg (2022).

[141] G. C. Wick, The Evaluation of the Collision Matrix, Physical Review **80**, 268 (1950).

[142] M. Governale, M. G. Pala, and J. König, Real-time diagrammatic approach to transport through interacting quantum dots with normal and superconducting leads, Physical Review B **77**, 134513 (2008).

[143] J. König and J. Martinek, Interaction-Driven Spin Precession in Quantum-Dot Spin Valves, Physical Review Letters **90**, 166602 (2003).

[144] M. Kamp and B. Sothmann, Phase-dependent heat and charge transport through superconductor–quantum dot hybrids, Physical Review B **99**, 045428 (2019).

[145] S. Weiss and J. König, Odd-triplet superconductivity in single-level quantum dots, Physical Review B **96**, 064529 (2017).

[146] Y. Meir and N. S. Wingreen, Landauer formula for the current through an interacting electron region, Physical Review Letters **68**, 2512 (1992).

[147] M. G. Pala, M. Governale, and J. König, Nonequilibrium Josephson and Andreev current through interacting quantum dots, New Journal of Physics **9**, 278 (2007).

[148] P. Stegmann, *Generalized factorial cumulants applied to Coulomb-blockade systems*, PhD Thesis, Universität Duisburg-Essen (2017).

[149] M. J. Martínez-Pérez, P. Solinas, and F. Giazotto, Coherent Caloritronics in Josephson-Based Nanocircuits, Journal of Low Temperature Physics **175**, 813 (2014).

[150] J. Splettstoesser, M. Governale, and J. König, Adiabatic charge and spin pumping through quantum dots with ferromagnetic leads, Physical Review B **77**, 195320 (2008).

[151] S. Liu and G. Trenkler, Hadamard, Khatri-Rao, Kronecker and Other Matrix Products, International Journal of Information and Systems Sciences **4**, 160 (2008).

[152] T. Dittrich, P. Hänggi, G.-L. Ingold, B. Kramer, G. Schön, and W. Zwerger, *Quantum transport and dissipation*, Vol. 3 (Wiley-Vch Weinheim, 1998).

[153] S. D. Brorson, J. G. Fujimoto, and E. P. Ippen, Femtosecond electronic heat-transport dynamics in thin gold films, Physical Review Letters **59**, 1962 (1987).

[154] X. Liu, R. Stock, and W. Rudolph, Ballistic electron transport in Au films, Physical Review B **72**, 195431 (2005).

[155] J. I. Mustafa, M. Bernardi, J. B. Neaton, and S. G. Louie, Ab initio electronic relaxation times and transport in noble metals, Physical Review B **94**, 155105 (2016).

[156] D. Gall, Electron mean free path in elemental metals, Journal of Applied Physics **119**, 085101 (2016).

[157] V. Palenskis, Drift Mobility, Diffusion Coefficient of Randomly Moving Charge Carriers in Metals and Other Materials with Degenerated Electron Gas, World Journal of Condensed Matter Physics **2013**, 73 (2013).

[158] J. König, *Resonanztunneln in mesoskopischen Systemen*, Diplomarbeit, Universität Karlsruhe (TH), Karlsruhe (1995).

Danksagung

Mein Dank gilt an erster Stelle meinem Betreuer Prof. Dr. Björn Sothmann. Ohne seine gewissenhafte und gute Betreuung während meiner Masterarbeit hätte ich nie mit einer Promotion begonnen. Während meiner Promotion stand mir seine Tür immer offen und er wurde auch nie müde mir weiterzuhelfen, wenn es mal hakte.

Weiter möchte ich mich bei allen aktiven und ehemaligen Mitgliederinnen und Mitgliedern der AG König und AG Sothmann bedanken. Das gute Arbeitsklima in der Gruppe hat mich jeden Tag aufs Neue motiviert. Besonders hervorheben möchte ich meinen Büropartner Alexander. In der Regel konnten wir uns zwar nicht gegenseitig bei unseren Problemen weiterhelfen aber der humorvolle Umgang damit sowie die guten Gespräche haben mir immer viel Freude bereitet.

Ich möchte mich außerdem bei meinen Kolleginnen und Kollegen aus dem SFB 1242 bedanken. Die vielen wissenschaftlichen und nichtwissenschaftlichen Aktivitäten boten mir eine gute Abwechslung zu meinem persönlichen Forschungsalltag. Darüber hinaus förderte der Austausch eine gemeinsame Publikation. Für die gute Zusammenarbeit möchte ich mich an dieser Stelle noch einmal herzlich bei meinen Koautorinnen und Koautoren bedanken.

Mein Dank gilt außerdem meinen Freundinnen und Freunden aus dem Studium. Ohne sie wäre meine Zeit als Student nicht so schön gewesen. Ich möchte mich auch bei den Mitgliederinnen und Mitgliedern des Fachschaftrats Physik bedanken, die mit mir zusammen die vielen schönen Veranstaltungen und Fahrten organisiert haben.

Natürlich möchte ich mich auch bei meinen Eltern bedanken, die es mir finanziell ermöglicht haben, mich vollständig auf mein Studium zu konzentrieren und mir auch während der Promotion eine sichere Anlaufstelle boten. Besonders bedanken möchte ich mich auch bei meiner Schwester Maria, der ich mich immer anvertrauen konnte.

Zu guter Letzt möchte ich mich bei meiner Freundin Eileen bedanken. Ohne deine uneingeschränkte Unterstützung hätte ich es nicht geschafft. Ich liebe dich.